Institut für
Umformtechnik
und Leichtbau

Hamed Dardaei Joghan

Hybrid additive manufacturing of metal laminated forming tools

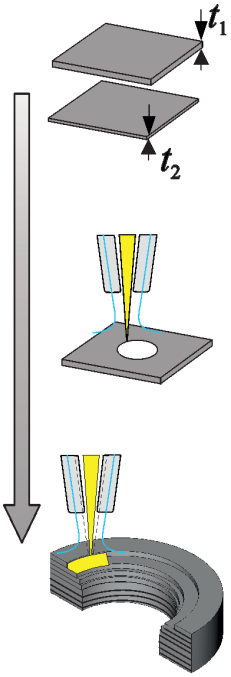

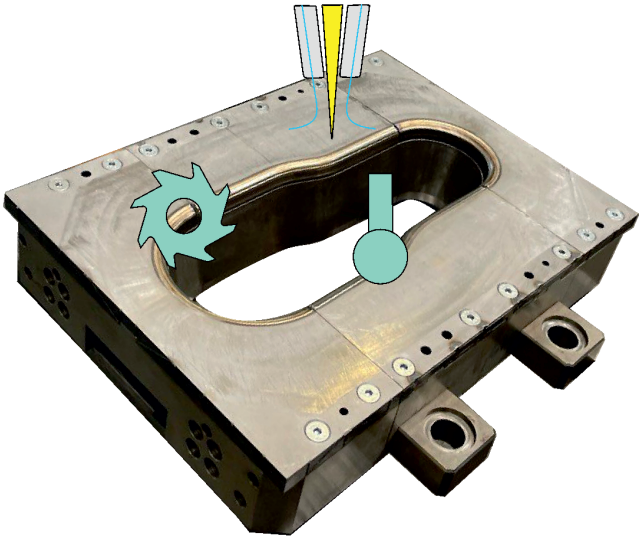

Reihe
Dortmunder Umformtechnik **Nr. 123**

Hybrid additive manufacturing of metal laminated forming tools

Zur Erlangung des akademischen Grades eines

Dr.-Ing.

der Fakultät Maschinenbau
der Technischen Universität Dortmund

Dissertation

vorgelegt von

Hamed Dardaei Joghan, M. Sc.

aus

Tabriz

Dortmund, 2024

Vorsitzender der Prüfungskommission:	PD Dr. habil. Tobias Kaiser
Berichter:	Prof. Dr.-Ing. A. Erman Tekkaya
Mitberichter:	Prof. Dr.-Ing. Jan T. Sehrt
	Prof. PD Dr.-Ing. Andreas Zabel
Tag der mündlichen Prüfung:	27. 02.2024

Dortmunder Umformtechnik

Band 123

Hamed Dardaei Joghan

Hybrid additive manufacturing of metal laminated forming tools

D 290 (Diss. Technische Universität Dortmund)

Shaker Verlag
Düren 2024

Bibliographic information published by the Deutsche Nationalbibliothek
The Deutsche Nationalbibliothek lists this publication in the Deutsche Nationalbibliografie; detailed bibliographic data are available in the Internet at http://dnb.d-nb.de.

Zugl.: Dortmund, Technische Univ., Diss., 2024

Printed in Germany.

ISBN 978-3-8440-9481-7
ISSN 1619-6317

Shaker Verlag GmbH • Am Langen Graben 15a • 52353 Düren
Phone: 0049/2421/99011-0 • Telefax: 0049/2421/99011-9
Internet: www.shaker.de • e-mail: info@shaker.de

Acknowledgments

A main part of this dissertation is the project's outcome with the title"Reducing the stair step effect for dies manufactured by layer-laminated manufacturing by additive and formative post-processing," with project number 426515407 funded by the (German Research Foundation (DFG) at the Institute of Forming Technology and Lightweight Components (IUL) at the Technical University of Dortmund. Therefore, I would like to take this opportunity to thank DFG for supporting their fund. Getting through my dissertation required more than academic support, and I have to thank many people.

I would like to express my deepest gratuities to Prof. A. Erman Tekkaya for his trust and allowance to write my doctoral thesis under his supervision. During my work at IUL, I have received constant encouragement, constructive discussions, and guidance to develop scientific and personal views from him. I would also like to thank the head of the Institute for Hybrid Additive Manufacturing (HAM) at the University of Bochum, Prof. Dr.-Ing. Jahn Sehrt, for his co-supervision of my dissertation. I would also like to show gratitude to my examination committee, including Prof. PD Dr.-Ing. Andreas Zabel and PD Dr. habil. Tobias Kaiser.
I would also like to thank all my colleagues at the IUL for the pleasant working atmosphere, helpfulness, and friendly relationship. Dr. Marlon Hahn is incredibly grateful for his support and encouragement and our numerous scientific discussions. I also thank Dr. Ramona Hölker-Jäger and Prof. Till Clausmyer for their scientific support. This journey would not have been possible without the support of the technical staff, particularly Dirk Hoffmann, Werner Feuer, and Sven Lukis, who significantly contributed to preparing the parts, and Jeanette Brand and Nina Hänisch for their support at the IUL office. I would also like to thank all the students who wrote student works under my supervision and students' assistants for their excellent cooperation.

I appreciate my family's support while I was working on my dissertation.

Finally, I must express my profound gratitude to my parents, whose encouragement was the primary motivation to overcome the difficulties throughout my academic journey. I also want to thank my brothers for the unconditional support of our parents over the years, which assisted me in concentrating on my research and work abroad.

Dormund, Febraury 2024

To my parents

Abstract

This thesis introduces and investigates a new resource-efficient manufacturing method for rapid tooling. The presented hybrid method combines two additive manufacturing processes: sheet metal lamination and direct energy deposition (DED). In this combination, the core of the forming tool is fabricated by sheet lamination in a short time and at a low cost. The resulting step areas are compensated by laser metal deposition (LMD), which is a subset of the DED process. Three post-processing methods, milling, ball burnishing and laser polishing, are applied and compared to improve the surface roughness of the deposited areas.

The results show the essence of the two-step filling strategy, in which a bonding step should bond together the tool sheets, and in the next step, the remaining stair-step areas should be filled by LMD. The tensile strength of the fillet bonding for different process parameters and tool sheet combinations shows that the higher laser power and feed rate result in higher strength; however, the sheet thickness also needs to be considered to avoid the melt-through of the thin sheets. In the filling step, filling in the radius direction shows better surface roughness, but the nozzle life is shorter. The preheating of the die sheet to reduce the residual tensile stress shows only a 25 % reduction, which causes waviness of the deposited surface. Therefore, it can be neglected.

A semi-analytical model to analyze the stress distribution showed the possibility of using the low-strength tool sheets in a major part of the laminated tool. Deep drawing experiments are successful for two types of blanks. The wear test study shows low wear of the dies manufactured by the hybrid method in comparison with the conventional method. The feasibility of manufacturing complex geometries is demonstrated by a manufactured demonstrator.

The economic and technological advantages of the hybrid method are compared with conventional and fully manufactured tools by LMD, and the number of possible sheet combinations for tool lamination is reduced by considering cost and energy criteria.

Zusammenfassung

In dieser Arbeit erfolgt die Entwicklung und Untersuchung eines neuen ressourceneffizienten Fertigungsverfahrens für das Rapid Tooling. Das vorgestellte Verfahren Tooling kombiniert zwei additive Fertigungskategorien: Sheet lamination und Direct Energy Deposition (DED). In dieser Kombination wird der Kern des Umformwerkzeugs durch Blechlaminierung in kurzer Zeit und zu geringen Kosten hergestellt. Die entstehenden Treppenstufenbereiche werden durch Laserpulverauftragschweißen (LPA), zugehörig zur DED-Kategorie, kompensiert. Drei Nachbearbeitungsmethoden, Fräsen, Glattwalzen und Laserpolieren, werden zur Verbesserung der Oberflächenrauheit der aufgebrachten Flächen eingesetzt und verglichen.

Die Ergebnisse zeigen, dass das Konzept einer zweistufigen Füllstrategie, bei der die Werkzeugbleche zunächst zusammengefügt wurden, und im nächsten Schritt die verbleibenden Treppenstufenbereiche durch LPA gefüllt werden, von Vorteil ist. Untersuchungen an Kehlnahtverbindungen bei verschiedenen Prozessparametern und Werkzeugblechkombinationen zeigen, dass eine höhere Laserleistung und Vorschubgeschwindigkeit zu einer höheren Festigkeit führen; allerdings sollte auch die Blechdicke berücksichtigt werden, um das Durchschmelzen der dünnen Bleche zu vermeiden. Beim Füllen zeigt sich, dass ein Auffüllen in radialer Richtung eine bessere Oberflächenrauheit als Auffüllung in der Kehlnahtrichtung aufweist. Die Vorwärmung des Werkzeugblechs zur Verringerung der Zugeigenspannungen führt nur zu einer Verringerung um 25 %, was zu einer Welligkeit der aufgebrachten Oberfläche führt. Daher kann sie vernachlässigt werden.

Ein semi-analytisches Modell zur Analyse der Spannungsverteilung zeigt die Möglichkeit der Verwendung von Werkzeugblechen mit niedriger Festigkeit in einem Großteil des laminierten Werkzeugs. Tiefziehversuche sind für zwei Arten von Blechen erfolgreich, für kaltgewalzten hochfesten Stahl (HC380LA) und für eine Spezieltiefziehgüte (DC06). Verschleißuntersuchungen zeigen, dass der Verschleiß der mit der Hybridmethode hergestellten Matrizen im Vergleich zur konventionellen Methode gering ist. Ein Demonstrator beweist die Herstellbarkeit auch komplexer Geometrien.

Die wirtschaftlichen und technologischen Vorteile des Hybridverfahrens werden mit konventionellen und vollständig mit LMD gefertigten Werkzeugen verglichen und die Anzahl der möglichen Blechkombinationen für die Werkzeugauslegung wird unter Berücksichtigung von Kosten- und Energiekriterien reduziert.

Index

Publication of contents ix

List of supervised student theses ix

Formula symbols and abbreviations x

1 Introduction 1

2 State of the art 3

2.1 Sheet metal forming ... 3
2.2 Basics of deep drawing ... 3
2.3 Manufacturing deep drawing tools ... 6
2.3.1 Subtractive methods ... 6
2.3.2 Non-conventional methods ... 6
2.3.3 Additive manufacturing ... 7
2.3.3.1 Direct energy deposition (DED) ... 7
2.3.3.2 Sheet lamination ... 12
2.3.4 Hybrid additive manufacturing ... 23
2.4 Summary ... 28

3 Aim and scope 29

4 Materials and experimental methods 33

4.1.1 Tool sheet (laminae) ... 33
4.1.2 Deep drawing sheets ... 33
4.1.3 Tensile tests ... 33
4.1.4 In-plan torsion test ... 35
4.1.5 Powders for LMD ... 35
4.1.6 Laser metal deposition ... 36
4.1.7 Deep drawability and wear tests ... 37
4.1.8 Setup for demonstrator die ... 38
4.1.9 Ball burnishing ... 39
4.1.10 Strip tensile test ... 39
4.2 Measurements ... 40
4.2.1 Optical surface roughness measurement ... 40
4.2.2 Metallography and hardness measurement ... 40
4.2.3 Residual stress measurement ... 41

5 Tool design procedures 43

5.1 Properties of single/multi-deposited tracks ... 44
5.1.1 Single weld track ... 46

5.1.2 Multi-weld tracks ... 52
5.2 Preheating of substrate sheets ... 55
5.2.1 Preheating effect on surface roughness ... 56
5.2.2 Influence of preheating on residual stress ... 58
5.2.3 Influence of preheating on form accuracy ... 59
5.2.4 Influence of preheating on hardness ... 61
5.2.5 Influence of preheating on bending radius ... 62
5.3 Tribological study of laminated tooling ... 64
5.4 Summary ... 66

6 Realization of hybrid laminated tooling 67

6.1 Semi-analytical approach for laminated tooling ... 67
6.2 Deep drawing experiments ... 78
6.3 Laser polishing and ball burnishing ... 81
6.4 Wear study ... 88
6.5 Transfer to complex shapes (demonstrator) ... 91
6.6 Summary ... 94

7 Technological, economic, and energetic evaluation 97

7.1 Hybrid additive lamination method ... 98
7.2 LMD plus milling ... 103
7.3 Conventional method (milling plus hardening) ... 104
7.4 Comparison between the different processes ... 105
7.5 Determination of optimal sheet combination ... 108
7.6 Summary ... 111

8 Conclusion and outlook 113

8.1 Smart tooling ... 114
8.2 Cold forging dies ... 115
8.3 Workpieces ... 116
8.4 Hot stamping punches ... 116

References 119

Attachment A 131

Attachment B 137

Curriculum vitae CXL

Publication of contents

Dardaei Joghan, H., Hahn, M., Sehrt, J.T, Tekkaya, A.E., 2022a. Hybrid additive manufacturing of metal laminated forming tools. CIRP Annals, vol. 71, pp. 225-228.

Dardaei Joghan, H., Hahn, M., Tekkaya, A.E., 2022b. Effect of preheating during laser metal deposition on the properties of laminated bending dies. The International Journal of Advanced Manufacturing Technology, vol. 125, pp. 157-168.

Dardaei Joghan, H., Hahn, M., Aboola, O. E., Tekkaya, A. E. 2023a. Resources and manufacturing technology evaluation of hybrid additive metal laminated tooling for forming. Materials Research Proceedings, vol. 28, pp. 21-30.

Dardaei Joghan, H., Jölker-Jäger R., Komodromos A., Tekkaya A. E. 2023b. Hybrid additive manufacturing of forming tools. Special Issue on Automotive Lightweight, vol. 6, pp. 311-323.

List of supervised student theses

Bill Febrian Winoto, 2021. Development of a semi-analytical model for laminated forming tools under process forces. Master thesis.

Jakob Hamm, 2020. Untersuchung und Beurteilung der Strategien zur Verbindung lamellarer Stahlbauteile durch einzelne Schweißnähte mittels Laserpulverauftragschweißen. Bachelor thesis.

Mehmet-Kasim Ocakli, 2022, Hybride additive Fertigung einer laminierten Werkzeuggeometrie mit Freiformflächen. Bachelor thesis.

Niklass Resse and Neshanth Paskaran, 2021. Erstellung einer Berechnungsmethode für die produktionstechnische Bewertung von Fertigungskombinationen mit Schicht-Laminat-Verfahren und Laserpulverauftragschweißen. Project work.

Ololade Emmanuel Agboola, 2023. Effect of process parameters of laser metal deposition and laser polishing on flat surfaces. Project work.

Ololade Emmanuel Agboola, 2023. Realization of hot stamping dies using an optimized hybrid additive laminated tool. Master thesis.

Surav Tank, 2023. Investigation of laser polishing and ball burnishing effects on laser metal deposited surfaces. Project work.

Formula symbols and abbreviations

Nomenclature

Symbol	Unit	Description
A	mm^2	Area
A_c	mm^2	Material mixture area with substrate after deposition
A_D	mm^2	Deposited area
A_g	-	Fracture strain
A_P	mm^2	Part's area
A_s	mm^2	Scrap's area
a	mm	Free length of the tool sheet
a_b	mm	Length of stacked beam under support
a_e	mm	Radial depth of cut
a_p	mm	Axial depth of cut
b	mm	Width of the tool sheet
b_S	mm	Tool sheet offset
c_d	mm	Clearance between the die and the punch
C	-	Constant value
C_L	mm	Cutting length
c	-	Thickness-to-length ratio
D	N	Axial stiffness of stacked beam
D_B	mm	Blank initial diameter
D_{Die}	mm	Inner diameter of deep drawing die
D_P	mm	Punch diameter
d	mm	Cylindrical hole with diameter
d_L	mm	Laser spot diameter

Symbol	Unit	Description
$\dot{D}$	g/min	Deposition rate
E	MPa	E-Module
E_{B}	J	Energy for ball burnishing
E_{Bulk}	J	Energy for production of bulk material
E_{H}	J	Energy for hardening
E_{LC}	J	Energy for laser cutting
E_{LMD}	J	Energy for LMD
E_{LP}	J	Energy for laser polishing
E_{M}	J	Energy for milling
E_{Powder}	J	Energy for production of powder
E_{PP}	J	Energy for post-processing
E_{Sheet}	J	Energy for production of sheet
E_{rq}	J	Required energy consumption
F_{H}	N	Horizontal force
f	mm/min	Feed rate or scanning speed
f_{P}	mm/min	Feed rate of laser polishing
G	GPa	Shear modulus
H	mm	Height of elastic support
H_{B}	RC or Vickers	Hardness
H'_B	-	Change of hardness
h_{c}	mm	Depth or height of the cup
h_{d}	mm	Hatching distance
I	mm^4	Inertia of moment
j	-	Degree of polynomial

Symbol	Unit	Description
k	GPa	Elastic modulus of elastic bed
L	-	Constant value
M	N.mm	Bending moment
m	-	Slope of the inter-planer spacing to different tits
m_{P}	kg	Part's mass
m_{s}	kg	Scrap's mass
m_{Step}	kg	Sum of stair-step areas
$\dot{m}$	g/min	Powder feed rate or mass flow
n	-	Number of stacked tool sheets
P	W	Laser power
P_{BH}	MPa	Blank holder pressure
P_{N}	-	Number of possible sheet combinations
P_{P}	W	Laser power for laser polishing
P_{r}	MPa	Reaction pressure of elastic bed
q	N/mm	Distributed force
Q	N	Shear force in beam theory
Q	mm^3/h	Material removal rate
R	mm	Die corner radius
R'_{m}	mm	Bending radius after unloading
R'_a	-	Change of average surface roughness
R'_z	-	Change of maximum height of surface roughness
R_{a}	µm	Arithmetical mean deviation of the profile in 2D
R_{m}	MPa	Ultimate strength

Symbol	Unit	Description
R_m	mm	Bending radius before unloading
R_P	mm	Punch corner radius
$R_{p0,2}$	$N \cdot mm^{-2}$	Tensile strength
R_z	µm	Maximum height of the profile in 2D
r	-	Anisotropy coefficient
r_n	-	Normal anisotropy
Δr	-	Planer anisotropy
S	$N.mm^2$	Stiffness of stacked beam
S_a	µm	Arithmetical mean deviation of the profile in 3D
SEC	J/kg	Specific energy consumption
S_k	µm	Roughness depth of the core
S_{mr}	%	Areal material ratio
S_z	µm	Maximum height of the profile in 3D
s	mm	Thickness position
T	°C	Temperature
T_s	mm	Sum of the stacked beam thicknesses
T_H	s	Time for hardening
T_{LC}	s	Time for laser cutting
T_{LMD}	s	Time for LMD
T_{PP}	s	Time for post-processing
T_T	s	Total manufacturing time
t	mm	Tool sheet thickness
t_b	mm	Blank thickness
u	mm	Displacement of the stacked beam

Symbol	Unit	Description
u'	rad	1st order invariant of displacement (Bending angle)
u''	1/mm	2nd order invariant of displacement
u_2'''	1/mm	3th order invariant of displacement
V	mm^3	Volume
v_P	mm/min	Punch velocity
W_a	µm	Waviness arithmetical mean deviation of the profile in 3D
W_D	mm	Working distance between laser nozzle and deposited surface
X	-	Material yield
x^N	-	Normalized length in the *x*-direction
z^*	mm	Distance of the neutral layer to the middle of the beam layer's cross-section
z^N	-	Normalized length in the thickness direction
β	-	Deep drawing ratio
Γ	-	Coefficient factor
γ	°	Angle
$\bar{\varepsilon}_{Plastic}$	-	Equivalent plastic strain
ε	-	Strain
θ	W/(kg/mm)	Track-specific power density
θ_z	°	Angle of rotation of normal to the mid-surface of the deflection in beam theory
Λ	-	Correction factor for maximum von Mises stress
λ	J/mm	Applied energy per unit length by laser polishing

Symbol	Unit	Description
μ	-	Friction factor
ρ	Kg/mm^3	Density
$\sigma_{v.M.}^{N}$	-	Normalized von Mises stress
σ_f	MPa	Flow stress
σ_n	MPa	Normal stress
σ_r	MPa	Radial stress
σ_t	MPa	Tangential stress
σ_w	MPa	Weld fracture strength
τ	MPa	Shear stress
ν	-	Poisson's ratio
$\emptyset$	-	Dilution ratio

Indices

Index	Description
0	Initial value
eff	Effective
eq	Equivalent
max	Maximum
min	Minimum

Abbreviations

Abbreviation	Description
2D	Two dimensional
3D	Three dimensional
AM	Additive manufacturing
AWJ	Abrasive water jet
BC	Boundary condition
CAD	Computer-aided design
CAM	Computer-aided manufacturing
CIRP	International academy for production engineering
CNC	Computer numerical control
CVD	Chemical vapour deposition
DED	Direct energy deposition
EBSD	Electron backscatter diffraction
EDX	Energy-dispersive X-ray spectroscopy
FEM	Finite element method
FGM	Functionally graded material
FSW	Friction stir welding
GMAW	Gas metal arc welding

GTAW	Gas tungsten arc welding
HAM	Hybrid additive manufacturing
HAZ	Heat affected zone
LBMD	Laser-based metal deposition
LDMD	Laser direct metal deposition
LENS	Laser engineered net shape
LFF	Laser freeform fabrication
LLM	Layer laminated manufacturing
LMD	Laser metal deposition
LMDS	Laser metal deposition shaping
LOM	Laminated object manufacturing
LSA	Laser surface alloying
LST	Laminated steel tooling
N.A.	Neutral axis
PEL	Profiled edge laminae
RT	Room temperature
SEC	Specific energy consumption
SOM	Surface over-melt
SSM	Shallow surface melting
TIG	Tungsten inert gas

1 Introduction

Green manufacturing is not possible without implementing decarburization of manufacturing processes. The goal of increasing the number of green factories is only possible by optimizing or regenerating existing manufacturing solutions. Based on the 2015 Paris Agreement, total net greenhouse gas (GHG) emissions should be zero by 2050 (**Fig. 1.1a**), which means global warming should be limited to 2 °C above pre-industrial levels. However, experts offer to keep the global temperature increase below 1.5°C, referred to as the 1.5 °C pathway. To achieve this goal, CO_2 emissions would have to be reduced from 33 gigatons CO_2e to about 18 Gt CO_2e by 2030. This implies a 57 % reduction in CO_2 emissions for production-related CO_2 emissions, **Fig. 1.1b** (Küpper et al., 2022).

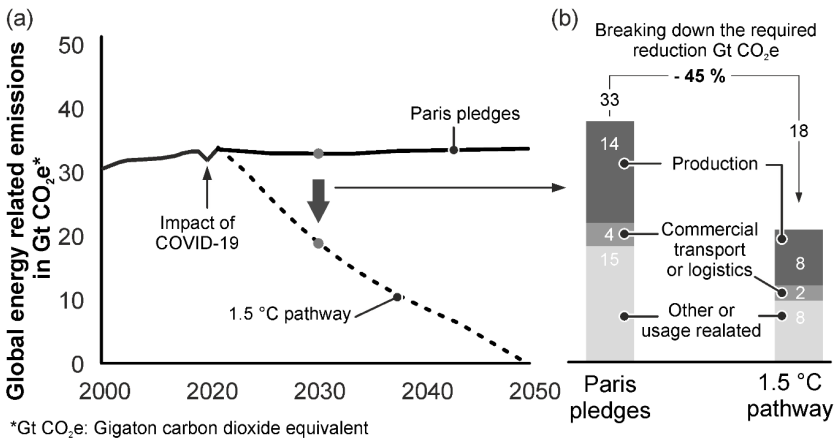

Figure 1.1: (a) Net emissions pathways to limit global warming to 1.5 °C, (b) required decrease in greenhouse gas emission by 2030 for achieving net zero by 2050 (Küpper et al., 2022)

In pursuit of this goal, companies need to increase their energy efficiency. One way to increase efficiency is to improve the existing process. This can be done by combining different methods and eliminating unnecessary steps in the production process.

Due to industry requirements such as high strength and hardness, metal forming tools require high manufacturing energy. Deep drawing is a standard metal forming process widely used in almost every product in the automotive industry, home appliances, and other transportation systems. The design of deep drawing dies depends on the unique characteristics resulting from the number of parts, the material to be formed or the process forces applied to the die and the size or shape of the drawn part. The

conventional method of manufacturing deep-drawing tools is via a machining process. The machining process has a high scrap rate and requires additional hardening to achieve the necessary hardness, which is energy-intensive. Depending on the strength of tool needed or functionality (implementation of sensors or cooling/heating channels), the tools are either manufactured as a single block (monoblock) or segmented (Doege and Behrens, 2010). For most serial production of deep-drawing tools, initial experiments are required to understand the material behavior and validate the numerical results, as not all details can be determined in advance in the design step.

The concept of rapid tooling is primarily used to perform initial prototyping experiments in a short time. Rapid tooling is mainly used for small batches and is normally not associated with large production quantities. Rapid tooling additionally provides the opportunity to identify process errors and the feasibility of the developed process. Additive manufacturing (AM) can now produce complex shapes without the additional tooling costs of rapid tooling. The main disadvantages of AM-based methods are high the energy consumption and the long manufacturing time. The first disadvantage is in contrast to green manufacturing goals, which require a process with low energy consumption and a smaller carbon footprint. The second disadvantage of long manufacturing time is that it is in conflict with the concept of rapid tooling, where tools must be manufactured quickly. Therefore, new process innovations are needed to meet both criteria to facilitate the goal of zero carbon emissions by 2050.

2 State of the art

2.1 Sheet metal forming

The cross section to volume ratio is much higher for sheet metal forming than for bulk metal forming. Sheet forming is used to produce complex lightweight components and process forces are much lower than bulk metal forming. As a result, the rigidity of the forming tool required for sheet metal forming is lower. (Lange, 1990)

2.2 Basics of deep drawing

Deep drawing is one of the most common sheet metal forming processes. Deep drawing is a tension-compression sheet forming process based on DIN 8584 (2003). In deep drawing, the blank flows through a punch into a hollow die, and a blank holder force controls the sheet flow (**Fig. 2.1a**). The purpose of the blank holder force is to prevent the blank from wrinkling and buckling during the deep-drawing process. As the punch moves at a defined speed (v_P) toward the blank (in the minus Z direction in Fig. 2.1a) to the final position, where is the depth or height of the cup, h_c, the workpiece is deformed to the shape of the punch and die cavity. The deep draw ratio (β) is defined as the ratio of the blank diameter, D_B, to the punch diameter, D_P, ($\beta = D_B / D_P$). The theoretical maximum achievable drawing ratio is $\beta = 2.72$. However, the maximum practical drawing ratio is lower, e.g., for steel, about 2 to 2.2 (Marciniak et al., 2002).

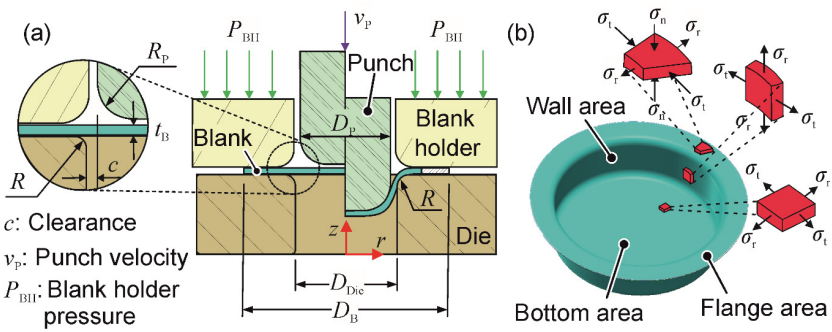

Figure 2.1: (a) Deep drawing process, (b) stress states in a deep-drawn cup

The blank encounters different stress states during deep drawing (**Fig. 2.1b**). The cup in the flange area exhibits tangential compressive stresses (σ_t), normal compressive stresses (σ_n), and tensile radial stresses (σ_r). However, the normal stress caused by the blank holder (σ_n) on the cup is insignificant. In the wall of the cup, the sheet stretches in the radial direction and the thickness direction. During deep drawing, tensile stresses in the thickness and radial directions occur at the bottom of the cup. In the deep drawing, one objective is to avoid thickness variations during the process.

A deep drawing tool needs to meet specific requirements such as geometric accuracy, appropriate surface roughness, stiffness, and hardness for a successful deep drawing process. For steel, it is recommended that the punch radius (R_P) should be at least three times greater than the die radius (R). In addition, the die radius should be between 5 to 10 times larger tool than the blank thickness (t_b). However, the optimal die radius is defined experimentally. The smaller die radius leads to a higher drawing force, while the larger the die radius, the less material will pass over the radius. The maximum drawing depth or cup height (h_c) is determined practically. The clearance between the die and the punch (c) is a function of the sheet thickness, and for steel sheets, it is calculated as follows $c_d = t_b + 0.007\sqrt{10t_b}$ (Boljanovic, 2004). The blank holder pressure (P_{BH}) is constant at about 1 or 2 % of the blank tensile strength ($R_{p0.2}$). The typical tool failures in the deep drawing are wear, plastic deformation, chipping, cracking, and galling. Punch movement and blank deformation result in inhomogeneous contact pressure (P) at the die corner. Low lubricant usage during forming due to environmental concerns and high contact pressure at the die radius results in high tool wear, leading to higher-strength tool material.

Determining the maximum pressures on the die during the deep drawing process is essential for optimal die design. Pereira et al. (2009) comprehensively studied the contact pressure condition in deep drawing die in a two-dimensional plane strain state. At the beginning of the deep drawing ($\zeta = \alpha_I$), the bending moment (M) in the contact line is maximum which leads to high bending stress and contact pressure peaks $P_{\alpha I}$ (**Fig. 2.2a**). The magnitude of this compressive high-peak stress is greater than the yield stress of the sheet ($R_{p0.2}$). In the intermediate state, as the punch stroke continues, point A moves away from the beginning of the die radius, and more material is in contact with the die radius. As a result, the pressure exerted by the blank on the tool decreases. The second contact point occurs at $\zeta = \alpha_{II}$, similar to the initial condition. It causes a high-contact pressure. In most cases, the punch stroke must pull material from the beginning of the die radius, point A, as shown in **Fig. 2.2b.**

In the final state, which is a steady-state step, point A is a part of the sidewall ($\zeta = \alpha_{III}$), and the new material is plastically bent by entering the die radius. This state has the lowest contact pressure peaks, which are less than the yield strength of the blank (**Fig. 2.2c**). Pereira et al. (2007) showed that the intermediate state step (at ca. $\zeta = 59°$) is the principal place for tool wear. However, the larger arc length results in a higher contact area in the steady state step, which can affect tool life depending on process conditions such as lubricant quantity and sliding speed. It can be seen that the main contact area subjected to high stresses and pressing forces is the die radius. Therefore, it is essential that the die surface in the radius exhibits high toughness and hardness during the process to avoid wear and failure in the process.

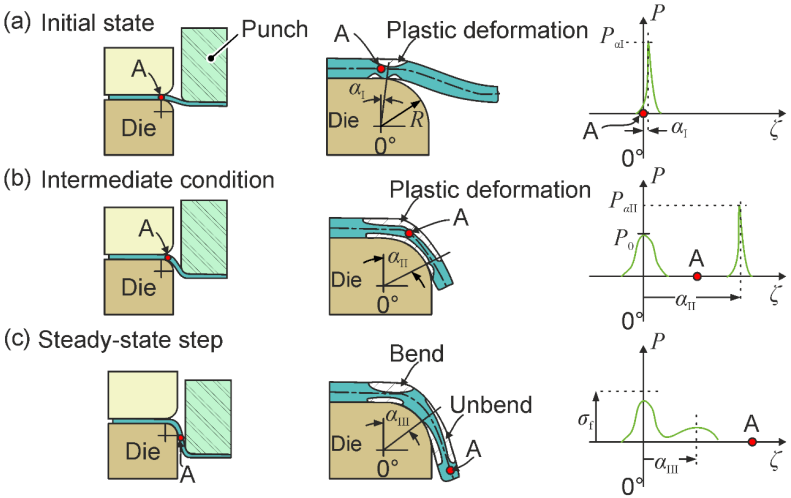

Figure 2.2: (a) Initial state, (b) intermediate condition, (c) steady-state step (Pereira et al., 2007)

Tool surface roughness plays an important role in the tribological behavior in addition to the level of forces and, consequently, stresses on the die during deep drawing. Various parameters are defined to characterize the quality of the surface. The surface irregularities are classified into three main types: (I) roughness, (II) waviness, and (III) shape error (Jiang et al., 2007). According to EN ISO 4287 (2010), in the 2D direction, the arithmetic mean deviation (R_a) and the mean roughness depth (R_z) are standard parameters used in industry (**Fig. 2.3**).

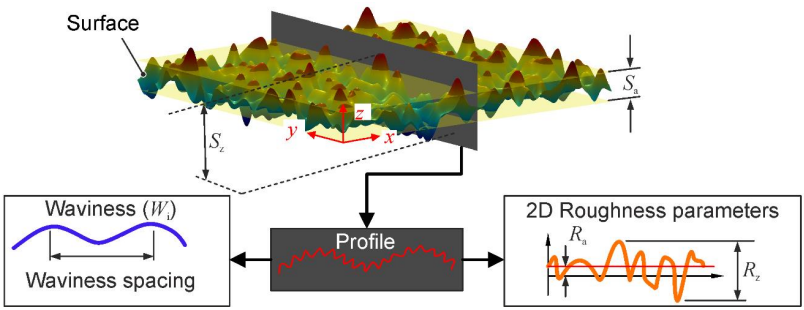

Figure 2.3: Definition of parameters for 3D surface and 2D profile

The main disadvantage of the two-dimensional profile parameters, especially determined by tactile measurement, is the dependence of the results on the measured

position. Optical measurement can determine the 2D surface parameters along several lines. According to the DIN EN 25178 (2016), several surface parameters are defined. The arithmetic mean of the absolute height (S_a) is an extension of the R_a in the areal scale (3D). The sum of the highest peak and the deepest pit in a defined area (S_z) is also an extension of the R_z (Fig. 2.3). Surface waviness can be characterized by W_a, the arithmetic mean deviation of the wave height, after removing the profile curvature.

2.3 Manufacturing deep drawing tools

The final geometric accuracy of deep-drawn parts is directly influenced by the accuracy of the tool. The tool manufacturing method should be selected based on the required process conditions (process forces, residual stresses, geometric accuracy, etc.) and within the allowed or desired processing time. The production of tools in a short time is a concept known as rapid tooling. Rapid tooling is a subset of rapid manufacturing and is defined as any manufacturing technology that can produce a tool in a short time. The primary goal of rapid tooling is to turn innovative design ideas into manufactured products in the shortest possible time. Rapid tooling methods are generally divided into direct and indirect (or transfer) categories. The direct method produces the target part with the required features. However, in the indirect method, sacrifice or transfer parts are manufactured to produce the target part (Pinkerton, 2010). These can be either prototypes or series of production tools or their elements, depending on the specific application and manufacturing technology (Gebhardt, 2016). Rapid tooling can generally be divided into four main groups, namely subtractive (conventional), non-conventional, additive manufacturing, and hybrid additive manufacturing. All four will be discussed below.

2.3.1 Subtractive methods

Milling, turning, and electric discharge machining (EDM) are common subtractive manufacturing methods for producing metal deep drawing dies, where turning being used for simple symmetrical shapes. Both milling and EDM are suitable for producing relatively complex shapes. In milling, process parameters such as tool speed, feed rate, toolpath overlap, lubricant application and type, and workpiece material directly affect the manufactured tool's surface finish and geometric accuracy. In most cases, due to the high forming process forces applied, the manufactured forming tool needs to be hardened after milling. The EDM method, also known as spark machining, spark erosion or die sinking, can machine many complex shapes and hard materials. The main disadvantage is the long production time.

2.3.2 Non-conventional methods

Conventional deep drawing dies are usually designed for maximum rigidity. However, for small batch production, casting of polymer to make deep-drawing dies offers the

possibility of manufacturing an inexpensive and fast tooling concept. Apart from the necessity of a negative die for casting, the main disadvantage of this method is the low wear resistance of the manufactured dies. Diamond-like carbon, chromium, and copper coatings deposited by physical vapor deposition (PVD) have been used, but their durability has been unsatisfactory. In addition to being time-consuming, a galvanic nickel coating has a low level of durability. Deep-drawing tests show that the wear resistance of the polymer-based deep-drawing die with thermally coated WC-FeCSiMn cored wire flux (EN ISO 14919-5-1.6-4) with 50 % FTC (fused tungsten carbide) is adequate for the high-strength steels used in small to medium-sized production runs. (Witulski et al., 2011)

2.3.3 Additive manufacturing

Additive manufacturing (AM) is widely used in industry to produce complex components and tools. AM processes are defined as "manufacturing processes in which the workpiece is built up in successive layers or units" according to VDI 3405 (2014). DIN EN ISO/ASTM 52900 classifies AM processes into seven categories (**Fig. 2.4**).

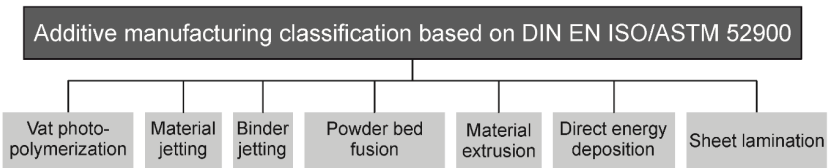

Figure 2.4: AM classification based on DIN EN ISO/ASTM 52900

Direct energy deposition and sheet lamination are briefly described in the following sections, as they are the focus of this thesis.

2.3.3.1 Direct energy deposition (DED)

Direct energy deposition is an AM category in which typically the concentrated heat source is used to melt the feedstock material to create a melt pool for building three-dimensional features or parts. The focused heat source can be an electron beam, laser, gas tungsten arc, or plasma, and the feedstock materials are either in powder or wire form. The DED process also has unique properties, such as a high degree of control over the grain structure and the ability to produce high-quality parts. DED processes are commonly used for repair purposes. For all the different heat sources, the feed of filler materials can be coaxial or off-axial. The utilization of a laser or an electric arc as a heating source is the most common method for DED processes. However, the feed material could be only wire for the arc as the energy source (Wire Arc Additive Manufacturing, WAAM). The defects that occur in a laser DED process include porosity, lack of fusion, cracks, residual stresses, and poor surface quality. The main

reasons for such defects on the DED process are related to the selection of improper process parameters (laser power, feed rate, powder mass flow, etc.) and also impurity of feedstock material. (Sreekanth et al., 2020)

Laser Metal Deposition (LMD) is a process that uses the laser as the energy source and powder as the feedstock material. In this process, metal powders are carried by inert gas (nitrogen or helium) to the focal distance of the laser. The high energy of the laser melts the powder and deposits it on the substrate surface under shielding gas (**Fig. 2.5**). The subsequent mixture of molten substrate and feedstock material during the laser metal deposition process defines the dilution ratio (∅). The dilution ratio ∅ is defined as (Jasim et al., 1993):

$$\emptyset = \frac{A_D}{A_D + A_c}, \tag{2.1}$$

where A_D is the deposited area and A_c is the material mixture area with the substrate after deposition. The higher the dilution ratio, the greater the penetration of the feedstock material on the substrate. The desired dilution ratio varies depending on the requirement. For example, the desired dilution ratio for coatings is 3 to 5 % (Syed et al., 2005). The chemical composition of the deposited material is also affected by dilution (Atamert and Bhadeshia, 1989).

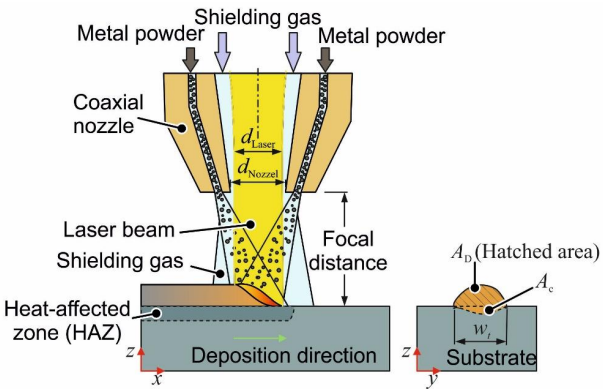

Figure 2.5: Principle of laser metal deposition with coaxial feeding system

The main LMD process parameters are laser power (P), scanning speed or feed rate (f), powder feed rate or mass flow ($\dot{m}$), substrate preheat temperature (T_0), the working distance (W_d), powder grain size, cooling time, and intervals, the flow of carrier and shielding gas flow, track overlapping value and build direction increment (Z increment), and finally the deposition strategy (Bax et al., 2018). The main parameters that affect the surface roughness of the deposited areas are material type and size, process

parameters such as laser power, feed rate, powder mass flow, scanning strategy, and layer height and toolpath overlap.

The deposition rate ($\dot{D}$) is the mass of utilizable feedstock material that can be deposited in one minute. This parameter indicates the efficiency of the DED process. Each variation of the DED process has specific characteristics (**Table 2.1**), which are discussed in detail below. Laser-based DED offers advantages, e.g., low distortion and surface damage and higher deposition resolution than arc-based DED processes such as WAAM (Pinkerton, 2010).

Table 2.1: Comparison of the laser-based DED with WAAM

Energy source	**Laser**		**Arc**
Feed material	**Wire**	**Powder**	**Wire**
Work scale	large scale[1]	small scale	large scale[2]
Complex shapes	lower	higher[3]	lower[4]
Hardness	340-385 HV 0.3[5]	43-45 HRC	44-46 HRC[6]
Surface damage	lower[7]	lower[7]	higher[15]
Residual stress	lower[8]	lower	higher[2,4,8]
In-situ mass flux variation	impossible	possible	impossible
Deposition rate, (g/min)	lower[9] (10.2)	lower[9] (7.8)	higher[4] (16.67 to 66.67)
Dilution ratio	< 20 %[9]	< 5 %[9]	40 - 50 %[10]
Feedstock material size	limited[11]	less limited[11]	limited
R_a (µm)	40-60[12] 1.5-36.3[5]	70-90[12]	500[13]
Material efficiency	higher[11]	lower[11]	higher
Cost	lower[1,14]	higher[1,14]	lower[4]

[1] (Ding et al., 2015) [2] (Wu et al., 2018) [3] (Dutta et al., 2011)
[4] (Williams et al., 2016) [5] (Kelbassa et al., 2019) [6] (Xu et al., 2018)
[7] (Pinkerton, 2010) [8] (Li et al., 2018) [9] (Syed et al., 2006)
[10] (Pickin et al., 2011) [11] (Lorenz et al., 2015) [12] (Syed et al., 2005)
[13] (Martina et al., 2012) [14] (Cunningham et al., 2018) [15] (Verma et al., 2022)

Laser-based DED with a powder, like the LMD process, allows the manufacturing of complex shapes on a small working scale with a relatively high hardness characteristic. Because the focused energy is applied to a concentrated area, surface damage, and residual stresses are lower compared to arc-based DED. The use of powder as a feedstock material also provides a unique advantage in that the mass flow can be varied and the different materials with different grain sizes can be easily mixed. However, the low material efficiency due to the volume of powder not being completely melted and bonded, the high cost of powder production, and safety considerations are the main disadvantages of this process.

Setting the proper process parameters during LMD is critical to achieve a successful process. The properties of the deposited surface can be affected by variation of each parameter. The effect of various parameters on surface roughness, dimensional accuracy, residual stress, and porosity is summarized in **Table 2.2**.

Table 2.2: Effect of LMD process parameters on deposited area quality

By increasing the:	Surface roughness	Dimensional accuracy	Hardness	Residual stress	Porosity
Laser power	improve[1]	decrease[3]	decrease[3,4]	increase[8]	decrease[5]
Feed rate	improve[2] decrease[1]	-	increase[4]	-	-
Powder mass flow	decrease[2,4]	-	-	-	increase[7]
Powder grain size	decrease[9]	-	-	-	-

[1](Gharbi et al., 2013) [2] (Craig et al., 2021) [3] (Feenstra et al., 2020)
[4] (Mahamood et al., 2015) [5] (Sreekanth et al., 2020) [6] (Zhong et al., 2015)
[7] (Gäumann et al., 2001) [8] (Shamsaei et al., 2015) [9] (Kong et al., 2007)

One of the main drawbacks of AM products is the surface roughness of the manufactured parts, especially in DED. Different process parameters affect the surface roughness of AM parts. The parameters influencing the properties of DED parts can be divided into two groups: first-order and second-order factors. The first-order factors are laser power, feed rate, and powder mass flow. Despite the second-order factors, such as focal distance, pause time between passes, and shielding gas velocity and volume, the first-order factors can be easily varied (Gharbi et al., 2013). The effect of the first-order parameters showed that laser power (320 to 500 W) and feed rate (0.1 to 0.6 m/min) affect waviness and surface roughness. For a constant powder mass flow (1 g/min), the high laser power and lower feed rate resulted in better surface roughness, i.e., lower waviness and better surface finish. In contrast, Craig et al. (2021) concluded that the surface roughness of H13 hot work tool steel processed by LMD improves with increasing feed rate (at a maximum feed rate of 700 mm/min and laser power of 400 W). The low mass flow outcomes in better surface roughness because the powder melts completely and deposits properly on the surface (Mahamood et al., 2015).

The effect of powder grain size on surface roughness is correlated with laser spot diameter. When the powder spot size (the peak concentration of powder at the focal point) is larger than the laser spot diameter, it results in poor surface roughness (Kong et al., 2007). Additionally, powders smaller than 20 µm cause an inhomogeneous surface. The small size of the particles tends to coagulate inside the nozzle, and then the high pressure of the carrier gas ejects the coagulated powder, resulting in the pulsation of the powder and, consequently, the poor surface roughness. The powder grain size between 44 and 88 µm for Inconel 625 powder shows the right size where the deposition

efficiency improves in addition to the surface roughness. The shape accuracy decreased with increasing laser power for 316L and Inconel 625 powders. In this study, the laser power varied between 1200 and 2000 W. It is also concluded that the higher laser power decreases hardness due to the resulting laser melt pool size and, so, longer solidification time (larger grain size). The higher feed rate (0.1 m/s) by deposition of Ti6Al4V results in higher microhardness from about 368 to 408 HV0.5 (Mahamood et al., 2015).
The shielding gas affects the amount of powder delivered to the melt pool and, therefore, the coating thickness. The higher the shielding gas flow rate, the greater the thickness of the deposited layer. However, the higher shielding gas flow rates tend to direct the powders away from the melt pool surface (Shamsaei et al., 2015).

Residual stress is one of the most critical challenges in AM parts, especially in DED parts. Residual stresses are generated in almost all manufacturing processes, especially in the melt phase joining process, such as AM. The residual stresses play an essential role in the fatigue life, crack propagation, and effective yield stress of the manufactured components (Macherauch et al., 1973). Some of the residual stresses remain even in the absence of external forces or thermal gradients. After fabrication, the resulting internal forces and moments are balanced as a system in the fabricated part. Type I (macro stresses) and Type II and III (micro stresses) are three subcategories of residual stresses based on the length scale. Type I is at the macro level and causes irregular strain distribution. Microscale stress (Type II stress) exists due to anisotropy of the material at the grain scale. Nanoscale dislocations and coherency cause Type III stresses. Since type II and III residual stresses have an insignificant effect on the macroscopic mechanical properties of the material and the measurements require very accurate and specific equipment, Type I residual stresses are mainly studied (Macherauch and Kloos, 1989). Compressive residual stresses (negative values) are particularly desirable in tools because they increase fatigue life by limiting crack growth and propagation (Milella, 2013). Like the welding process, the particular thermal cycle (rapid heating-cooling) of additive manufacturing develops residual stress in AM components. To some extent, the formation of residual stresses in AM and welding follows a similar formation mechanism (Kou, 2020).

In addition to laser power, laser head feed rate, powder mass flow, the initial substrate temperature, scanning strategies, and cooling time (dwell time) are effective parameters on residual stresses in the LMD process (Tebaay et al., 2020). The laser scanning direction in 316L powder shows an insignificant effect on the magnitude of residual stresses investigated by Rangaswamy et al. (2005). The impact of cooling/dwell times on residual stresses depends on the deposited material. The deposition of Inconel 625 material with a longer cooling time results in smaller residual stress amplitudes. Conversely, a shorter cooling time causes the higher residual stresses in deposited Ti64 material (Wang et al., 2017).

Preheating the substrate is one solution to reduce the unwanted residual stress, in addition to heat treatment of AM components (Li et al., 2018). The maximum residual stress of Co-based alloy powder deposited on die steel Cr12 (1.2080) reduces by 20 % from 350 MPa at room temperature (RT) to about 280 MPa at 600 °C in the deposited area. However, for nickel-based powder (Ni60A), the residual stress is reduced by only 6 %, showing an insignificant effect (Jiang et al., 2016). The preheating of the bulk substrate for heat-treated steel (36CrNiMo4) causes the formation of a homogeneous dendritic structure of the deposited layers, which is not the case for the non-preheated substrate for co-alloy powder (Stellite®1) (Alimardani et al., 2010). The preheating of the substrate leads to a reduction in the hardness of the deposited material due to an increase in ferrite in low alloy steel powder (12CrNi2), as shown by Ding et al. (2018). For 316L and Inconel 625 powders, the preheating prevents the initiation of cracks when joining dissimilar materials in LMD (Meng et al., 2020). It is also shown that the preheating method, called laser synchronous, improves the microstructure of the deposited material. In this method, the substrate or deposition areas are preheated with a laser beam to apply the initial or subsequent deposition track.

There are several methods to measure the residual stress, such as the curvature of hole drilling, X-ray diffraction, and neutron diffraction (Li et al., 2018). The application of X-ray diffraction is one of the most common and well-established methods for measuring residual stress. This method is a non-destructive, non-contact, and accurate measurement and is relatively inexpensive compared to neutron diffraction (Hauk, 1997). Residual stresses can be measured to a depth of 20 µm with an accuracy of ± 20 MPa by X-ray diffraction (Withers and Bhadeshia, 2001). The residual stresses in this method are determined with Bragg's law (Bragg and Bragg, 1913) and $sin^2\psi$ method. A comprehensive explanation of the principle of measuring X-rays with $sin^2\psi$ method can be found in Withers and Bhadeshia (2001).

2.3.3.2 Sheet lamination

In sheet lamination or Layer Laminated Manufacturing (LLM), three-dimensional objects are produced by cutting the two-dimensional cross-section of the sheets and stacking the adhesive-coated sheets to produce the target geometry. In sheet metal lamination, the laminations can be stacked in either a vertical or horizontal orientation (vertical and horizontal lamination). Vertical lamination stacks the laminae parallel to the part axis. This method automatically supports the embossing in the laminated part because the vertical sheet is supported by the laminae (Bryden et al., 2000). Vertical lamination (**Fig. 2.6a**) often encounters over-elastic deformation that affects the geometry of the target part, which leads to plastic deformation and subsequent part failure. Vertical lamination also requires lateral support (Yoo and Walczyk, 2005). Horizontal lamination (**Fig. 2.6b**) limits the ability to create islands and embossments in part due to the orientation of the laminations. The surface roughness of the horizontal

laminated parts is better than that of the vertical one, and more material can be saved by horizontal lamination, where the waste material from the cavity can be used to laminate the core part. In most cases, the horizontal orientation is preferred for flat parts (Bryden et al., 2000; Dickens, 1997).

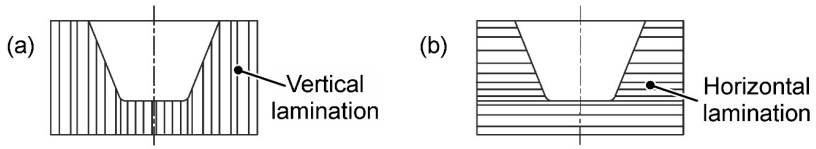

Figure 2.6: (a) Vertical lamination, (b) horizontal lamination

The low manufacturing time, lead time, and cost are sheet lamination's main advantages, making this technique suitable for rapid prototyping and tooling. Sheet metal lamination also allows for the combination of different materials and/or laminates of different sheet thicknesses, which can also be interchanged if necessary (Pepelnjak and Kuzman, 1998). The use of sheet lamination for tooling production was first patented by Hart (1942) to manufacture shoe molds. In 1954, another patent was filed to make hydroforming dies using sheet metal laminated tooling (Clevenger et al., 1954). In the automotive industry, the application of sheet metal laminated tooling dates back to the early 1980s for the manufacture of the metal laminated stamping tool by Nakagawa and Suzuki (1981). Sheet lamination also allows the positioning of sensors for innovative tooling (Cao et al., 2019). Complex cooling and heating channels can be initiated in sheet laminated tools. Bryden et al. (2002) demonstrated the implementation of cooling channels in laminated tool for functional testing at 900 °C for the aerospace industry. Complex cooling channels have been successfully implemented in injection molds produced by the metal laminate tooling method (Bryden and Pashby, 2001).

Despite its advantages, sheet lamination has disadvantages, making it take longer to develop than other AM techniques. The possible reasons could be the following:

- bonding laminates with sufficient strength to meet production requirements is challenging.
- automating of this process is challenging, especially for complex geometries.
- finally, the design of angled or curved surfaces in sheet lamination results in a jagged and inhomogeneous surface called the stair-step effect, i.e. the non-smooth and edged surfaces due to stacking. This stair-step effect depends on the layer thickness and the angle of the surface. The thicker the sheet metal layer, the greater the stair-step effect and, consequently, the greater the surface roughness (Bryden et al., 2000).

To solve the lamella bonding challenge, various joining methods such as bolting, welding and laser welding, soldering, diffusion bonding, adhesive bonding, hydraulic

jaws, form fit, or pull cables. The application of the required tool determines the bonding method, e.g. laser welding, bolting or bonding by adhesives, which provide sufficient bonding strength for sheet metal forming tools and core boxes. Strong bonding by diffusion welding is required for injection molding and die-casting tools (Himmer et al., 2003). The working temperature during the experiment is critical in selecting the type of bonding method. For low-temperature (< 250 °C) experiments, soldering or brazing can be used as the joining method. For high-temperature conditions, around 900 °C, hot isostatic pressing is required (Bryden et al., 2000). The development of faster computer processing power, supported by more advanced computer-aided design (CAD) and computer-aided manufacturing (CAM) software packages, has led to the possibility of automating complex shapes at the design and production stages (Bryden et al., 2000).

However, the main challenge in laminated tooling is eliminating or reducing the stair step effect. Laminates can be cut in two ways (**Fig. 2.7a**) where the corners of the sheet are in contact with the nominal geometry or angle of the curve.

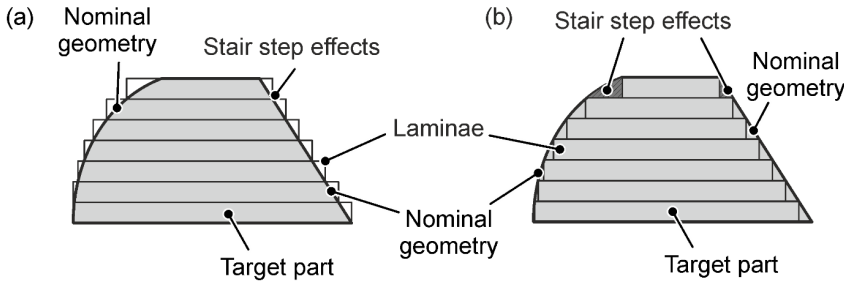

Figure 2.7: Two possible methods of cutting of laminae (a) over-length method, (b) short-length method

In an over-length method, the target geometry of the part is inside the laminations, and the corners of the underside of the laminations are in contact with the nominal geometry (Fig. 2.7a). In this method, the extra sheet must be removed by subtractive processes such as milling or turning. In the second or short-length method (**Fig. 2.7b**), the target part geometry is outside the sheets, and the sheet lengths are shorter than the target part width/length (horizontal/vertical lamination). In this case, in order to achieve the target geometry, the void areas of the stair step areas would need to be filled with additional material.

The elimination/reduction of the stair-step effect of metal-laminated tools can be divided into three groups: no pre-/post-processing, pre- and post-processing, as shown in **Fig. 2.8**. According to Kleiner and Krux (2001), the use of an intermediate layer as a soft layer or elastomer between the laminated tool and the blank is a possible solution to avoid pre-/post-processing. The interlayer should have high elasticity, high elongation

at break, low hardness, and high shear strength. The study showed that only small step sizes can be successfully eliminated by this method, which limits manufacturing flexibility. Profiled Edge Laminae (PEL) tooling or slant cutting of laminae is a method of pre-processing laminae prior to stacking developed by Weaver (1991). The laminae are stacked in an array, with the top of each sheet uniquely profiled and sloped based on the target curvature. This method is mainly used for vertical lamination (Walczyk and Hardt, 1994).

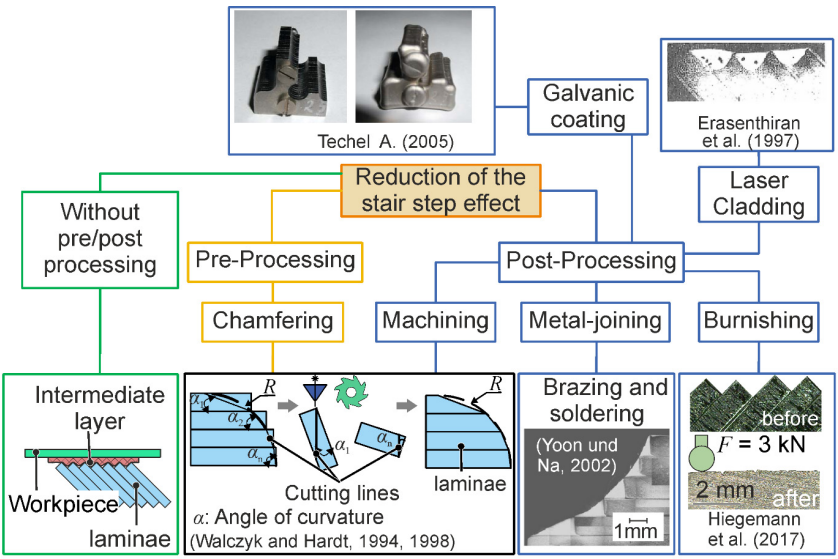

Figure 2.8: Classification of the existing methods for reduction of the stair step effect

The top edge of the laminae is profiled by cutting processes such as laser, wire EDM, or abrasive water jet (AWJ) cutting. The main disadvantage is the high effort required to maintain the profiling when moving from the design step to the manufacturing step (laminate clamping and cutting tool alignment), which increases manufacturing time and cost. Choosing the right laser power for profiling is another challenge of this method (Walczyk and Hardt, 1998). Yoo and Walczyk (2005) developed an advanced automatic cutting model for a PEL to reduce the profiling effort. The most common method of eliminating the stair-step effect is machining. Kunieda and Nakagawa (1985) used this method to remove the stair-step effect in manufacturing metal-laminated deep-drawing dies. The study shows that polishing or grinding is still required after machining. Diffusion bonding has also been shown to be a suitable joining method for laminated dies. A combination of chamfering and machining of the laminate to manufacture stamping dies was studied by Walczyk and Hardt (1998). However, this combined

method is more complex and costly. Metal laminated tools post-processed by chamfering and machining always have the possibility of delamination during operation because there is no layered bonding in the contact area between the workpiece and the tool. The application of brazing and soldering to fill stair steps of 1 mm low-carbon steel sheets with solid filler material is also investigated (Yoon and Na, 2005). Since brazing and soldering do not penetrate into the substrate, the exact amount of solid filler material can be determined in this method. Nevertheless, the lap shear stress results show maximum tensile shear stress of 137 MPa and 21 MPa for furnace brazing and dip brazing, respectively. It is shown that the maximum hardness is just under 50 HV without adding particles to the filler material. Hardness can be increased up to 600 HV by adding carbide particles after heat treatment, improving mechanical properties and increasing production time. However, there is no need for machining to improve surface roughness.

Electroplating sharp contours and achieving closed contours (spaces between laminations) with a homogeneous surface is another way to reduce the stair-step effect (Techel, 2005). Galvanic coating (electroplating) and the application of an adhesive metal layer in stair-step areas require complex pre-treatment. Electroplating with nickel, for example, has no significant thermal effects on the part.

In addition to machining, forming an uneven surface (stair-step areas) can decrease surface roughness. Despite the machining processes, ball/roller burnishing is a chipless finishing process. The homogeneous and smooth surface in ball/roller burnishing is achieved by high contact pressure supported by hydrostatic pressure between the ball/roller and the uneven surface (**Fig. 2.9a**). The high contact pressure causes plastic deformation of the metal surface under pressure, resulting in a smoother texture. The functional operation of the ball burnishing tool is shown in **Fig. 2.9b**.

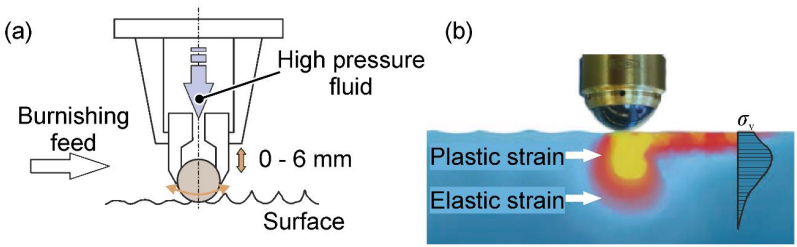

Figure 2.9: (a) Principle of the operation of ball burnishing, (b) applied vertical stress distribution by the ball burnishing (Röttger, 2003)

It is shown that compressive stress can be induced in the heat-affected zone (HAZ) to reduce hot cracking. The application of ball or roller rolling to welds could be either directly after welding, called in-situ rolling, or after cooling the weld, called post-weld

rolling (Adams et al., 2020). Post-weld rolling is more effective than in-situ rolling in reducing residual tensile stresses in friction stir welding (Altenkirch et al., 2009).

The subsequent yielding of the weld bead material during cooling renders in-situ rolling ineffective in reducing residual stresses (Coules et al., 2012). Colegrove et al. (2017) combined rolling with the WAAM process. It is concluded that rolling reduces the peak residual stress and distortion, and by increasing the rolling force, the hardness also increases. It is shown that in-situ rolling does not affect distortion. Hiegemman et al. (2016) also used the advantages of ball burnishing to form and smooth the stair-step effect. In this work, the DC04 steel sheets with a thickness of 1 mm and a length difference of 1 mm are stacked (**Fig. 2.10a**). The laminations are ball burnished under 45° (**Fig. 2.10b**) with three different rolling forces. The results of Vickers hardness under different rolling forces show that the rolling force of 3 kN increases the hardness by 75 % (**Fig. 2.10c**). This increase is due to the fact that the main advantage of this process is the work hardening of the deformed surfaces. Even with the higher rolling forces, the laminations' surface roughness is insufficient for deep drawing applications.

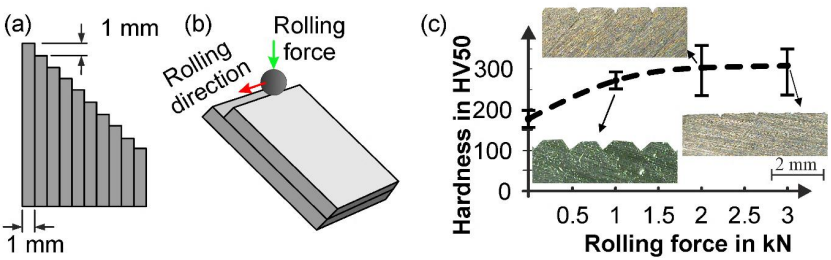

Figure 2.10: (a) Dimension of laminae (b) rolling force and direction (c) hardness curve

For the first time, Erasenthiran et al. (1997) briefly investigated the application of laser cladding to eliminate the stair-step effect of simple laminates using Ni powder as the cladding material. In this study, two different deposition routes are followed. In the first route, the almost exact amount of powder was individually tailored and placed in each stair-step effect, called “replaced powder”. In the second route, the steps are deposited regardless of the volume of the steps, called blown powder cladding. Blow powder cladding results in lower porosity and produces a smoother surface than pre-placed powder. However, it has a rough surface roughness. Laser remelting of the deposited surfaces is also briefly attempted in this work. Laser polishing is an exciting method for surface treatment in the industry due to its high operational speed, flexibility, and localized surface treatment (Bhaduri et al., 2017). Since it is a non-contact process, it would accelerate the automation possibilities (Dadbakhsh et al., 2010).

Laser polishing is classified into three groups: laser large-area ablation, laser localized ablation, and polishing by remelting (Krishnan and Fang, 2019). In large-area ablation, the laser beam has an angle of 85° to the target surface, and the large area is under the laser beam. This method is mainly used for chemical vapor deposition (CVD) of diamond films. In contrast, pulsed laser radiation has been used for localized ablation, where the ablation of the profile peaks is controlled (by controlling the power density). This method is very costly because precise positioning of the laser beam at the profile peaks requires very accurate measurement equipment. Compared to other methods, laser polishing by remelting has a high degree of automation (no need for skilled labor), short processing time, and results in no change in surface shape. Laser polishing also has no environmental impact compared to other processes, such as grinding and burnishing, which produce waste and chemicals (Willenborg, 2011). The principle of laser remelting is shown in **Fig. 2.11**. Shallow Surface Melting (SSM) and Surface Over Melting (SOM) are the two main mechanisms of surface roughness reduction in remelting. The dynamics of high-temperature metal flow create the SSM region. The metal flow is forced into micro-roughness and fills the existing valleys. This causes the melt level to be lower than the peak-to-valley distance, which laser parameters can influence.

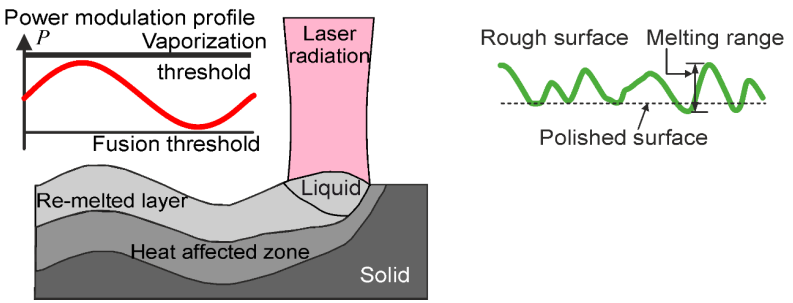

Figure 2.11: Principle of laser polishing (Krishnan and Fang, 2019)

The melt pool behavior is a function of the energy density of the laser beam. As the laser power increases, the melt pool thickness increases and exceeds the roughness height. It leads to the transformation of the entire metal surface into a melt pool. At higher laser powers, which results in a temperature above the material's melting point, the molten material pulls away from the solidification front and forms waves on the surface. This phenomenon is called surface overmelting (SOM) (Ramos et al., 2002; Krishnan and Fang, 2019). The generated surface roughness after laser polishing, besides the initial state of the surface such as the original surface roughness, the homogeneity of the surface and the thermophysical material (thermal conductivity, viscosity, other parameters), is a function of various parameters such as the type of laser (fiber, CO_2, diode, excimer), the beam diameter and intensity, the interaction time between the laser

beam and the target surface (Krishnan and Fang, 2019). Since laser polishing is a non-contact process, it provides high accessibility. Laser polishing of free-form surfaces is of interest to the industrial and medical sectors. **Fig. 2.12** illustrates the application of laser polishing to components of a heart pump where the laser is moving on complex shapes.

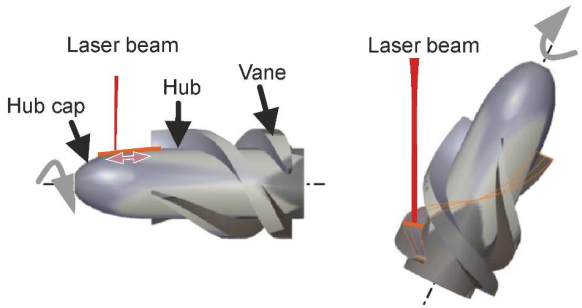

Figure 2.12: Example of laser polishing of a heart pump component hub and hub cap (Temmler et al., 2010)

Some other post-processing of AM parts, such as etching, electropolishing, plasma spraying, or sandblasting (Bhaduri et al., 2017), can be used for AM parts, which are beyond the scope of this study.

Failure modes and strength of laminate for tool design

Several failure modes are possible for laminated tooling. The primary failure is the lack of a strong bond between the laminae, especially under process forces. The failures (**Fig. 2.13**) could be due to stresses from service process forces such as tension, shear, peeling (delamination), or a combination of several stresses.

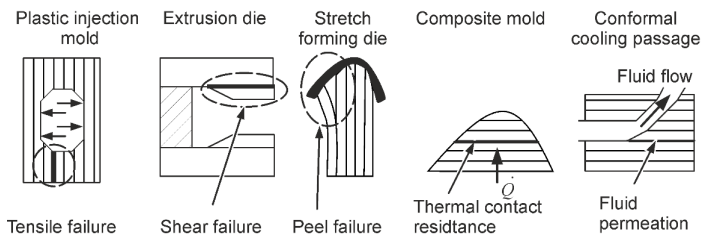

Figure 2.13: Failure modes in laminated tooling (Walczyk and Dolar, 1997)

Thermal contact resistance and lack of proper sealing are the other possible failure modes in laminated tools (Walczyk and Dolar, 1997). The other criterion to consider is the stiffness of the laminations under process forces. The laminae should not break or

even plastify during the process. To this end, several methods have been developed to study the stiffness of the laminae, which will be discussed below.

The laminated sheets as mechanical structures can be considered as either a beam or a plate. The main difference between a beam and a plate is the width. The beams have a much smaller width compared to the plates. The beam theory calculates the beam as a one-dimensional element, although in reality it is three-dimensional. The Euler-Bernoulli beam and Timoshenko beam theories (Timoshenko and Gere, 1985) are more commonly used to study the beam.

In the Euler beam theory, the fourth-order differential equation of the displacement (u) is a function of the vertically distributed force (load per length) $q(z)$, the moment of inertia (I) and Young's modulus (E) as presented in **Eq. (2.2)**.

$$\frac{d^4u}{dz^4} = \frac{q(z)}{EI} \tag{2.2}$$

The Eq. (2.2) can be solved by applying the boundary conditions at the beginning and end of the beam. The main drawback of the Euler beam theory is that it is only valid for slender beams, and the length of the beam is much larger than its cross-section. It underestimates the deflection for short or thick beams because the shear deflection is neglected. By introducing the shear deflection, Timoshenko beam theory solved this problem by introducing the shear factor k. In Timoshenko's beam theory, the plane section remains plane but no longer perpendicular to the longitudinal axis (**Fig. 2.14**). This leads to a rotation angle of the normal to the mid-surface of the deflection θ_z. The governing Timoshenko beam equation is equal to:

$$\frac{d^2}{dz^2}\left(EI\frac{d\varphi}{dz}\right) = q(z), \tag{2.3}$$

$$\frac{dw}{dz} = \varphi - \frac{1}{\kappa AG}\frac{d}{dz}\left(EI\frac{d\varphi}{dz}\right), \tag{2.4}$$

where A is the cross-sectional area, G is the shear modulus, and κ is the Timoshenko shear coefficient (which depends on the cross-section geometry). The shear modulus is $G = -0.5\,E(1+v)^{-1}$ where v is Poisson's ratio. By combining these two equations and simplifying them, the bending moment (M_{zz}) and the shear forces (Q_z) can be calculated as follows:

$$M_{zz} = -EI\frac{\partial\varphi}{\partial z}, \tag{2.5}$$

$$Q_z = \kappa AG\left(-\varphi + \frac{\partial w}{\partial z}\right). \tag{2.6}$$

Besides Timoshenko's beam theory, there are other theories, such as Levinson's beam theory (Levinson, 1981) and other higher-order beam theories. The main difference is

the different way of calculating the shear stress, assuming that the cross-section is no longer plane. However, Timoshenko's beam theory still provides accurate results if the boundary conditions are fulfilled correctly.

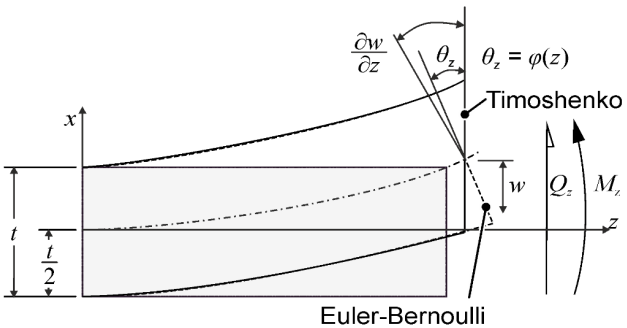

Figure 2.14: Timoshenko beam versus Euler–Bernoulli beam and deformation of the beam

Several studies have been conducted to analyze the strength of laminated tooling under process forces. There is a different analysis for vertical and horizontal laminated tooling. Walcyk and Hardt (1998) analytically explained the mechanical failure of the laminae for the vertical PEL laminated tooling. Due to elastic or possibly plastic deformation, the process forces on the vertical laminates lead to form errors in the laminated tool (**Fig. 2.15a**). Based on the Timoshenko beam theory, the individual sheets become unstable and begin to buckle or deform (**Fig. 2.15b**). The process forces applied to the individual sheet can be separated into buckling and bending forces (**Fig. 2.15c**). The total forming force of the blank on the laminae is the integration of the effective force F_{n} and the resultant perpendicular static friction force $\mu \cdot F_n$ at the contact area of the laminae and the blank, where μ is the coefficient of friction (Fig. 2.15c). Considering the total forming of $F_T = F_n \cdot \sqrt{(1+\mu^2)}$, the bending force ($F_{\mathrm{bending}}$) and buckling force ($F_{\mathrm{buckling}}$) are equal to $F_T \cdot \sin(\alpha - \tan^{-1}\mu)$ and $F_T \cdot \cos(\alpha - \tan^{-1}\mu)$, respectively. Based on Euler`s column buckling formula, the critical buckling force for rectangular cross-section can be determined as:

$$F_{buckling}^{critical} = \frac{\Gamma \cdot E \cdot b \cdot t^3}{12 \cdot a^2}, \tag{2.7}$$

where E is Young's modulus, b, and t are the width and thickness of the sheet, respectively. The free length of the beam is a. The coefficient factor Γ depends on the support condition in both ends. Therefore, the mechanical failures could be divided into buckling and bending. It is also concluded that the cutting forces should be considered by post-processing the stair step effects by the machining to avoid deformation and

shape errors. Later, multilayer beams subjected to horizontal loading were studied by Bareisis (2004).

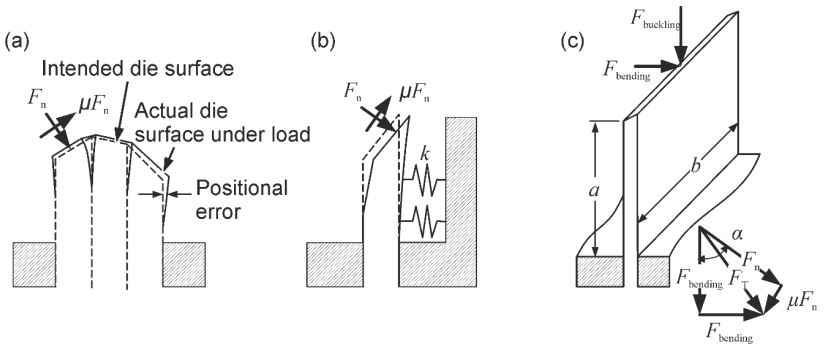

Figure 2.15: (a) Laminae under forming forces, (b) substitution of the supporting laminae, (c) single PEL sheet under bending and buckling forces (Walczyk and Hardt, 1998)

The results of an analytical method for determining the deformation of multilayer beam and its corresponding normal stress were in good agreement with finite element method (FEM) simulation results. In the proposed model, the laminated layers are considered as a single beam.

Hölker (2014) developed an analytical model for the laminated extrusion die (**Fig. 2.16a**). The derived analytical model consisted of a single cantilever beam under distributed vertical force supported by an elastic bed as a support (**Fig. 2.16b**).

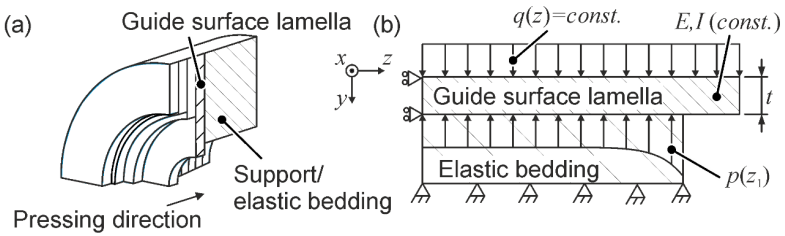

Figure 2.16: (a) Cross-section of the extrusion die, (b) simplified 2D model of the laminated extrusion die with BC (Hölker, 2014)

To validate the developed analytical model, FEM simulations are used, which showed only a 12 % deviation in von Misses stress values from the analytical model (**Fig. 2.17**). The main reason for this deviation is the dependence of the FEM simulation results on the mesh size and the discontinuity in the transition zone between the supported area and the free length in the cantilevered area. Yoon and Walczy (2005) developed a

software model for analyzing and manufacturing the structural integrity of PEL tooling with vertical layer orientation. The advanced software integrated CAD, CAM, FEM, and analytical models for PEL tool manufacturing. Compared to experimental work, the software results in a maximum deviation of 25 % for deflection error.

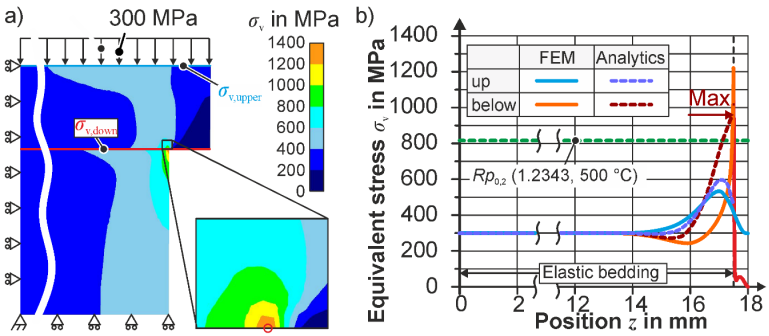

Figure 2.17: Comparing of analytical with FEM model (Hölker, 2014)

2.3.4 Hybrid additive manufacturing

In addition to economic and energy considerations, the increasing demands for new products for high accuracy, strength, and functionality lead to increased productivity of manufacturing processes. Considering that the parts also need to be produced in a short time, innovation increases. Integrating different manufacturing processes such as forming, machining, joining, and additive manufacturing can improve productivity. This integration, called hybrid manufacturing (HM), can overcome the limitations and constraints of individual processes. The terms "*hybrid processes*," "*hybrid manufacturing*," or "*hybrid manufacturing processes*" do not have a clear definition (Zhu et al., 2013). The term hybrid machining was first used by (Rajurkar et al., 1999) and comprehensively defined by (Aspinwall et al., 2001) as a process in which more than one subtractive methods are used independently on a single machine, or these processes are used simultaneously. However, other definitions exist (Rivette et al., 2007). The word "hybrid" can be defined as integrating different processes that significantly influence the properties of the target part (Lauwers et al., 2010). The International Academy for Production Engineering (CIRP) defines the hybrid process as (Zhu et al., 2013):

- integrated utilization or integration of various physical active principles, such as the application of laser in machining (Dandekar et al., 2010)

- combination of individual process steps as an integrated process, e.g., superposition of sheets during the incremental forming (Araghi et al., 2009) or use of laser for single point incremental forming (Duflou et al., 2007)
- integration of machines performing different processes at the same location (She and Hung, 2008)

Subtractive methods, especially computer numerical control (CNC) machining, are the only choice when high-quality parts are required. This method is costly and time-consuming. However, it requires highly skilled labor to generate the CAM program and evaluate the part's manufacturability. Rapid tooling concept can eliminate this step and accelerate the transformation of the design concept into the real part in a short time (Karunakaran et al., 2010). Considering additive manufacturing in integration with conventional processes, a new classification of hybrid manufacturing is proposed by (Pragana et al., 2021), as shown in **Fig. 2.18**. The new classification considers hybrid additive manufacturing to be sequential hybrid manufacturing integrated with conventional manufacturing processes. Additive manufacturing can be combined with conventional manufacturing methods of metal laminate tooling. Hybrid manufacturing can increase flexibility and robustness (Pragana et al., 2021). The hybrid additive manufacturing process can reduce the amount of waste material in conventional manufacturing (Lorenz et al., 2015).

In the subcategory of I (Fig. 2.18), processes require the combination of more than one energy source or tool, all of which must affect the target zone. The process could be used as an aid (I.A in Fig. 2.18), such as a laser to raise the temperature, or a process used to change the properties as an individual process (I.B in Fig. 2.18), such as bending the profile during extrusion. In the second group (II), the processes are used individually to shape the properties of the parts. The first subcategory (II.A) integrates conventional processes such as forming followed by machining or drilling. Hybrid additive manufacturing (HAM) belongs to the second subcategory of sequential hybrid manufacturing (HM). In HAM, additive manufacturing is always followed by at least one subtractive process, such as milling of the manufactured part from DED, or a forming process integrated with additive manufacturing, such as deposition of functional elements on the deformed sheet by single-point incremental sheet forming (Tebaay et al., 2020) or deep drawing of sandwich sheets with complex core structure (Rosenthal et al., 2022).

Integrating the forming process with metal additive manufacturing offers the opportunity to make the properties of the formed parts more robust and to reduce the production time of complex geometries. This hybridization extends the capabilities of conventional methods for customized products (Merklein et al., 2016).

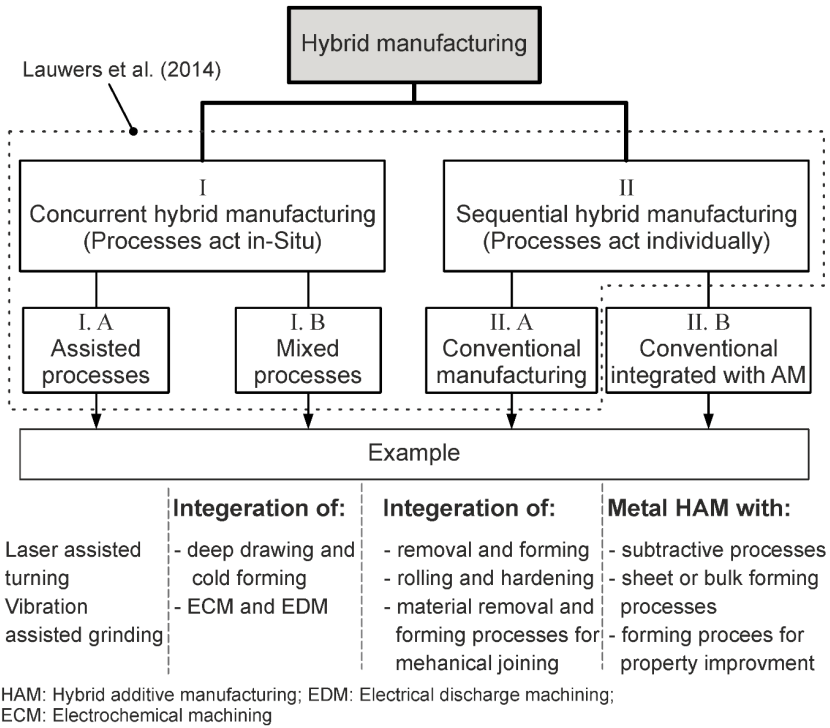

Figure 2.18: New classification of hybrid manufacturing (Pragana et al., 2021)

Hybrid additive manufacturing of forming tools

Increasing variation in the required parts, typically produced by forming processes, requires rapid small or medium batches tooling. The primary motivation for using hybrid additive manufacturing for forming tools is illustrated in **Fig. 2.19**. DED or Laser metal deposition is used to speed up the repair process chain for the existing tools (Graf et al., 2012). Conventional tool repair is mainly done by standard welding processes such as TIG (tungsten inert gas) or GMAW (gas metal arc welding). However, the main disadvantage of these processes is the high energy input, which requires post-weld heat treatment, which is time-consuming (Lant et al., 2001). Laser metal deposition has a lower dilution and energy input than conventional welding processes and does not require additional post-weld heat treatment. The use of the laser as an energy source increases the reproducibility of the deposited material and lends itself to automation (Graf et al., 2012).

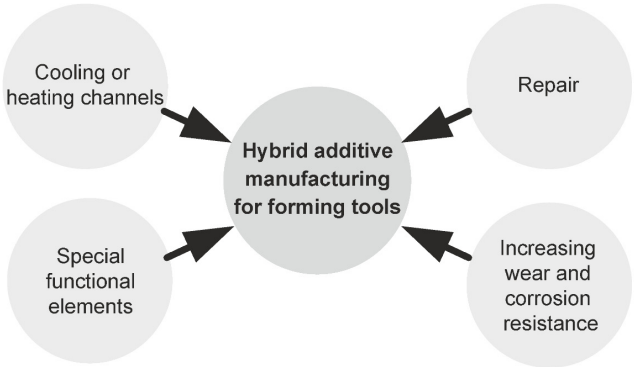

Figure 2.19: Motivations for using hybrid additive manufacturing for forming tooling

Table 2.3 compares the conventional welding process with DED for repair purposes on various criteria. Also, repairing with conventional methods, i.e., TIG/Plasma or Gas Tungsten Arc Welding (GTAW), provides higher deposition rates, but the metallurgical characteristics are poor. This is not the case with DED due to the low dilution and localized treatment. (Saboori et al., 2019). Applying the DED process for repair and restoration reduces the lead time and cost, thus reducing greenhouse gas emissions (Ahn, 2021). Using the DED process to repair the turbine blade can reduce 68.1 % of the total energy consumption compared to manufacturing a new turbine blade. This amount of energy saved reduces ca. 72.5 % of greenhouse gas emissions (Wilson et al., 2014).

Table 2.3: Conventional repair methods compared with DED (Saboori et al., 2019)

Criteria	TIG/ Plasma	GTAM	Cold spray	Thermal Coating	DED
Deposition rate	**	****	**	*****	****
Portability	****	****	*	**	**
Metallurgical properties	**	*	**	**	****
Set up time	***	**	***	**	****
Post-heating treatment	***	**	***	**	***
Cost	**	*	**	**	***

Since most metal-based additive manufacturing processes allow almost free choice of materials, DED processes offer the opportunity to deposit one or more highly wear-resistant layers on the surface of parts where wear or corrosion may occur. Forging, hot stamping, and rolling tools enhanced by the DED process show lower or undamaged areas. The application of laser metal deposition to add the additional surface as a

resistance layer is called Laser Surface Alloying (LSA), which has the same principle as LMD. The alloying material (alloy powder) applied to the deposited surface by laser energy completely dissolves the alloying materials in the melt pool. The target surface is enriched with the required alloying elements (Sharkeev et al., 2016). From an economic point of view, LSA reduces the cost of alloying elements because only the required area can be enhanced with high-strength elements instead of the entire part. Yet, it also saves energy and cutting tool costs during production (Chatterjee et al., 2008). The main advantage of this method over other competing methods is the possibility of rapid quenching. It results in smaller grain size and the creation of metastable state structures (Kwok et al., 2006) or configurationally frozen metastable state structures (Turnbull, 1981). In several forming processes, such as hot stamping or deep drawing at elevated temperatures, it is essential to control the near-surface temperature of the tool through complex cooling and heating channels. In the hot stamping process, it is essential to reduce the blank temperature at a cooling rate of 27 k/s (Karbasian and Tekkaya, 2010). Additive manufacturing processes, such as powder bed fusion, can produce complex cooling channels; however, the manufacturing time is long (Röttger et al., 2023). The complex cooling channel can be manufactured by combining the pre-machined substrate (bottom side of the tool) and depositing the internal complex cooling channel by LMD as the top side of the tool (Popov and Fleisher, 2020). A relatively complex conformal cooling channel has been successfully manufactured by depositing the ASI H13 powder (similar to Ferro55) on the pre-machined channels on the bottom side of the tool (Cortina et al., 2018). The new hybrid method is able to produce the cooling channels close to the surface of the hot stamping punch, ca. 4.5 mm distance to the tool surface, without the additional hardening step (Komodromos et al., 2022) required by the conventional method, which is 6.4 mm (Lv et al., 2016).

Compared to conventional composites, the DED process using powder as filler material allows maximum tailoring of the graded composition, in addition to tailoring the microstructure based on the required properties (El-Galy et al., 2019; Liu et al., 2020). The fabrication of thin-walled functionally graded material (FGM) from 100 % titanium to about 95 vol.- % TiC without any crack formation was possible by LMD (Xia et al., 2020). The functional elements can be generated in a short time by DED on the forming tools. Since the DED process does not require special fixtures and tools, the functional elements can be implemented in locations accessible to the head of the DED machine. The application of Ti-6Al-4V powder by laser beam melting on Ti-6Al-4V metal sheets to fabricate the functional elements showed an 88 % higher shear bond strength than conventional methods (Schaub et al., 2016). No specific study was found in the literature on the use of functional elements of forming tools. DED also offers the possibility of increasing the local strength of the tool by depositing high-strength materials. The locally reinforced AA 6016 sheets are successfully subjected to hole-flanging without

new tooling. The deposited support allows the utilization of the formed part by reducing the total weight (Bambach et al., 2021). With conventional reinforcement methods such as spot welding or other adhesive methods, the risk of corrosion or poor bonding between the target part and the patch is high, limiting design freedom. This concept can be extended to the fabrication of the forming tools. The combination of laser metal deposition with sheet lamination and ball burnishing has been patented by Hölker and Tekkaya (2018). In this patent, the stepped areas caused by sheet lamination are filled with the laser metal deposition process. Ball burnishing is used to smooth and improve the surface roughness quality of the deposited areas.

2.4 Summary

In addition to a brief overview of sheet metal forming (especially deep drawing), surface roughness parameters, additive manufacturing, and sheet lamination, different methods for existing techniques to reduce the stair-step effect are presented. It is shown that integrating conventional machining processes with additive manufacturing (AM) processes can mitigate the inherent limitations of both methods in producing complex parts and reduce the design and manufacturing constraints. Hybrid additive manufacturing also has a lower CO_2 footprint and offers the possibility of realizing rapid manufacturing.

The use of sheet lamination as a rapid tooling method is limited due to the stair-step effect. The main drawback of existing sheet lamination methods to reduce or eliminate the stair-step effect is the difficulty in attending to existing automated remedial technologies. In addition, the application of laser metal deposition to reduce the stair-step effect was briefly investigated by Ersenthiran et al. (1997), and the application of ball burnishing to smooth surface roughness was patented by Hölker and Tekkaya (2018). However, further investigation of these methods for manufacturing forming tools, such as deep drawing tools, is needed.

3 Aim and scope

In conventional tool manufacturing methods, the raw materials in the form of blocks or cylinders are machined either by milling or turning or, if the tool already has a high hardness or a complex geometry, by electrical discharge machining to achieve the desired geometry and dimension (**Fig. 3.1a**). In most cases, the manufactured part must be hardened by additional heat treatment and is only ready for use if the hardening does not cause deviations in shape or geometry.

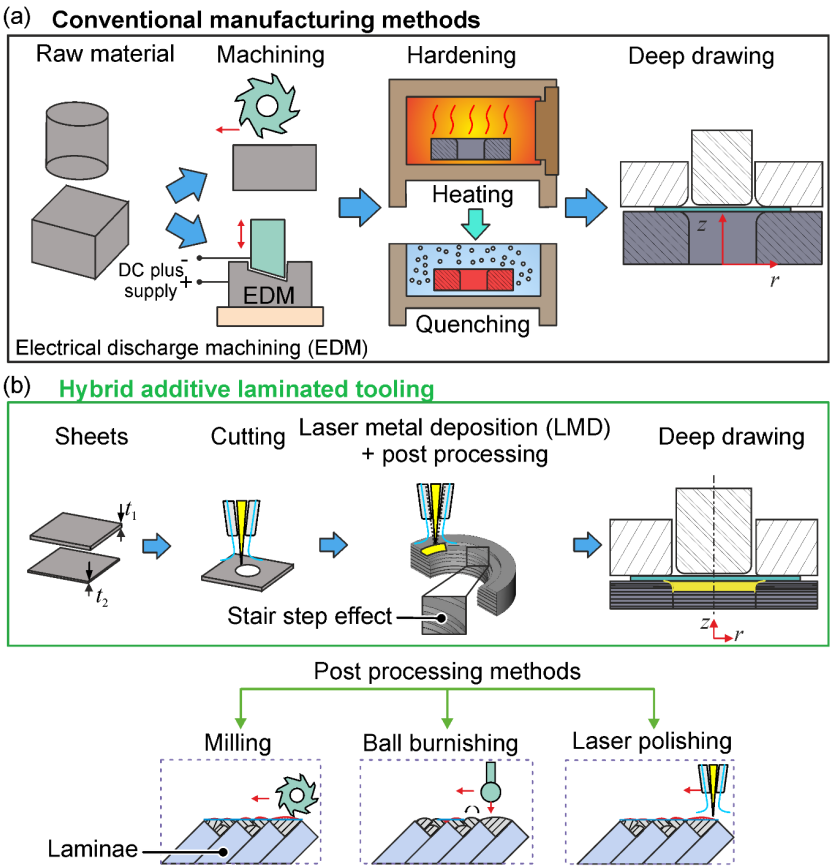

Figure 3.1: Comparison of (a) conventional and (b) hybrid additive manufacturing of laminated deep drawing tools route

The manufacturing time is directly related to the complexity of the geometries. The tools consisting of 3D cooling/heating channels or even places for sensors require more

manufacturing time. The more complex geometry results in more expensive machining and cutting tools.

Since the surface of the die undergoes high pressure during the forming process, only the surface of the die needs to be hardened at a certain depth to increase wear resistance and strength. In addition to the high-energy consumption, hardening the entire part equipped with sensors or cooling/heating elements is difficult since high temperatures could damage the existing sensors or functional elements. Developing a new manufacturing process that eliminates the hardening process facilitates the production of smart tools and reduces energy consumption and CO_2 emissions. In addition, the process must be able to produce the tool quickly to meet the requirements of rapid tooling and flexible manufacturing.

This work aims to develop a resource-efficient process chain for the flexible manufacture of deep-drawing tools using sheet metal lamination and additive manufacturing. The proposed hybrid additive manufacturing process starts with the preparation of the required metal sheets, which can be cut by laser or water jet to the desired geometry (**Fig 3.1b**). By stacking the sheets in the correct order, a stair-step effect is created. Laser metal deposition (LMD) reduces or eliminates the stair-step effect. The deposited surface is still rough; three post-processing methods are investigated to improve the tool surface roughness. The deposited area has high hardness and no additional hardening step is required. The use of LMD to reduce the stair-step effect offers the possibility of adaptively filling the various areas of the stair-step effect by in-situ adjustment of the powder mass flow rate. LMD also enables building on curved surfaces and structures (full 3D capability). It can also process multiple materials to create hybrid components. With this method, all the advantages of laminated tooling, such as the insertion of sensors or complex cooling and heating channels, can be used simultaneously, in addition to selecting different types of tool sheets. However, the development of such a tool requires a systematic design.

Three fundamental questions for developing a design guideline for hybrid additive manufacturing of laminated tooling are:

1. What are the considerations in the tooling design process?
2. What are the characteristic mechanical limitations of the hybrid process?
3. What is the CO_2-footprint of this process?

To answer the first question, it is necessary to study the laminated tools' stiffness and strength to guarantee that the tool doesn't fail during the deep drawing. For this, developing an analytical-based model helps to understand the stress distribution of the laminated tooling to ensure a proper material selection (chapter 6), including meeting cost criteria (chapter 7). Choosing proper process parameters and a deposition strategy needs a thorough investigation to achieve the best surface roughness and minimum form

deviation (chapter 6). It is also required to evaluate the effect of different post-processing methods on the surface roughness and hardness of the deposited areas (chapter 6). Since residual stresses are expected in AM parts, it should be analyzed whether preheating the tool sheets can improve the manufactured tool surface (chapter 5). The effect of different tool surface roughness on the frictional behavior of the tool also needs to be determined (chapter 6). Applying the developed knowledge to simple axisymmetric deep drawing tools ensures the functionality of tools (chapter 6). Since the LMD offers the possibility of manufacturing fully 3D surfaces, the effect of the process parameters on the different 3D strategies by manufacturing a demonstrator is studied (chapter 6). Finally, an economic as well as ecological assessment of the developed method is compared with the conventional and purely additive manufacturing processes for rapid tooling (chapter 7).

4 Materials and experimental methods

The following chapter presents the material properties of sheets used for tooling and deep drawing experiments. The chemical composition of metal powders used for LMD is also provided. Subsequently, different test setups consisting of standard conventional equipment and nonconventional test tools are also presented in detail.

4.1.1 Tool sheet (laminae)

The ferritic HC420LA (1.0556) belongs to conventional high-strength steels, according to DIN EN 10268 (2013). The cold-rolled low-alloy steel HC420LA is used in sheet thicknesses of 0.5 and 1.0 mm. The high-strength steel S355MC (1.0976) with a thickness of 2.0 mm, according to DIN EN 10149-2 (2013), is a thermomechanically hot-rolled steel for cold forming. The low content of carbon and microalloyed elements provides good weldability for both materials. The melting temperature of sheets is between 1480 – 1526 °C. The surface roughness of the sheets as delivered are $R_a = 0.77 \pm 0.1$ µm and $R_z = 4.26 \pm 0.4$ µm. The chemical composition of both sheets based on the provided company Kanuf Interfer Stahl service center GmbH of sheets is presented in **Table 4.1**.

Table 4.1: Chemical composition of the tool sheets in weight percentage %

Tool sheet	C	Mn	Si	P	S	Nb	v	Ti	Al
HC420LA	0.1	1.6	0.5	0.025	0.025	0.09	0.064	0.15	0.015
S355MC	0.12	1.5	0.5	0.025	0.02	0.09	0.2	0.15	0.015

4.1.2 Deep drawing sheets

The low carbon interstitial free (IF) steel DC06 (1.0873) and the high-strength steel HC380LA (1.0550), both 1 mm thick, are used for all deep drawing experiments. The chemical composition of the sheets based on the supplier is presented in **Table 4.2**.

Table 4.2: Chemical composition of the deep drawing sheets in weight percentage %

Deep drawing sheet	C	Mn	Si	P	S	Nb	v	Ti	Al
DC06	0.019	0.188	0.007	0.005	0.006	-	-	0.001	-
HC380LA	0.073	0.326	0.009	0.007	0.005	0.055	0.002	0.001	0.065

4.1.3 Tensile tests

All tensile experiments are carried out according to DIN EN ISO 6892 (2020). The tensile specimens are prepared according to DIN 50125 - H20 × 80 (2016). All tensile specimens are laser-cut using a laser-machining center LASERCELL TCL 1005 from company Trumpf. At least three specimens are tested at 0°, 45°, and 90° for each

material in the rolling direction (RD). The tensile tests are performed on a universal testing machine Z250 from the company ZwickRoell GmbH & Co. KG. The machine has a load cell for recording test forces up to 250 kN. Hydraulic grips grip specimens with parallel jaws. Tactile extensometers recorded the length and width changes. The parameters are selected according to DIN EN ISO 6892 1A (2020). The tensile tests are always run continuously for all specimens until failure. Before the test begins, the width and thickness of specimens are measured. The width of the specimen is measured at three different points using a digital caliper gauge. The thickness is measured analogously with a digital outside micrometer. The specimen grips are first closed with 50 bar closing pressure and then clamped with 150 bar clamping pressure to prevent the specimens from slipping during the test and thus avoid falsification of the results. In addition, a preload of 5 MPa is applied, which is permissible according to the standard. This slight preloading of the specimen also avoids errors in the strain measurement. The machine is operated using the "testXpert II" software. The results of the tensile test for all materials are presented in **Table 4.3**.

Table 4.3: Mechanical properties of the materials from the tensile test

Material	Angle to RD	$R_{p0.2}$ in MPa	R_m in MPa	A_g in %	$r_{2\text{-}20/Ag}$	r_n	Δr
DC06 (1 mm)	0°	168	297	24	1.7	1.69	0.52
	45°	175	303	22	1.4		
	90°	168	291	22	2.1		
HC380LA (1 mm)	0°	374	440	17	0.7	0.98	-0.15
	45°	379	433	17	1.06		
	90°	385	450	16	1.09		
HC420LA (0.5 mm)	0°	455	549	12	0.54	1.07	-0.85
	45°	439	511	14	1.49		
	90°	480	566	12	0.75		
HC420LA (1 mm)	0°	458	524	15	0.60	1.04	-0.65
	45°	450	509	15	1.37		
	90°	478	546	14	0.84		
S355MC (2 mm)	0°	417	481	17	0.72	0.94	-0.34
	45°	406	479	16	1.11		
	90°	430	497	16	0.82		

Where $R_{p0.2}$ is yield strength, R_m is ultimate strength, A_g is fracture strain, $r_{2\text{-}20/Ag}$ is the anisotropy of the material between 2 to 20 % of strain. The normal anisotropy (r_n) defines as (r_0+2r_{90}+ r_{45})/4, and planer anisotropy (Δr) defines as (r_0-2r_{90}+ r_{45})/2. Since the anisotropy of the tool sheet is insignificant (Table 4.3), the tool sheets are cut during

the laser cutting in different directions. In the strength analysis the minimum yield strength of the sheet is considered.

4.1.4 In-plan torsion test

The in-plane torsion test generally offers higher degrees of deformation than the tensile test; yield curves can be determined for a larger range (Yin et al., 2015). The torsion samples with groove geometries are used for the in-plane torsion test of blanks. The comprehensive test procedure is explained by Yin et al. (2015). The grooved specimens for the materials with a sheet thickness of 1 mm have a groove radius $r_{Nut} = 4$ mm, a groove depth $t_{Nut} = 0.5$ mm, and a groove track radius $r_{Nut} = 17$ mm. The optical measurement system used 1 s^{-1} as the frame capture frequency. The rotation motor was 100 $min^{-1,}$ and the clamping force of 100 kN. The results of each material's tensile and torsion tests are presented as follows (**Fig. 4.1**).

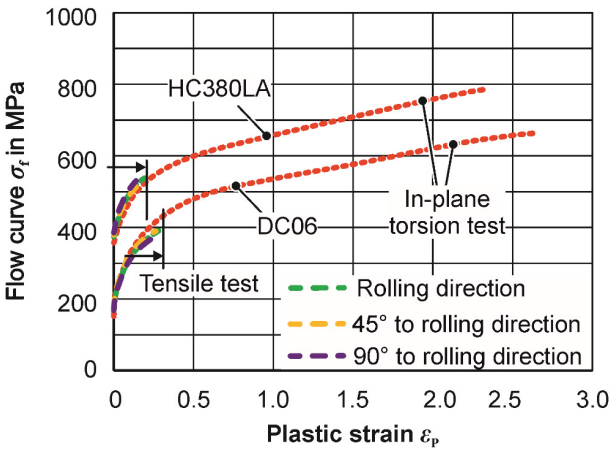

Figure 4.1: Tensile and in-plane torsion test results for sheet materials

4.1.5 Powders for LMD

Austenitic stainless steel powder 316L-Si (1.4404) and tool steel Ferro55 (comparable to X40CrMoV5-1 or 1.2344 or H13) with a delivered particle size of 45 – 125 µm (some batches 150 µm) are used as filler material for the laser metal deposition process. The chemical composition of both powders and their melting temperatures are shown in **Table 4.4**. The gas-atomized MetcoClad™ 316L-Si powder with an apparent density of 4 – 4.5 g/cm^3 is supplied by Oerlikon Metco AG. Due to the existing alloys, the deposited material offers high impact resistance, especially at elevated temperatures. Molybdenum provides high resistance to pitting and crevice corrosion. The higher

silicon content provides a cleaner deposited track as a fluxing agent. Due to its high corrosion resistance, this powder is suitable for marine, oil and gas applications (N. N., 2014). Voestalpine AG offers PLASweld™ Ferro55 powder with a density of 7.8 g/cm^3 and an average hardness of 53-58 HRC. Due to the high carbon content resulting in high hardness, only carbide tools can be used for machining. This powder is suitable for tooling concepts.

Table 4.4: Chemical composition in weight percentage % and melting temperatures of the powders

Powder	C	Ni	Cr	Mo	Si	Mn	Fe	Melting temperature
316L-Si	0.03	12	17	2.5	2.3	1.0	rest	1400 °C
Ferro55	0.35	-	7	2.2	0.3	1.1	rest	≈1570 °C

4.1.6 Laser metal deposition

The experiments for LMD are performed by a machine referenced to as Lasertec 65 3D hybrid (Lasertec 65 3D) manufactured by Sauer GmbH/DMG MORI AG. The Laserte 65 3D is a 5-axis machine in which the laser metal deposition is integrated with the milling with an automatic tool changer. The Lasertec 65 spindle can move in three linear *x*, *y*, and *z* axes, and the table rotates in two *A*-axis (around the *x*-axis) and *C*-axis (around the *z*-axis), as shown in **Fig. 4.2**.

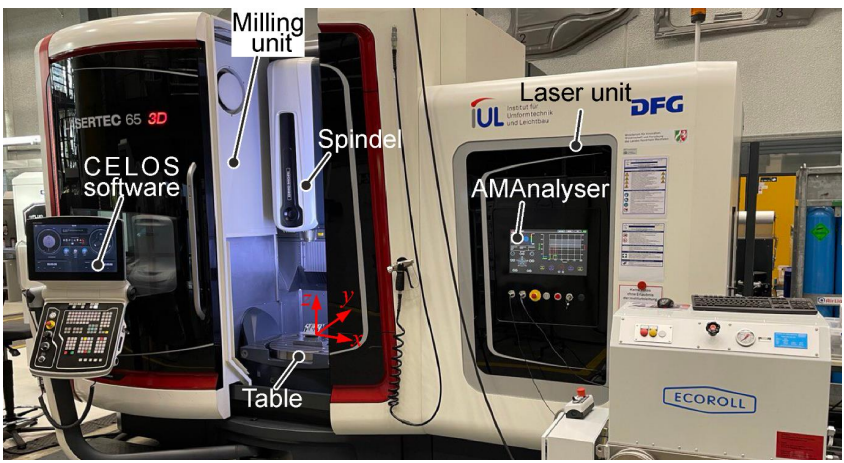

Figure 4.2: Lasertec 65 3D hybrid machine

The powder mass flow can be varied during deposition. The laser unit is manufactured by Laserline GmbH. It is equipped with a 2.5 kW fiber-coupled diode laser, which delivers the laser beam through laser fibers with a fiber diameter of 600 µm, a

wavelength of 1030 ± 10 nm, and a length of 5 m. The delivered laser light is guided by three mirrors and focused on the focal point by a focusing lens. The laser power stability is ± 2 % over two hours. Another generation of the laser head is being developed for this machine. In this study, the initial experiments are performed with the COAX09 laser head, which is later upgraded to the COAX14 head. According to the manufacturer, the main differences are better powder efficiency and improved powder focus. Both laser heads have the possibility to install two different nozzles with different laser spot diameters, namely 3 and 1.6 mm (**Fig. 4.3**).

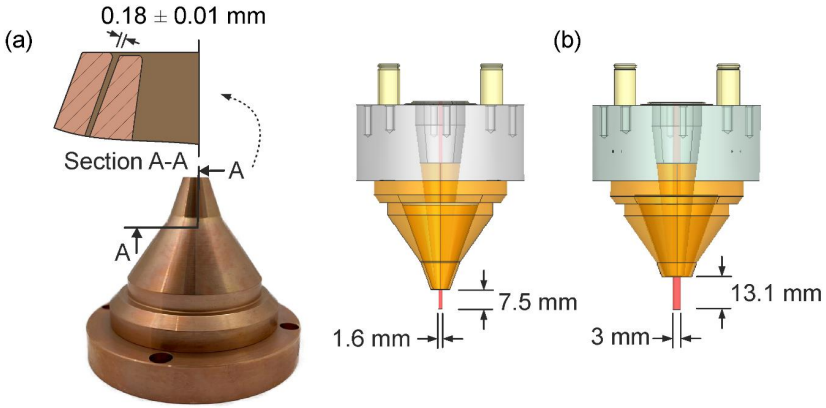

Figure 4.3: Nozzle for (a) 1.6 mm laser spot diameter, (b) 3 mm laser spot diameter

The study uses the 1.6 mm nozzle for deposition because of its small area deposition capability and low thermal distortion. For laser polishing, both nozzles are used. The powder feed gap for the 1.6 mm nozzle is about 0.18 ± 0.01 mm, while this value is about 0.36 ± 0.01 mm for the 3 mm nozzle. This results in the need to screen the supplied powder to prevent the powder from sticking and accumulating inside the 1.6 mm nozzle. All powders are sieved for the 1.6 mm nozzle in the latest laser head generation (COAX14). The sieved powder has a maximum particle size of 80 µm (min. is 45 µm). Argon gas is used as shielding and powder carrier gas. The melt pool size and temperature is measured by the camera on the laser head. Since no thermal camera is used, the temperature and melt pool size are calculated by image processing. The Fraunhofer Institute IWS Dresden developed the melt pool temperature measurement system (E-MAqS). The recorded data is directly post-processed with the AMAnalyser software from DMG MORI. The average temperature deviation is ±3 K.

4.1.7 Deep drawability and wear tests

Cylindrical cups were deep-drawn on a Schuler AG PDR 63/250 C-frame eccentric press. The maximum press capacity is 630 kN. The eccentric press is integrated into an

automated test stand. The sheet material was first fed from a coil or strip onto a coil and then fed into the die cavity by rollers, which also oil the sheets. The deep drawing oil used was Iloform PN 226 from Carl Bechem GmbH. All deep drawing tests were performed with a deep drawing speed of approximately 42 mm/s and a blank holder force of 2.4 kN. Deep drawability experiments are realized with an initial blank diameter (D_B) of 115 mm (deep drawing ratio of $\beta = 1.93$), whereas for the wear test, this value was 120 mm ($\beta \approx 2$). The punch diameter D_{Punch} was 59.9 mm (**Fig. 4.4**). The deep drawing tool geometry and specifics in detail can be found in (Kolbe, 2012). For the reference tests, a new die with a die radius of 8 mm is made out of tool steel 1.2379 (X155CrVMo12-1), which was gas nitrided to achieve the hardness of 642 ± 13 HV10 (hardness test force of 98.07 N). Wear resistance tests were conducted on all the laminated dies up to 10,000 cups using high-strength steel HC380LA. The surface roughness of the laminated dies and cups and the corner radius of the cups were measured. The measurements up to 1000 strokes were made after every 200 strokes and then after every 1000 strokes.

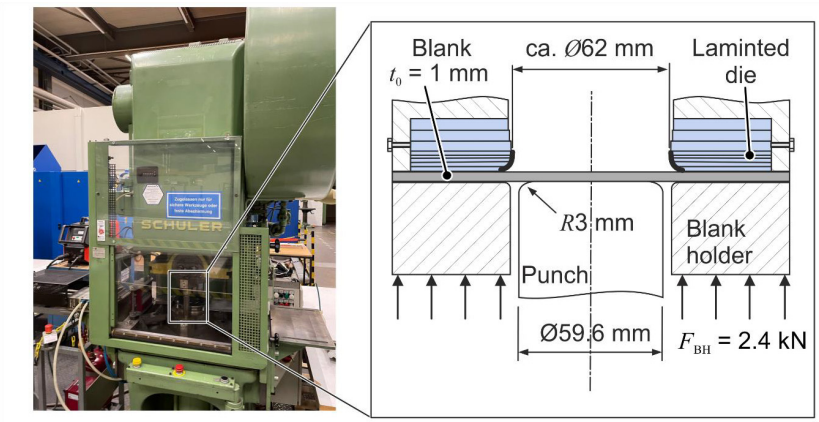

Figure 4.4: Test setup for deep drawing and wear resistance test

4.1.8 Setup for demonstrator die

A demonstrator die is manufactured using the hybrid method in order to transfer the knowledge gained to a complex shape with free surfaces. The demonstrator is deep-drawn on a single-column hydraulic drawing press HPSZK 100-1025/650 from Shuler-hydrap GmbH & Co. KG with a maximum pressing force of 1000 kN (**Fig. 4.5**). Iloform PN 226 oil is used for the deep drawing process. The experiments are performed with a blank holder force of 100 kN and a punch speed of 8.6 mm/min.

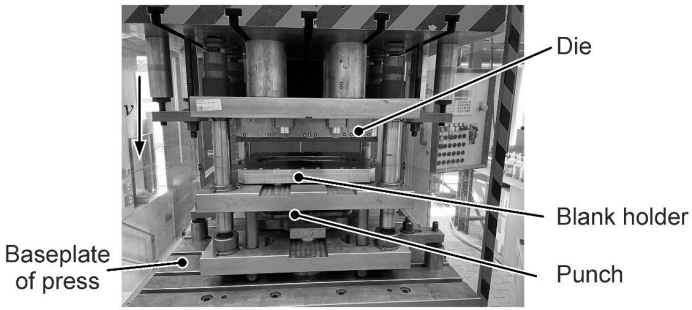

Figure 4.5: Test setup for deep drawing and wear resistance test

4.1.9 Ball burnishing

Ball burnishing experiments are performed on the DMG MORI DMU 50 CNC milling machine (**Fig. 4.6**). A hydrostatic burnishing tool with a ball diameter of 12.7 mm manufactured by ECOROLL is used. The fluid pressure used for burnishing is 30 MPa for Ferro55 and 25 MPa for 316L-Si, with a feed rate of 900 mm/min at different track distances.

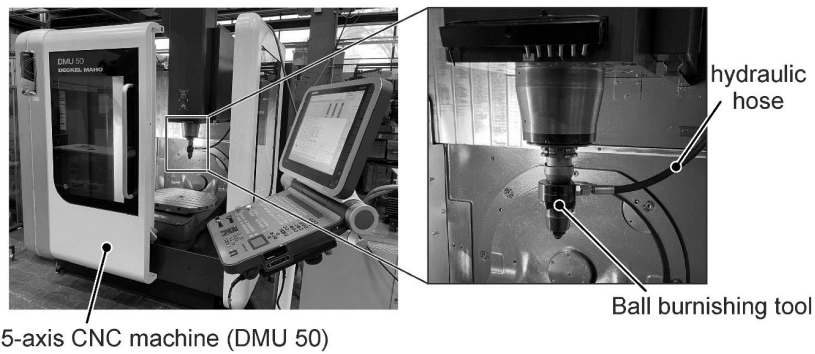

Figure 4.6: 5-axis CNC machine DMU 50 and ball burnishing tool

4.1.10 Strip tensile test

The strip tensile testing machine manufactured at IUL is used to determine the friction values (**Fig. 4.7**). Sheet strips are clamped between friction elements. Next, with the help of the hydraulic cylinder, a defined pressure is applied to the strip sheet. The applied normal force F_{normal} is adjusted based on the effective contact area to achieve a contact pressure. Then, the pulling cylinder pulls the sheet at the specified speed with the pulling force F_{draw}.

The friction coefficient μ based on Coulomb's law calculated as $\mu = \frac{F_{normal}}{F_{draw}}$. An innovative fixture is manufactured to clamp the laminated sheets on the machine (Fig. 4.7).

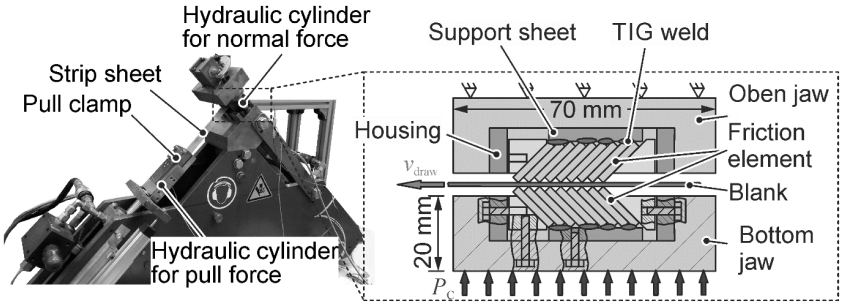

Figure 4.7: (a) Test setup for strip tensile test, (b) different friction elements

4.2 Measurements

4.2.1 Optical surface roughness measurement

The Nanofocus µsurf C confocal white light microscope is used to measure the surface roughness of laminates for preheating experiments. The measurements were performed with a 20x objective magnification. For the rest of the surface roughness measurements, the Keyence VR-5000 Series 3D Image is used. This measuring device magnifies up to 160x. It uses a 4 megapixel monochrome CMOS image receiver element and a double telecentric transmitter and receiver lens. Telecentric lenses provide constant magnification regardless of the distance or position of the object in the field of view. The instrument performs all measurements based on the ISO 21920 (2021), the new DIN ISO 4287 standard (2010) version. A 40x magnification is used for all surface roughness measurements. Surface roughness is measured in both radial and longitudinal directions in 2D and 3D.

4.2.2 Metallography and hardness measurement

The grinding and polishing processes succeed with the TEGRAMIN-25 machine. Hot mounting is carried out in the Citopress-15 mounting press, in which the specimen is surrounded with plastic granules that melt in the unit at 180 °C and solidify after subsequent cooling. The samples are final-polished with 1 µm diamond suspension. The etching is realized by immersing the surface of the samples for a few seconds in Nital, a mixture of a small amount of concentrated nitric acid and ethanol, which is suitable for etching low-alloy steel. The geometries of deposited materials were measured by a ZEISS AXIO IMAGER M1m reflected light microscope with a magnification of 50x.

Wolpert Diatestor 2 RC/S hardness machine is used for macro Vickers hardness measurement, and microhardness measurements are performed in DUH-211S from company Shimadzu Europa GmbH.

4.2.3 Residual stress measurement

The G2R model machine from Stresstech GmbH with an X-ray source of a Cr-tube with a collimator diameter of 2 mm is used for residual stress measurements. The measurement parameters are selected from Ren et al. (2019). An angle of 152.3° for 2θ, an X-ray voltage of 30 kV, and a current of 8 mA were used. An exposure time of 20 s and a tilting angle of 42° with 42° and ± 3° tilt oscillation in 8 different angles (± 19.5°, ± 28.2°, ± 35.4°, ± 42°) are used. The modified-chi measurement method is used for evaluation.

5 Tool design procedures

For the design of laminated tools, the material, the thickness, and the sequence of the individual sheets are of particular interest. The principle process chain for the innovative hybrid tools is illustrated in Fig 3.1. The sheet lamination gives the possibility of a combination of diverse sheet thicknesses and materials. There are many possibilities for sheet combinations to generate different radii. Since the calculation of the possible combinations cannot be computed manually, a Matlab code is created for the calculations. For example, for manufacturing a tool radius of 6 mm out of three different sheet thicknesses: 0.5, 1.0, and 2.0 mm, there are 520 possible combinations, and each combination has its stair-step areas (volumes). Therefore, the selection of the proper combination between the possibilities is essential. The different order of the sheet thicknesses also leads to a diversity of the stair areas. Depending on the sheet thickness, the stair areas vary considerably (**Fig. 5.1**). Varying the step area, in turn, affects the number of weld tracks and the required energy consumption and processing time in the LMD.

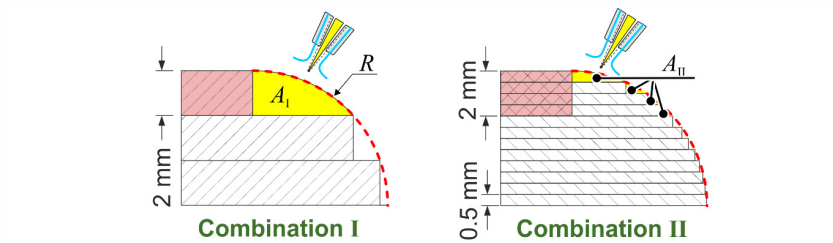

Figure 5.1: Stair-step area variation for two different sheet combinations

The selection of the appropriate process parameters for laser metal deposition (LMD) on thin sheets could avoid errors such as weak bonding strength, poor surface roughness, and high shape or form deviation (**Fig. 5.2a**).

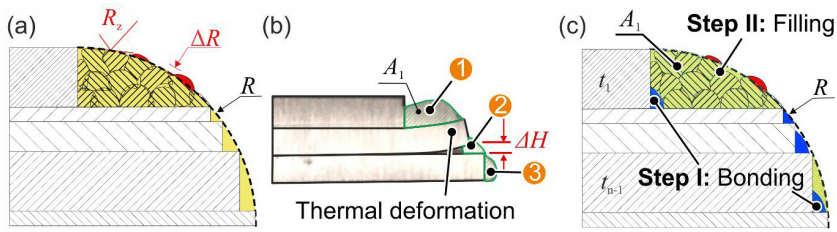

Figure 5.2: (a) Poor surface roughness and form deviation, (b) one-step filling, (c) two-step filling

High heat energy applies during the filling of stair-step areas on thin substrate sheets. From the preliminary experiments, it is concluded that the order of welding is important due to the high temperature and thin sheets. For a case in point, it was tried to fill the stir step area of A_1 as shown in **Fig. 5.2b** and then fill the areas A_2 and A_3 respectively, but as shown, filling the A_1 leads to thermal deformation of the substrate sheet. This thermal deformation is due to the applied high energy during the deposition and, consequently, thermal deformation, which leads to the form deviation in tool radius later. Therefore, in this thesis, all the laminated parts are manufactured using the two-step strategy, as illustrated in **Fig. 5.2c**. In the two-step strategy, the laminae are joined together to avoid relative movement to each other, followed by the filling strategy. The selection of appropriate process parameters for laser metal deposition will be discussed.

5.1 Properties of single/multi-deposited tracks

To specify the required deposition powder and, hence, the number of weld tracks, it is essential to establish the exact volume of the stair step area. Each stair-step area is a sector of which the opposite is the sheet thickness (t), and the adjacent is b (**Fig. 5.3a**).

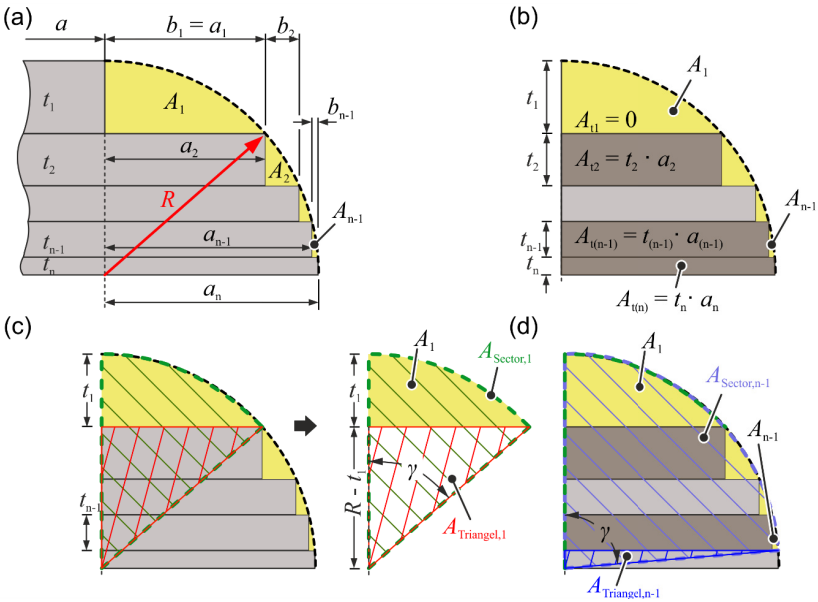

Figure 5.3: (a) Cross-section of possible sheet combination and corresponding geometries, (b) different areas, (c) section for calculation of A_1, (d) section for calculation of A_{n-1}

For the calculation of each step stair area (A_i), it is required to determine the lengths a and b as a function of radius and sheet thickness. As a first step, it is necessary to calculate the length a_i of the sheets. Based on the Pythagorean theorem, as shown in Fig. 5.3a, the radius R is a hypotenuse. Therefore, the length a_i can be calculated as:

$$a_{\mathrm{i}} = \sqrt{R^2 - \left(R - \sum_{j=1}^{i-1} t_{\mathrm{j}}\right)^2} \Leftrightarrow a_{\mathrm{i+1}} = \sqrt{R^2 - \left(R - \sum_{j=1}^{i} t_{\mathrm{j}}\right)^2}. \tag{5.1}$$

The length of b is:

$$b_{\mathrm{i}} = a_{\mathrm{i+1}} - a_{\mathrm{i}}. \tag{5.2}$$

Replacing the **Eq. (5.1)** in **(5.2)** yields:

$$b_{\mathrm{i}} = \sqrt{R^2 - \left(R - \sum_{j=1}^{i} t_{\mathrm{j}}\right)^2} - \sqrt{R^2 - \left(R - \sum_{j=1}^{i-1} t_{j}\right)^2}. \tag{5.3}$$

Each sheet has the area of A_{ti} as shown in **Fig. 5.3b**, which can be calculated as:

$$\mathrm{A}_{ti} = t_i \cdot b_i \tag{5.4}$$

For the calculation of each step, stair area A_i is essential to calculate the sector area ($A_{\mathrm{Sector,i}}$) and subtract the triangle area ($A_{\mathrm{Triangle,i}}$) and all previous step areas. As an example, shown in **Fig. 5.3c** to calculate the step stair area A_i. The sector area ($A_{\mathrm{Sector,i}}$) can be calculated as:

$$A_{\mathrm{Sector},i} = \frac{\pi}{360\,^\circ} \cdot \alpha \cdot R^2, \tag{5.5}$$

where γ is equal to:

$$\gamma_{\mathrm{Sector},i} = \cos^{-1}\left(\frac{R - \sum_{j=1}^{i} t_{\mathrm{j}}}{R}\right). \tag{5.6}$$

By replacing **Eq. (5.5)** in **Eq. (5.6)**, the segment area can be calculated as a function of sheet thickness and radius as **Eq. (5.7)**.

$$A_{\mathrm{Sector},i} = \frac{\pi}{360\,^\circ} \cdot R^2 \cdot \cos^{-1}\left(\frac{R - \sum_{j=1}^{i} t_{\mathrm{j}}}{R}\right). \tag{5.7}$$

The triangle area ($A_{\mathrm{Triangle,i}}$) can be calculated as

$$A_{\mathrm{Triangle},i} = \frac{a_{i+1}}{2} \cdot \left(R - \sum_{j=1}^{i} t_j\right). \tag{5.8}$$

Based on **Eq.s (5.3)**, **(5.4)**, **(5.7)**, and **(5.8)**, the area of each stair step area is equal to:

$$A_i = A_{\text{Sector},i} - A_{\text{Triangle},i} - \sum_{j=1}^{i-1} A_j - \sum_{j=1}^{i} A_{\text{t}j} \text{ or} \tag{5.9}$$

$$A_i = \frac{\pi}{360\,°} \cdot R^2 \cdot \cos^{-1}\left(\frac{R - \sum_{j=1}^{i} t_j}{R}\right) - \frac{a_{i+1}}{2} \cdot \left(R - \sum_{j=1}^{i} t_j\right) - \sum_{j=1}^{i-1} A_{\text{j}} - \sum_{j=1}^{i} t_j \cdot b_j. \tag{5.10}$$

As illustrated in **Fig. 5.4**, by choosing different sheet thicknesses as the first sheet (t_1), the stair step area (A_1) can be varied significantly based on the tool radius.

Calculating the stair step areas helps estimate the number of weld tracks during the laser deposition and the required amount of powder (chapter 7).

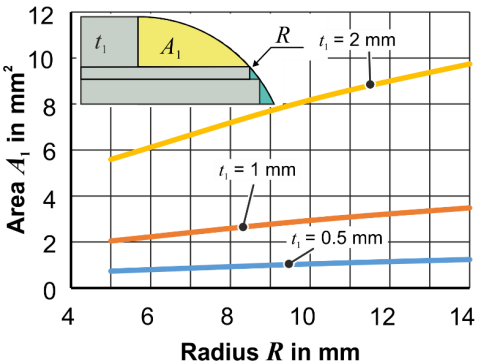

Figure 5.4: Dependency of area A_1 to the initial sheet thickness for different tool radii based on **Eq. 5.10**

5.1.1 Single weld track

The bonding weld tracks are required to join the sheets to each other to avoid the thermal distortion of thin substrate sheets during the filling step. The joining tracks need to have high strength and proper quality without any defects such as porosity, lack of fusion, discontinuous weld track, etc. For this purpose, a parameter study is performed with different laser power (P), feed rate (f), and powder mass flow ($\dot{m}$). The preliminary experiments are developed using the Design of Experiments (DOE) with Design Expert software (version 12) to generate a test plan for Ferro55 and 316L-Si powder. Based on the D-optimal method, the total experiments are reduced to 65 for each powder (in sum: 130 experiments). Each experiment is repeated at least three times. The process parameters laser power P (700, 1000, 1400, and 1800 W), feed rate f (700, 1000, and 1400 mm/min), and powder mass flow $\dot{m}$ (4, 7, and 10 g/min) are varied within the given values. The list of experiments is given in **Appendix A**. Three sheets with thicknesses

of 0.5 mm, 1.0 mm (HC420LA), and 2.0 mm (S355MC) are utilized for joining (six different sheet combinations in total). For the fillet weld track, a continuous weld track 210 mm in length is deposited, and 40 mm wide tensile specimens are laser cut from the overlapped sheets. The deposition is performed with the COAX09 laser head. The tensile experiments (**Fig. 5.5**) are served with a universal testing machine from Z250 the company ZwickRoell GmbH & Co. KG. Supporting sheets with relative thickness are used to minimize the bending moment in the weld track during the experiments. For determination of the fracture strength of the weld (σ_w) it is assumed that the tensile force flows perpendicular to the hypotenuse of the triangle of the fillet track (Fig. 5.5). The effective area A_{eff} is the hypotenuse length multiplied by the sheet's width (40 mm). By using the support sheets, it is assumed that there is no bending moment between the sheets during the tensile experiments, and the whole force flows through the weld area.

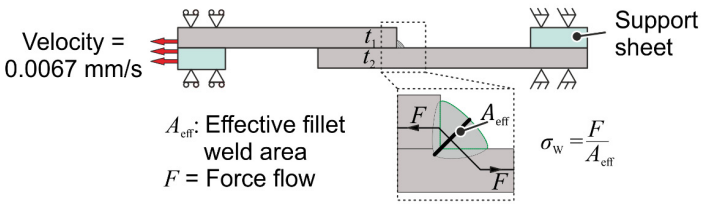

Figure 5.5: Tensile test setup for fillet weld track

The hypotenuse length of the fillet weld tracks was measured using the Zeiss Axio Imager.Z2m microscope. The cross-sectional area of the fillet weld tracks varies between 0.37 and 1.7 mm^2 depending on the deposition parameters and sheet thickness combinations used for Ferro55 powder. During the experiments, in some combinations, the tool sheets are plasticized or fractured prior to the weld fracture. Therefore, it was not possible to determine the maximum weld fracture strength for such combinations. The weld tracks are fractured by 2 mm in all experiments with 2 mm sheet combinations. The discontinuous and inhomogeneous weld tracks are caused either by the high feed rate and low laser power at low powder mass flow or by the high powder mass (**Fig. 5.6a**). The high laser power of 1400 W combined with the low powder mass flow results in melt-through of the 0.5 mm tool sheet. However, with the same feed rate and power, the depth of the melt area is less than 30 % of the substrate sheet by increasing the mass flow (**Fig. 5.6b**). In general, the shape of the weld track can be convex, flat or concave. The sheet combination is important in determining the shape of the weld track because the same process parameter creates different shapes of fillet welds (**Fig. 5.6c**). The thinner overlapped sheet in combination with high powder mass flow or high feed rate results in convex shapes.

In AM, the physical properties of weld lines depend on many process parameters and hardware (such as machine type, powder quality, grain size, and etc.).

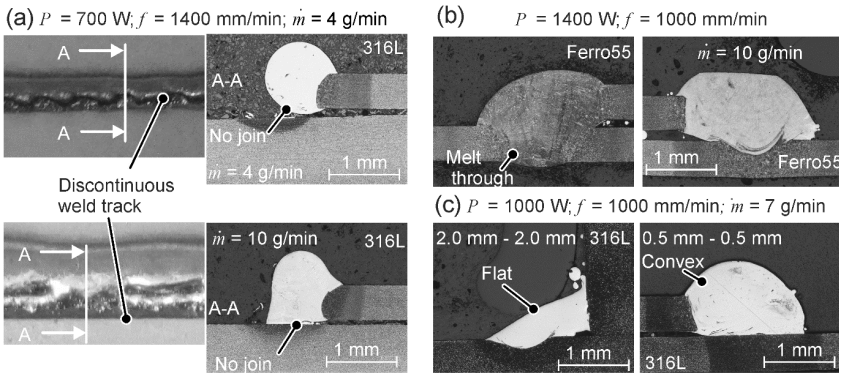

Figure 5.6: (a) High feed rate with low laser power, (b) effect of the mass flow and high laser power on weld quality, (c) effect of sheet combination on the shape of the weld track

A simple interpretation of the effect of a single process parameter is not possible; therefore, different combined parameters are defined in the literature (Bax et al., 2018). The combined parameter θ is defined as the track-specific power density or the mass per unit length of the deposited fillet track (Costa et al., 2003). It is defined as:

$$\theta = \frac{P \cdot f}{\dot{m}} \text{ or } \left[\frac{\text{Power·Distance}}{\text{Mass}}\right]. \tag{5.11}$$

The weld fracture strength (σ_w shows that the higher specific power densities θ more or less increase the weld fracture strength (**Fig. 5.7**).

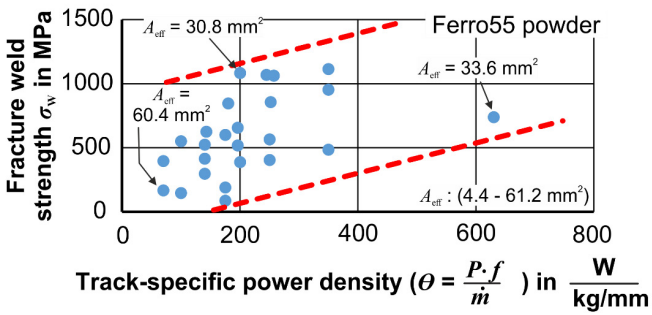

Figure 5.7: Track-specific power density effect on the fracture weld strength (σ_w) for Ferro55 powder

This can be achieved by increasing the laser power and/or feed rate or decreasing the powder mass flow. Since there is a significant scatter in the weld fracture strength, a second group of full factorial bonding experiments (total 60 combinations

× 3 replicates = 180 tests) are performed. The experiments were conducted with only 2 mm to 2 mm sheet combinations. The process parameters for the second set of experiments for the fillet weld study are shown in **Table 5.1**. The tensile tests are performed as shown in Fig. 5.5.

Table 5.1: LMD process parameters for fillet weld track

Levels	**I**	**II**	**III**	**IV**	**V**
Laser power P (W)	600	800	1000	1200	1400
Feed rate f (mm/min)	600	800	1000	1200	-
Powder mass flow $\dot{m}$ (g/min)	4	7	10	-	-

Five weld tracks of 30 mm length were deposited with five different laser powers (**Fig. 5.8a**). The geometry of the tensile specimen is shown in **Fig. 5.8b**. The deposition was performed with a new laser head (COAX14). Both 316L-Si and Ferro55 powders were tested. Five tensile specimens were lasered from each series of depositions (Fig. 5.8a).

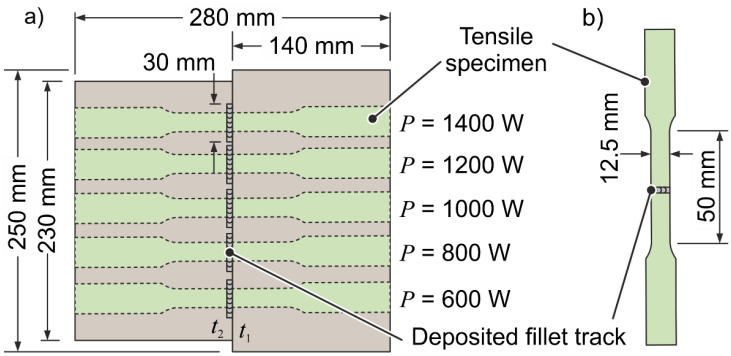

Figure 5.8: (a) Deposition step up and laser cut of tensile specimen, (b) dimension of tensile specimen

The tensile results show that the laser power 600 and 800 W, in most cases, deliver not proper joining (σ_w = 0), i.e., no bonding. Each parameter is studied individually to determine the effect of each process parameter on the weld strength (**Fig. 5.9a** and **b**). The laser power above 1000 W delivers the correct weld tracks independent of the mass flow or feed rate in the given range studied. However, the amount of fracture strength is dependent on the feed rate and mass flow. The maximum weld strength is achieved at 1000 and 1200 mm/min feed rates. The powder with a mass flow of 4 g/min delivers higher weld strength followed by 7 and 10 g/min. The possible reason is that the amount of the applied energy can fully melt the applied powder and generate a high dilution

ratio (Ø) as shown in **Fig. 5.10a**. The low energy results in insufficient powder melting and poor weld path deposition (**Fig. 5.10b**).

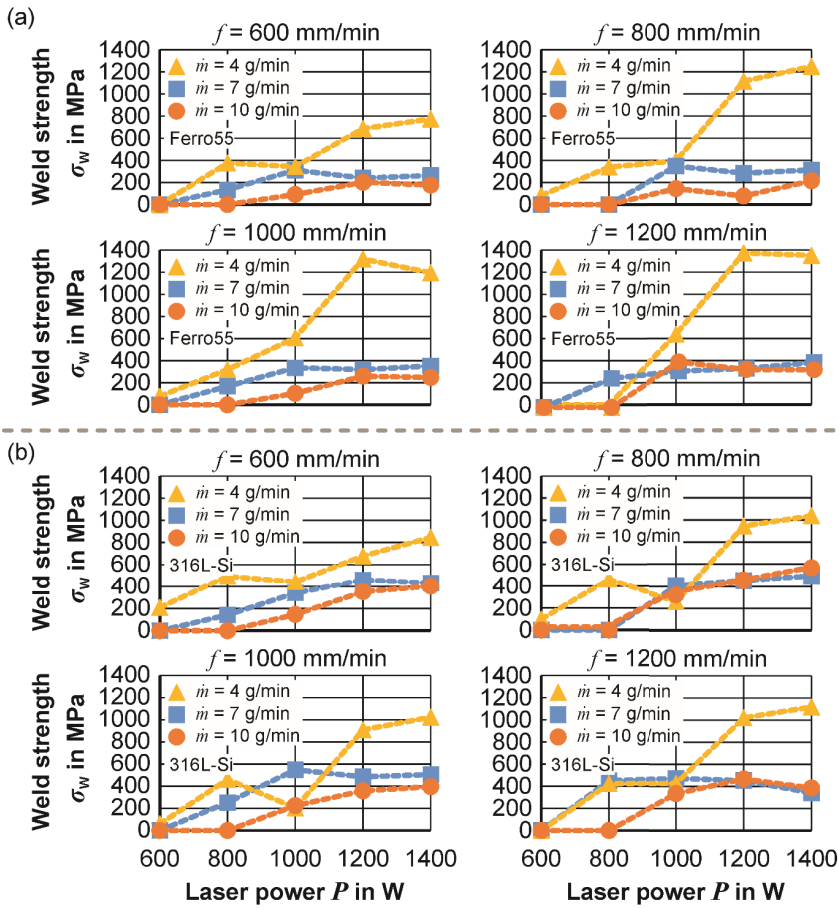

Figure 5.9: Weld strength of fillet track as a function of laser power and different feed rates and powder mass flows for (a) Ferro55, (b) 316L-Si powder

In sheet lamination, a higher number of sheets requires more bonding tracks, which increases the number of thermal cycles. Different combinations of sheets (with different numbers of sheets) were deposited, and the hardness of the initial fillet track was measured to investigate the effect of the number of thermal cycles on the hardness of the bonding tracks (**Fig. 5.11a**).

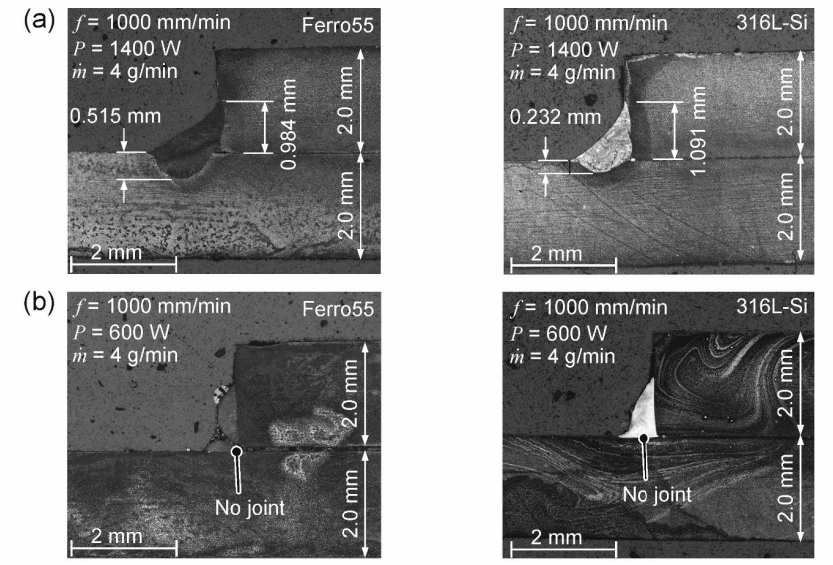

Figure 5.10: (a) High dilution ratio, high weld strength, (b) zero dilution ratio, no joint

The high sheet numbers with constant sheet thickness decrease the hardness of the weld track for Ferro55 by a maximum of 40 % (**Fig. 5.11b** and **c**). This reduction can be explained by the fact that the distance between the weld tracks decreases with a higher number of layers with constant radius, i.e. thinner thicknesses. Thus, the individual weld tracks are exposed to a higher number of thermal cycles over a longer period of time. 316L-Si powder has a lower hardness variation (max. 20 %), and due to the higher number of weld tracks, the hardness is almost constant for the same and different sheet thicknesses. This can be attributed to the fact that 316L-Si has almost the same material properties as substrate sheets; therefore, the thermal conductivity is almost the same. Thus, the energy converted into heat is transferred from the substrate sheet with each new deposition.

Fillet weld tracks have two sides or edges in contact with the weld track, the horizontal substrate and the vertical. The vertical side is a function of the sheet thickness, and the contact area can define the amount of heat transfer from the weld track to the substrate sheet in the horizontal direction. Due to the larger contact area, the sheet with a thickness of 2 mm as an initial sheet (t_1 = 2 mm) increases the cooling rate, and therefore, the hardness is higher compared to the thinner sheet with a thickness of 0.5 mm (**Fig. 5.11d**). The hardness of 316L-Si shows no sensitivity to initial sheet thickness.

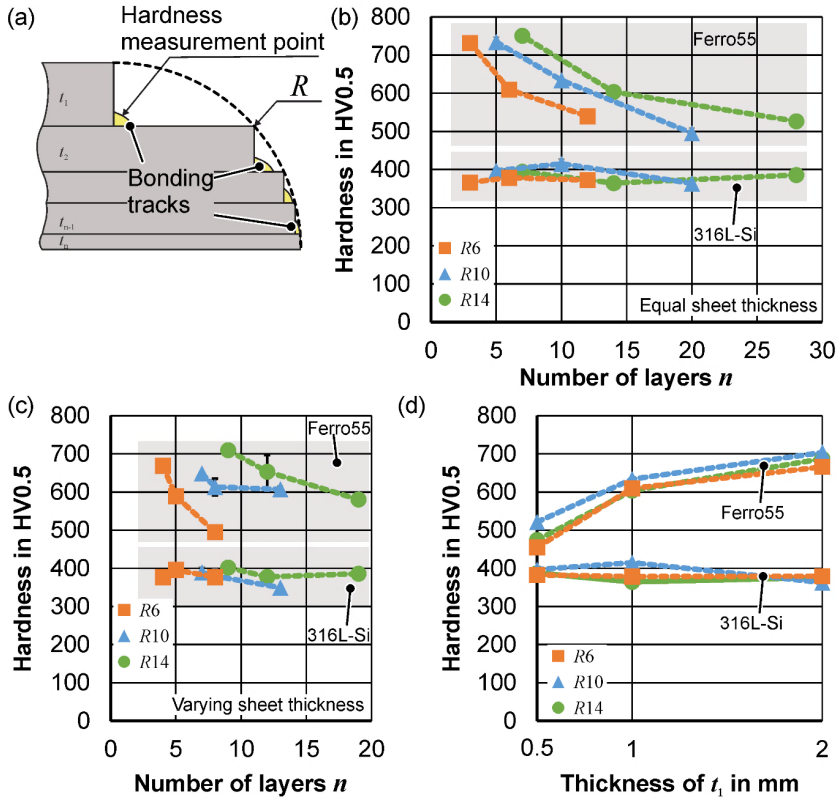

Figure 5.11: Effect of the number of layers on the hardness of the first bonding weld track (a) measured point, (b) same thickness, (c) varying sheet thickness, (d) initial sheet thickness

5.1.2 Multi-weld tracks

The selection of the proper process parameters during the deposition decreases the amount of post-processing required, especially for ball burnishing and laser polishing. Oversizing, high surface roughness, and undersizing are common errors in the filling step. Laser power, powder mass flow, and feed rate are varied for Ferro55 and 316L-Si powders to investigate the effect on surface roughness and form accuracy. A flat surface is considered for deposition. A biaxial strategy is used for deposition on a flat surface. The deposition process parameters are varied based on **Table 5.2**.

Table 5.2: LMD Process parameters for deposition on the flat surface

Process parameters	Level		
	I	II	III
Power *P* (W)	800	1000	1200
Feed rate *f* (mm/min)	600	800	1000
Powder mass flow $\dot{m}$ (g/min)	4	6	8

A single layer is deposited on a square with dimensions of 31.4 × 31.4 mm^2 (**Fig. 5.12**). A track spacing of 1.2 mm (25 % toolpath overlap) and a laser beam diameter of 1.6 mm are used for deposition. During deposition, the melt pool size and temperature were recorded. After each deposition, the laser nozzle was purged with argon gas to ensure that no powder particles were stuck in the nozzle orifice to avoid possible effects on the surface roughness results and increase the nozzle's lifetime. All powders were sieved to a maximum grain size of 80 µm (minimum grain size 45 µm). Full factorial design experiments are performed, i.e. 3^3 = 27, and repeated twice. The experiments are performed with the COAX14 laser head.

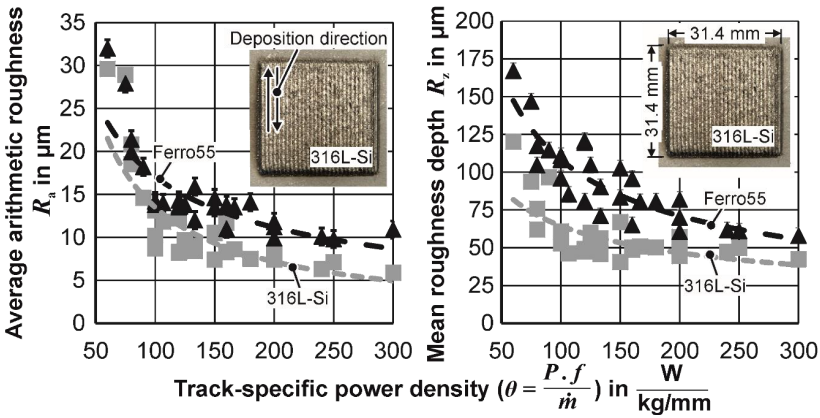

Figure 5.12: Effect of LMD parameter on surface roughness on the flat surface

The higher track-specific power density (θ) results in better surface roughness. The surface roughness parameter in both 2D and 3D decreases as the laser powder or feed rate increases or the powder mass flow decreases (Fig. 5.12). For the same amount of θ, the R_a values for Ferro55 powder are higher than for 316L-Si. The same trend can be seen for the S_a values; however, the values are higher because the measurements were made in 3D, which captures more surface defects. The higher surface roughness can be explained by the difference in the melting points of the two powders, since the Ferro55 powder has a higher melting temperature than 316L-Si (**Table 4.4**). Therefore, for the constant track-specific power density, the number of unmelted particles are higher in Ferro55 powder.

The higher laser power leads to a better surface roughness for 316L-Si powder. Increasing the laser power from 800 W to 1200 W decreases the R_a value by 25 % (**Fig. 5.13**). However, after 1000 W, the R_a is raised slightly for Ferro55 powder. Higher powder mass flow leads to higher surface roughness for both powders, up to 42% for R_a (Fig. 5.13). At lower powder mass flow rates, more powder volume can be efficiently and completely melted. Higher powder mass flow rates at the same laser power and feed rate result in some powder particles not completely melted. Increasing the feed rate from 600 to 800 mm/min improves the surface roughness by more than 50 % (Fig. 5.13). Increasing the feed rate from 800 mm/min to 1000 mm/min has no significant effect on surface roughness. It can be concluded that the lower powder mass flow and higher laser power and feed rate lead to better surface roughness for flat areas.

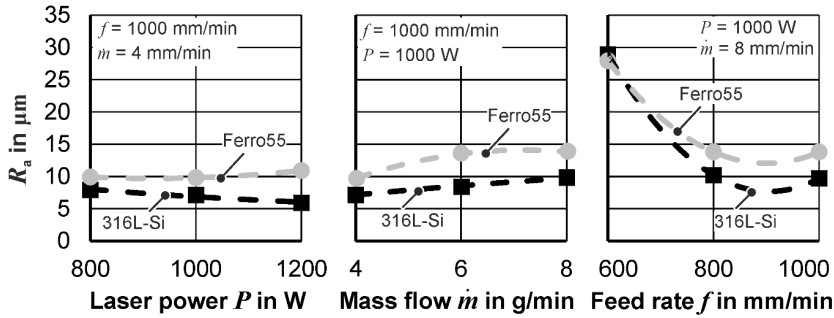

Figure 5.13: Effect of LMD process parameter on surface roughness on a flat surface

The effect of different strategies for cutting the tool sheets and filling strategy in the filling step is studied. Two approaches for the cutting tool sheets are investigated. The tool sheets are cut based on the nominal radius in the first approach. In this approach, called without offset, the corner of the tool sheets is in contact with the nominal radius (**Fig. 5.14a**). The main disadvantage of this approach is the inhomogeneous surface. Because some stair-step areas are so small, applying the fill and bond steps is impossible. Applying the bonding tracks on small stair-step areas leads to inhomogeneity, high form deviation, and high surface roughness (**Fig. 5.14b**). The solution is to use the second approach, "with offset strategy". In this strategy, all of the tool sheets (except top and bottom) are cut shorter, i.e., the radius is offset by minus b_S (here b_S = 1 mm) to the nominal die radius R (Fig. 14b). In the "with offset strategy" there the filling steps are divided into two levels (**Fig. 5.14c**). In the first level, called the prefilling step, the remaining areas from the bonding step to the offset radius (R - b_S) are filled to prepare an almost homogeneous base for the application of the fill layers. Finally, the final fill layers are applied according to the thickness of the layer.

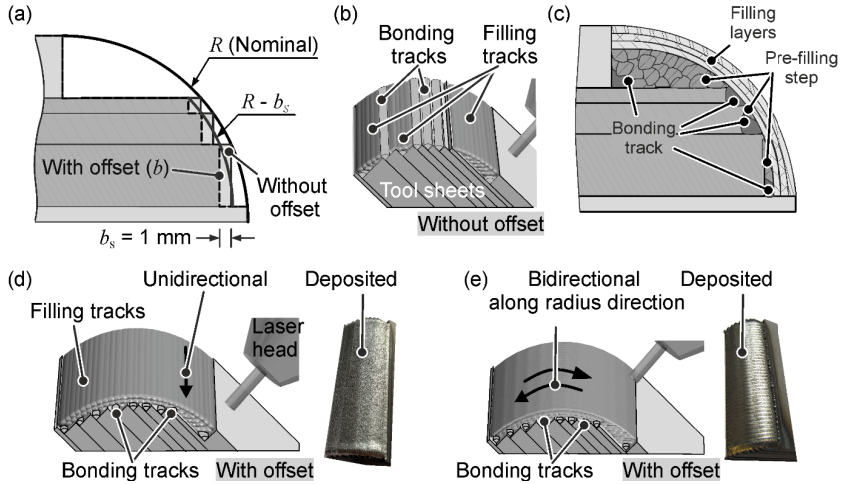

Figure 5.14: (a) Sheet cutting strategy, (b) without offset strategy, (c) with offset strategy, (d) unidirectional with offset strategy, (e) bidirectional in radius direction with offset

The "with offset strategy" can be followed by two diverse deposition methods. In the unidirectional method (**Fig. 5.14d**), all weld tracks are in the same direction as the bonding tracks. In the second method, the filling layers are along the radial direction (**Fig. 5.14e**). This strategy is called "radial bidirectional smoothing step". With offset strategy generally provides a more uniform surface with a proper surface roughness. Since the final weld tracks are along the nominal radius, it has a lower shape inaccuracy than "with offset strategy with unidirectional method". By the same process parameters during the deposition, the surface roughness (R_a in radius direction) of bidirectional along the radius direction is 35 % better than unidirectional with the offset strategy. Yet, the deposition time is almost three times longer, and the nozzle lifetime is shorter.

5.2 Preheating of substrate sheets

The distracting residual stresses are the main undesirable properties of the manufactured part in most additive manufacturing processes. The residual stresses can be reduced by preheating the substrate in AM parts (Li et al., 2018). Since preheating can affect the mechanical properties of the deposited region, the following section systematically analyzes this effect on the surface roughness characteristics, hardness, and residual stresses of the deposited areas. To investigate the effect of preheating on the forming process, bending dies are fabricated, and bending experiments are conducted.

The deposition is done based on a two-step strategy. A weld track distance of 0.56 mm with a unidirectional strategy is used during the filling step. The process parameters for

LMD in the bonding step were: laser power $P = 1400$ W, powder mass flow $\dot{m} = 7$ g/min, and a feed rate of $f = 1000$ mm/min. For the ensuing filling step the following parameters are used: $P = 1000$ W, $\dot{m} = 4$ g/min, and $f = 1400$ mm/min. Two stair step areas are assigned as A_1 and A_2 as shown in **Fig. 5.15a**. The 2 mm thick tool plates are heated by two heating cartridges (**Fig. 5.15b**). A 1 mm sheet of shielding steel (cover sheet) is used to ensure uniform heat distribution to all tool sheets (see **Fig. 5.15c**). In addition to the room temperature (RT), the temperature of the tool sheets is increased to 100 °C, 200 °C and 300 °C. A total of 12 experiments are performed with two replicates for each temperature. A thermometer is used to monitor the temperature during the heating of the tool sheets (**Fig. 5.15d**). The temperature increase is stopped just before the start of the deposition for technical and safety reasons. The melt pool size and temperature are monitored and reported by a camera embedded in the laser head above the deposition.

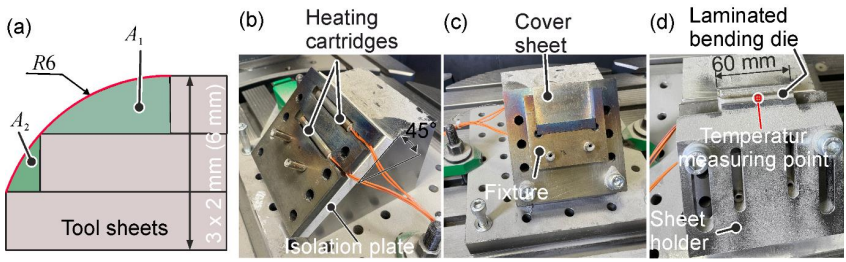

Figure 5.15: (a) Bonding and filling areas, (b) setup for preheating, (c) laminated bending die fixture, (d) deposited laminated bending die

5.2.1 Preheating effect on surface roughness

The surface quality of the forming tool directly affects the surface roughness of the deformed workpiece. Therefore, the effect of preheating on the surface roughness quality of the formed region is investigated. **Fig. 5.16a** shows the 2D surface roughness parameters measured along the radius direction. The effect of the preheating temperature on the R_a values is negligible, but the R_z value (mean roughness depth) decreases by about 30 % at the preheating temperature of 300 °C. In the areal surface parameters (3D), S_a and S_q increase by 31 % and 77 %, respectively (**Fig. 5.16b**). As in 2D, S_z decreases as the preheat temperature increases. A slow cooling rate and a longer semi-solid state in the melt pool lead to the formation of fewer peaks on the deposition surface by evaluating the preheating temperature. Due to the long solidification time, the waviness of the surface increases, as shown in **Fig. 5.16c**. All the waviness parameters (W_a, W_p, and W_q) of the deposited surface increase by at least 100 % by elevating the

preheating temperature. The course of the core surface roughness of the bearing area (S_k) at different preheating temperatures is presented in **Fig. 5.16d**.

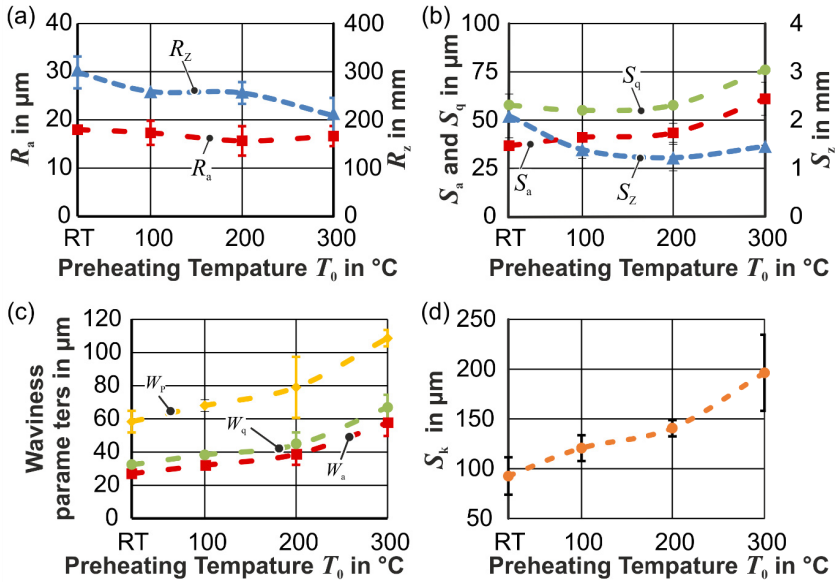

Figure 5.16: Preheating temperature effect on (a) 2D direction the field roughness parameters R_a and R_z, (b) 3D surface S_a, S_z and S_q, (c) waviness parameters W_a, W_p and W_q, (d) core height S_k

The core surface roughness of the bearing area after the primary operating cycle (such as bending experiments) is represented by S_k. Higher preheating temperatures increase the S_k depth, resulting in a rougher surface and higher friction forces after the primary operating cycle. The higher frictional forces also mean an increase in process forces during the experiments. The decrease in the mean roughness depth (R_z and S_z) can be explained by the deposited surface's mean profile height (h_m) of the deposited surface along the tool radius, as illustrated in **Fig. 5.17**.

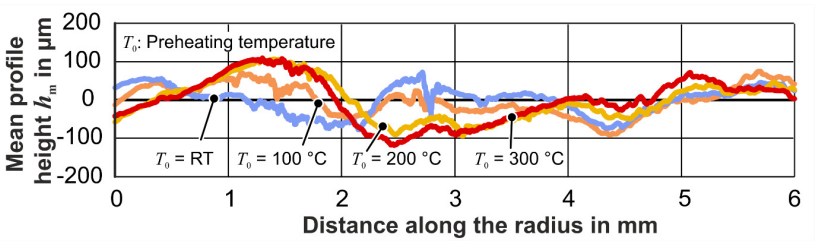

Figure 5.17: Mean profile height (h_m) at all preheating temperatures

For evaluation, the length of 6 mm of the profile length is cut in the same way for all cases. The mean profile height (h_m) results at different preheating temperatures show that the height of the wave domains increases as the preheating temperature increases. The mean profile heights (h_m) at higher preheating temperatures are smoother and show lower sharp picks but with a longer length and greater wave domain than those at lower temperatures. The sharp small peaks are formed due to the high cooling rate and incompletely melted particles.

5.2.2 Influence of preheating on residual stress

Almost all manufacturing processes induce residual stresses of various magnitudes, which play a key role in the service life of specimens. The compressive residual stresses in metal forming tools are mainly preferred because they stop crack growth and extend the fatigue life of specimens (Milella, 2013). The unique thermal cycles in AM (especially metal) are due to the rapid heating, cooling, and remelting with simultaneous melting of the previously solidified deposited layer. Such a high number of thermal cycles leads to sharp gradients of compressive or tensile residual stresses. The resulting residual stresses cause local failures in the manufactured AM parts (Li et al., 2018). After deposition, the residual stresses are measured once along the weld track ($\sigma_{0°}$) and once perpendicular to the weld track ($\sigma_{90°}$). The measurements are conducted in both the deposited area and heat-affected zone (HAZ), as shown in **Fig. 5.18a**. The residual stress at each preheating temperature is measured for three specimens and the standard deviation is calculated. The residual stresses $\sigma_{90°}$ (perpendicular to the weld tracks) in the deposited area are all tensile stresses (positive), as illustrated in Fig. 5.18a. The residual stresses parallel to the weld track ($\sigma_{0°}$) at RT and preheating temperature of 300 °C are insignificant, however, these values at 100 °C and 200 °C are positive yet smaller than the residual stresses at 90°. It can be seen that the tensile residual stress at 100 °C is reduced by a maximum of 25 % in comparison to RT in $\sigma_{90°}$. The tensile strength and ultimate strength of the DED manufactured tensile samples out of 316L-Si material are 486 MPa and 676 MPa, accordingly (Kumaran and Senthilkumar, 2021).

The tensile residual stresses in $\sigma_{90°}^{\text{Deposited}}$ could be clarified by rapid and short thermal cycles of heating and cooling. In the heating phase, the energy source (laser) increases the temperature of both the powder (filling material) and the substrate to the melting temperature, which causes an expansion in the molten material. However, this expansion is restricted by the substrate sheet or deposited material beside the heated zone. It results in the creation of compressive stresses. The cooling phase begins instantly after removing the energy source, which leads to cooling down the heated zone and the deposited material, and the material begins to shrink. By deposition of the next layer, the plastic deformation increases due to the heating phase and the reduction of the shrinkage. Finally, by resolidification, the deposited material begins to shrink again, but the solidified deposited material in the previous layer partially retrains this shrinkage,

resulting in tensile stress (Li et al., 2018). The residual stress at RT is nearly zero in both directions in the HAZ, as shown in **Fig. 5.18b**.

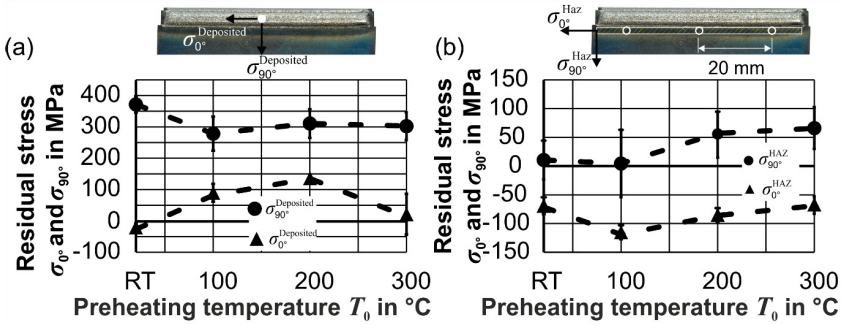

Figure 5.18: Effect of preheating temperature on residual stress in (a) deposited area, (b) heat affected zone (HAZ)

At 100 °C, the compression residual stresses rise slightly in the 90° direction ($\sigma_{90°}^{Haz}$); however, they increase in the negative direction for almost 100 % parallel to the weld track ($\sigma_{0°}^{Haz}$). Nevertheless, the residual stresses in HAZ are comparatively small and insignificant in both directions. The reason for low residual stresses is low thermal cycling and a free length at the beginning and finishing points of the weld tracks on both sides. This allows for thermal expansion, resulting in low residual stresses.

5.2.3 Influence of preheating on form accuracy

The shape and form accuracy of the tool has a direct effect on the geometry of the formed parts. In conventional manufacturing processes such as milling or turning, the precise movement of the cutting tool during the material removal process results in high geometric accuracy. Due to the solidification of the liquid state, it is impossible to control each track geometry in AM; therefore, the form and shape accuracy of most AM processes, especially DED, is low. The geometries of the deposited tracks define the shape and form accuracy of the manufactured parts in DED or especially in LMD processes. Two parameters, heat transfer, and solidification, are the main physical phenomena that influence the dimension and geometry of the deposited tracks. The metallographic images for all bending dies at four preheat temperatures (**Fig. 5.19**) show an inaccuracy in the die radius in all the laminated dies produced at the different preheating temperatures. The deposited material does not completely fill the entire stair-step area at RT. Increasing the preheat temperature reduces this problem, although even at 300 °C, there is still an excess of deposited material in the stair-step area, and the radius is oversized. To explain the reason for this phenomenon, it is essential to study the size of the melt pool.

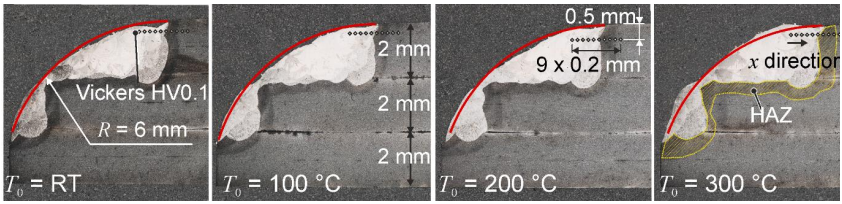

Figure 5.19: Cross-section of dies produced at four preheat temperatures

The influence of the preheating temperature on the melt pool size is significant and increases as the preheating temperature increases. As shown in **Fig. 5.20a**, each region has its corresponding deposition and filling steps. The deposition areas are designated A_{B1}, A_{F1}, A_{B2}, and A_{F2}. The variation of the melt pool size of the bonding for different preheating temperatures is presented in Fig. 5.20a. The bonding melt-pool size rises by elevating the preheating temperature by approximately 48 % and 62 % for A_{B1} and A_{B2}, accordingly. Due to the increasing temperature of the substrate (tooling sheets) during the deposition of AB1, there is a small variation in the melt pool size (**Fig. 5.20b**).

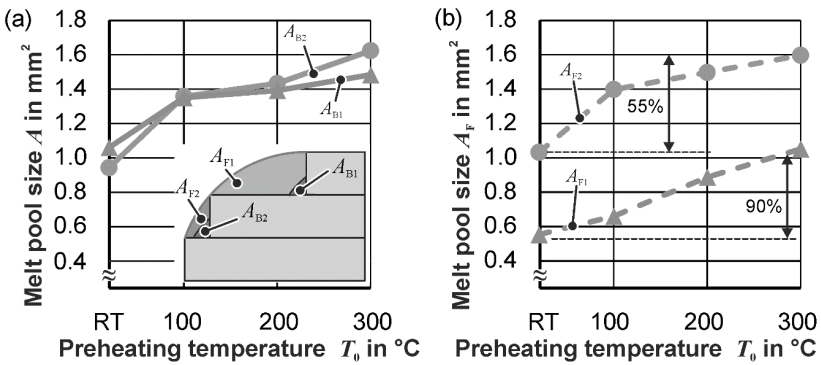

Figure 5.20: Effect of preheating on (a) melt pool size of bonding step, (b) melt pool size of filling step,

In the filling step, where the melt pool size of A_{F2} is larger than A_{F1}, the effect of secondary preheating is more significant, as shown in Fig. 5.20b. The melt pool size of filling in A_2 is almost 100 % larger than that of filling in A_1 at the same preheat temperature, i.e., $A_{F2} > A_{F1}$. The deviation of the melt pool size at RT varies from about 34 % (for A_2) to 40 % (for A_1) in the filling step. However, the maximum deviation of the melt pool size at higher temperatures is 27 %, indicating a stabilization at higher temperatures. Increasing the substrate preheating temperature increases the melt pool size in A_{F1} at T_0 = 300 °C by approximately 90 % compared to RT and by 55 % in A_{F2} (Fig. 5.20b).

The melt pool temperature (T) shows a minor deviation for all cases, and the mean value is around 1642 ± 2 °C for all temperatures. Overall, the increased preheating temperature to 300 °C has an insignificant effect on the melt pool temperature.

5.2.4 Influence of preheating on hardness

The hardness of AM parts is a function of the chemical composition of the deposited material and the substrate, in addition to the thermal cycles applied during the AM process. Since the hardening step is omitted in the hybrid additive laminated method, it is essential to study the effect of preheating on hardness. For this purpose, Vickers hardness measurements were performed starting from the deposited area to the substrate sheet. The variation of the hardness from the deposited area to the substrate sheet (along the x directions) is illustrated in **Fig. 5.21**. The hardness of the deposited area is higher than the substrate and slightly higher than the HAZ. However, the hardness of the called transition zone is much higher than the other zones.

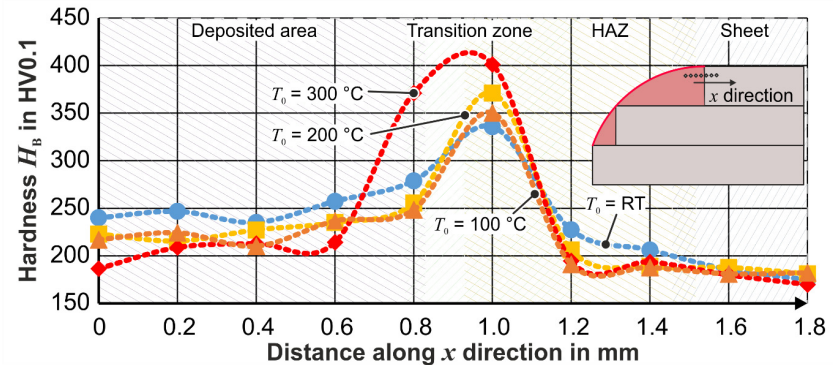

Figure 5.21: Hardness change of laminated bending dies from deposition to sheet

The hardness profile shows the same trend with studies for a single track (Ya et al., 2016) and multi-welded tracks (Hao et al., 2018). The difference in hardness compared to RT at 100 °C and 200 °C is insignificant, with the hardness decreasing by about 19 % at 300 °C. Two main reasons could explain the high hardness in the transition zone. The first reason could be the grain size since the cooling rate of the deposition zone, transition zone, or HAZ is different. Since the cooling rate in the melt pool is lower than in the transition or HAZ, the grain sizes are coarser. To verify this, electron backscatter diffraction (EBSD) is performed (**Fig. 5.22**).

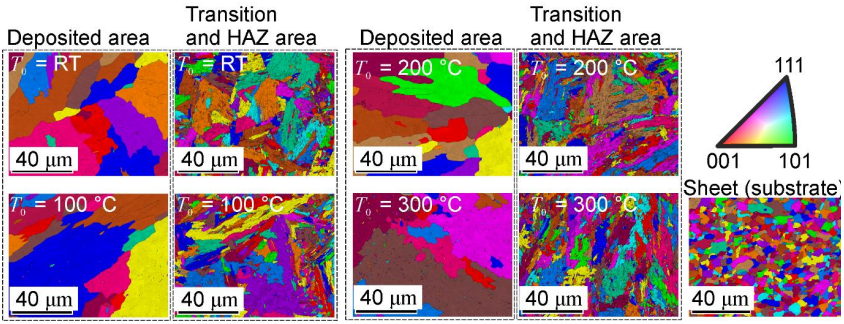

Fig. 5.22: (a) EBSD results for different preheating temperature, color coded map type: Inverse pole figure [001] crystal direction

The results shown in Fig. 5.21 confirm that the grain size of the transition zone is finer than that of the deposition zone. The average grain size in the deposition zone is 33 % coarser than in the transition zone and HAZ.

The formation of alloying elements is the transition zone, and the HAZ zone based on Ya et al. (2016) and Hao et al. (2018) may be the second reason. The energy dispersive X-ray spectroscopy (EDX) results of 316 SS powder confirm the presence of nickel and chromium alloys in these regions (Barragan De Los Rios et al., 2023).

5.2.5 Influence of preheating on bending radius

Bending experiments are conducted to understand the effect of the tool surface on bent sheets, as shown in **Fig. 5.23a**.

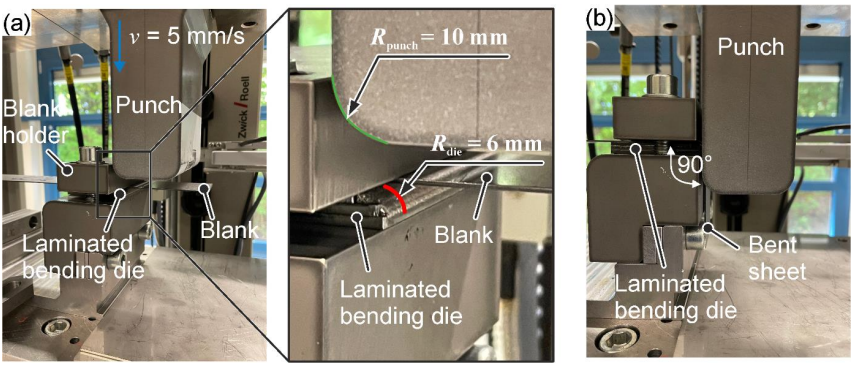

Figure 5.23: (a) Test setup for air bending, (b) bent sheet during and after bending

The two types of blanks, DC06 and HC380LA, with a thickness of 1 mm, are bent at a bending angle of 90°. One side of the blanks was fixed between the laminated bending

die and the blank holder. The blank holder force was generated by screws. A punch velocity was v_P = 5 mm/s. The clearance between the hybrid additive laminated bending die and the unlaminated punch was 1 mm (**Fig. 5.23b**). The experiments were performed on a Zwick250 universal testing machine.

For computing the radius before unloading (exactly after bending), the effect of springback (**Fig. 5.24a**) needs to be eliminated, i.e., subtracting the springback value from the measured radius of the sheet after unloading. Since the blank's width-to-thickness ratio (40 mm / 1 mm) is significant, it is safe to consider the plane strain state. Assuming a Poisson's ratio of 0.3 and substituting the values of width and thickness, the mean radius change (ΔR_m) caused by springback can be computed based on the classical bending theory as:

$$\Delta\left(\frac{1}{R_m}\right) = \frac{1}{R_m} - \frac{1}{R'_m} = 0.273 \cdot \frac{M_b}{E} \text{ with } M_b = \frac{1}{2\sqrt{3}} \cdot \sigma_f \cdot b \cdot t^2, \quad (5.12)$$

where M_b is the bending moment, R'_m is the bending radius after unloading, E is Young's modulus of the blank (E = 210 GPa), and σ_f is the flow stress. During the bending, the sheet faces strain hardening. Therefore, the corresponding flow stress needs to be determined. The bending equivalent plastic strain ($\bar{\varepsilon}_{Plastic}$) at the inner radius of the bent sheet is equal to:

$$\bar{\varepsilon}_{Plastic} = \frac{2}{\sqrt{3}}\left|\ln\left(1 - \frac{0.5}{5.5}\right)\right| = 0.095. \quad (5.13)$$

The corresponding flow curves (σ_f) for both blanks from the equivalent plastic strain of 0.095 based on Fig. 4.1 are 310 and 410 MPa for DC06 and HC380LA, respectively. The calculated inner radius (R_I) before springback at four preheating temperatures is shown in **Fig. 5.24b**. The inner radius before unloading has a maximum deviation from the nominal radius of 8 % and 10 % for DC06 and HC380LA without preheating. However, this deviation decreases to only 2 % at 300°C because the tool radius deposited at RT did not completely fill the step area, so the inaccuracy was high (Fig. 5.19). The surface roughness of the bent sheets with laminated bending dies at different preheating temperatures is presented in Fig. 5.24b. The average arithmetic roughness R_a decreases slightly as the preheating temperature increases for both blanks. Different preheating temperatures´ effect on the mean roughness depth (R_z) for both blanks is insignificant. Shortly, the effect of preheating on both surface roughness parameters of bent sheets is negligible. In the absence of additional data on tool wear in large-scale production at the various preheating temperatures, the tool presented without preheating is thus also adequate for efficient prototyping applications in particular.

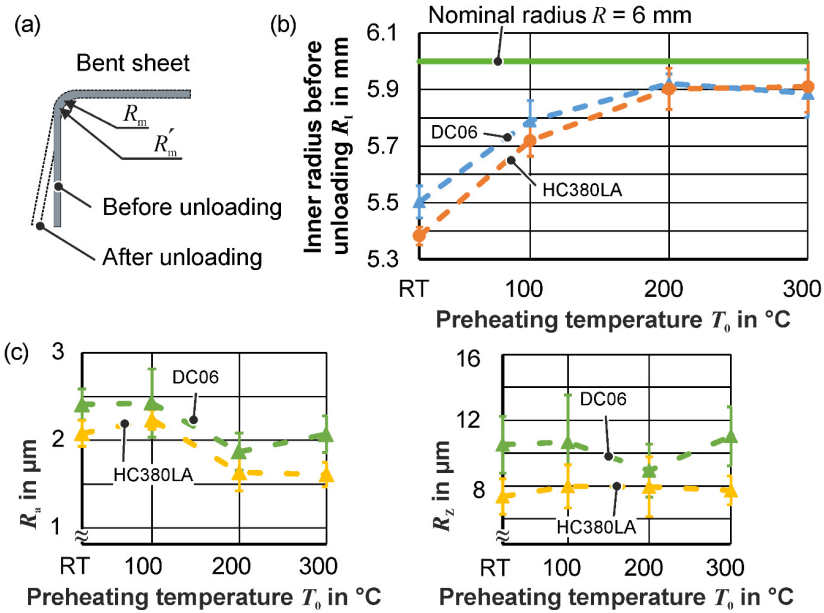

Figure 5.24: (a) Blank before unloading and after unloading, (b) inner radius before unloading in different preheating temperatures, (c) surface roughness parameters R_a and R_z

5.3 Tribological study of laminated tooling

The tribological properties of the tool surface play an essential role in the success of producing the parts. As mentioned in Fig. 2.8, different pre/post-processing methods exist to reduce the stair step of sheet lamination. The tool surfaces produced by LMD are potentially different from those that can be described as conventional. This section studies the tribological behavior of different tool surfaces produced by sheet lamination. The use of laser polishing for post-processing was not possible due to the high shape deformation of the sheets after laser polishing. Three basic friction elements were fabricated from 2 mm thick S355MC sheets: without LMD, with single and multiple LMD weld tracks **Fig. 5.25**. As a pre-processing step for the friction elements without LMD tracks, the sheets had to be chamfered at 45° with a water jet because the cut surface was too rough for a CO_2 laser. In addition, the friction elements were also milled (in their initial state) and ball-burnished. Ferro55 powder was used for the LMD. For reference, 1.2379 (X155CrVMo12-1) friction elements were also milled and gas nitrided (referred to as conventional). Fifteen different friction elements were produced.

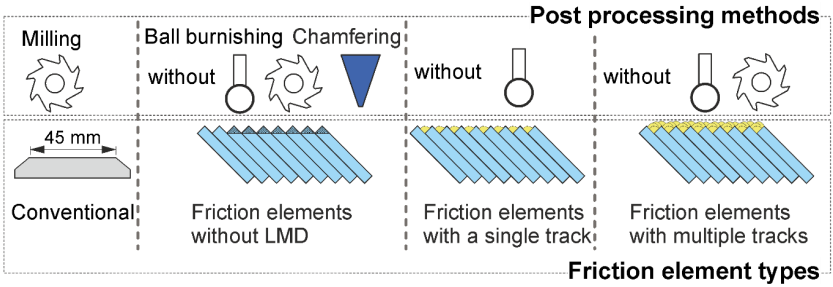

Figure 5.25: Friction element types and surface finishing methods

Strip tensile tests were performed at clamping pressures (P_C) of 4 and 12 MPa at drawing speeds of 10 and 50 mm/s with Iloform PN 226 lubricant. Each test was repeated at least three times.

The results of the coefficient of friction and roughness values for friction elements using the Ferro55 powder with HC380LA sheet strips are presented in **Fig. 5.26**. However, the higher clamping pressures result in lower coefficients of friction. There is no clear trend for the effect of drawing speed on the coefficient of friction. The LMD surfaces in the initial state have high peaks. These high peaks result in a smaller effective area in contact with the drawn sheets during the strip tensile test (due to the clamping force).

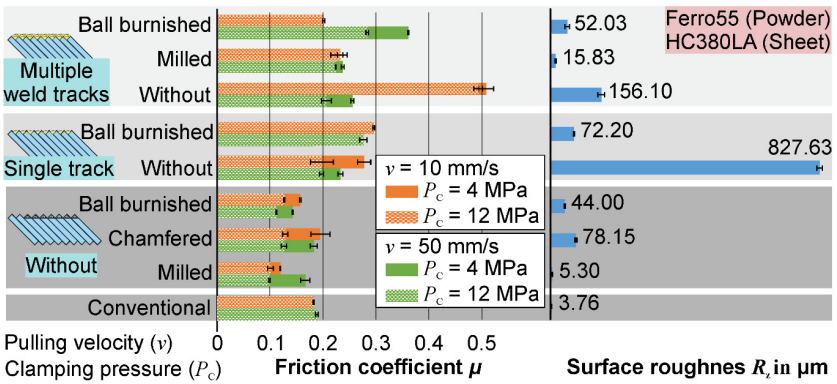

Figure 5.26: Coefficient of friction μ and roughness R_z of the friction elements

The friction coefficients of all friction elements with post-processing are equal to or even smaller than those of the conventional friction elements. It indicates that post-processing hybrid laminated tooling surfaces are necessary to achieve friction values comparable to those of the conventional method.

5.4 Summary

A two-step strategy is developed to ensure homogeneous surface roughness after deposition. As a first step in bonding, the results of tensile experiments for fillet weld track showed that the laser power above 1000 W and the feed rate 100 and 1200 mm/min ensure proper bonding, but the maximum fracture strength depends on the powder mass flow. Also, a 4 g/min powder mass flow provides at least 100 % stronger bonding for a 2 – 2 mm sheet combination. However, the substrate sheet's thickness must be considered when selecting the powder mass flow to avoid melting through the substrate.

The surface of one layer deposited area for the flat area shows that increasing the powder mass flow from 4 g/min to 8 g/min leads to higher surface roughness for both powders, up to 42 % for R_a. Increasing the laser power by 50 % from 800 W improves the surface roughness (R_a). Increasing the feed rate from up to 800 mm/min decreases the surface roughness by min 50 %, however, further increasing the feed rate has no significant effect on surface roughness.

By offsetting the tool sheets, the inhomogeneity of the deposited areas due to small step areas that cannot be properly reduced in the filling step is avoided. An offset of 1 mm gives promising results. Between deposition in the bonding track direction and along the radius direction, the radius direction gives 35 % (for R_a) better surface roughness in the radius direction. However, the deposition time is significantly longer (depending on the geometry), and the nozzle life is almost three times shorter.

Higher track-specific power density leads to smoother surfaces in both powders 316L-Si and Ferro55. Laser power is the main parameter affecting the surface roughness of deposited curved surfaces, followed by the laser's feed rate.

Preheating tool sheets is not recommended because of the increase in surface roughness, while the reduction in residual tensile stress at 100 °C is only 25 %. The functionality of the hybrid method for manufacturing the symmetrical bending dies is investigated. The EBSD results confirm the grain refinement (around 33 %) in the transition zone between the deposited area and the substrate sheet. It leads to higher hardness in the transition zone compared to the deposited area and the substrate sheet.

The tribological study shows that it is essential to achieve comparable results to improve the surface roughness of the deposited areas.

6 Realization of hybrid laminated tooling

Since sheet lamination allows using different materials for the tool sheets, the tool sheets should not be plastically deformed during the deep drawing process. The stress distribution of the laminated tool should be determined to avoid plastification of the tool sheets. Therefore, as a first step, a semi-analytical model is developed to determine the stress in the laminated tool in the critical area. Deep drawing experiments are performed in the next step to transfer the obtained knowledge to an axisymmetric deep drawing die. Laser polishing and ball burnishing are further investigated to analyze the effect of process parameters on the final tool surface roughness. Finally, a free-form demonstrator will be manufactured to verify the feasibility of producing complex shapes.

6.1 Semi-analytical approach for laminated tooling

Classical beam theory is used to determine the stress distribution. There are two ways to determine the stress distribution in a tool based on analytical models: classical beam theory or plate theory. The Kirchhoff-Love plate theory is the most famous theory (Love, 1888). In plate theories, the laminae (tool sheets) are considered as two-dimensional elements with large width-to-thickness ratios. Baratta (1981) showed that for metallic structures with a width-to-thickness ratio of less than 20, the stress values are less than one percent compared to plate theories using Timoshenko's beam theory. Since the laminations are under distributed compressive forces during the deep drawing process, the possibility of deformation of the tool sheet, such as anticlastic curvature, is low. Therefore, this approach uses the classical beam theory based on the Timoshenko beam to develop the analytical model.

The following assumptions are made to develop the semi-analytical model:

- Plane strain state
- Cross-section always remains plane
- Hook's law in the elastic range
- No slippage between the lamellae (due to welding of the layers)

MATLAB software is used to calculate the analytical model. In the deep drawing, the main forces are applied on the die from the blank holder and blank during the forming **Fig. 6.1a**. The resultant forming forces can be distributed as shown in **Fig. 6.1b**. For simplification, the forces are divided into constant vertical distributed force per length (q) and constant horizontal force (F_H), and the die radius is neglected for the sake of simplicity (**Fig. 6.1c**). The laminated tool consists of the n stacked beams with different thicknesses (t_i) and different Young's modulus (E_i) and moments of inertia (I_i).

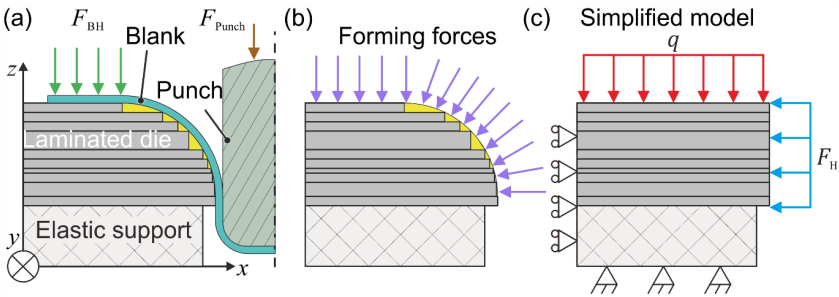

Figure 6.1: (a) Schematic of deep drawing, (b) forming forces applied on the laminated die, (c) simplified model with boundary conditions

The laminated tool (stacked beams) is supported by an elastic bed with an elastic modulus of k (**Fig. 6.2a**). The reaction pressure (P_r) from the elastic support on stacked beams. T_s is the total thickness of the stacked beam. The reaction pressure from the elastic support on the stacked beam can be calculated as:

$$P_r = k \cdot u(x_1), \tag{6.1}$$

where u is the displacement of the stacked beam. The simplified model replaces the elastic support with non-linear reaction pressure, as shown in **Fig. 6.2b**.

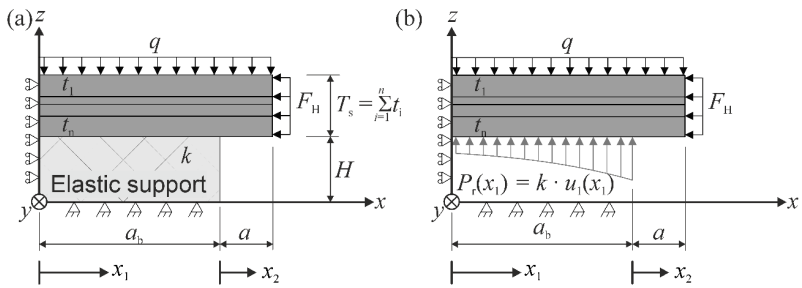

Figure 6.2: (a) Simplified model with defined geometries, (b) elastic support is repealed with distributed force

The neutral axis (N.A.) position on the z-axis (**Fig. 6.3a**) for the beam is where the longitudinal stress strains equal zero. For a multilayer beam it can be calculated based on Bareisis (2006):

$$z_{NL} = \frac{\sum_{i=1}^{n} D_i t_i + 2\sum_{i=2}^{n}\left(D_i \sum_{j=1}^{i-1} t_j\right)}{2\sum_{i=1}^{n} D_i}, \tag{6.2}$$

where the axial stiffness of each layer can be calculated as $D_i = E_i \cdot t_i \cdot w$ where E_i is Young's modulus of each layer, and w is the width of the stacked beams.

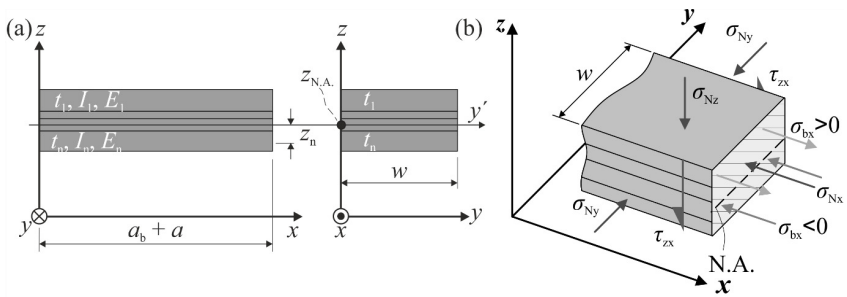

Figure 6.3: (a) Position of the neutral axis ($z_{N.A.}$) on the stacked bam, (b) applied forces and corresponding stresses on the stacked beam

The axial stiffness of a total stacked beam D can be calculated:

$$D = \sum_{i=1}^{n} D_i = w \sum_{i=1}^{n} E_i \cdot t_i \,, \tag{6.3}$$

It can be seen that the determination of the neutral layer of the stacked beam is a function of Young's modulus and the geometry. The total stiffness of the stacked beam is:

$$S = \sum_{i=1}^{n} S_i = \sum_{i=1}^{n} E_i \cdot I_i \,. \tag{6.4}$$

For rectangular beam elements, the moment of inertia of each layer of constant width w is calculated as follows:

$$I_i = w\left(\frac{t_i^3}{12} + t_i \cdot z^{*2}\right), \tag{6.5}$$

where the z^* is the distance of the neutral layer to the middle of the beam layer's cross-section.

$$z^* = z_n - \frac{t_i}{2} - \sum_{m=1}^{i-1} t_m. \tag{6.6}$$

The equivalent Young's modulus (E_{eq}) can be determined by the rule of the mixture and the corresponding equivalent moment of inertia (I_{eq}):

$$E_{eq} = \frac{S}{I_{eq}} \text{ where } I_{eq} = \frac{T_s \cdot w^3}{12}. \tag{6.7}$$

The stress state of the stacked beam for determination of the von Mises stress ($\sigma_{v.M}$) is illustrated in **Fig. 6.3b**. The normal stress along the x-axis resultant from the horizontal forces for each layer (Fig. 6.2b) equals:

$$\sigma_{\mathrm{Nx}_i} = \frac{F_\mathrm{H}}{w \cdot t_i}. \tag{6.8}$$

The normal forces in the x-direction caused by the bending moment (M_y) on each layer are:

$$\sigma_{\mathrm{bx}_i} = \frac{M_\mathrm{y} \cdot z_i}{S} \cdot E_i. \tag{6.9}$$

The resultant forces in the x-axis are the sum of the Eq.s (6.8) and (6.9).

$$\sigma_{\mathrm{xx}_i} = \sigma_{\mathrm{Nx}_i} + \sigma_{\mathrm{bx}_i} = \frac{M_\mathrm{y} \cdot z_i}{S} \cdot E_i + \frac{F_\mathrm{H}}{w \cdot t_i}. \tag{6.10}$$

The normal stress in the z-direction is equal to:

$$\sigma_{\mathrm{zz}_i} = \frac{q}{w}. \tag{6.11}$$

Considering the plane strain state ($\varepsilon_{\mathrm{yy}_i} = 0$):

$$\Rightarrow \sigma_{\mathrm{yy}_i} = \upsilon \cdot \left[\sigma_{\mathrm{xx}_i} + \sigma_{\mathrm{zz}_i}\right], \tag{6.12}$$

where υ is the Poisson's ratio. The shear stress due to the bending can be calculated based on **Eq. (6.13)**.

$$\tau_{\mathrm{zx}_i} = \frac{q(x)}{S \cdot w} \cdot \sum_{i=1}^{n} t_i \cdot E_i \cdot z_i. \tag{6.13}$$

The simplified model is divided into two main sections for calculation of the stresses, a supported area, and free length, as shown in **Fig. 6.4**.

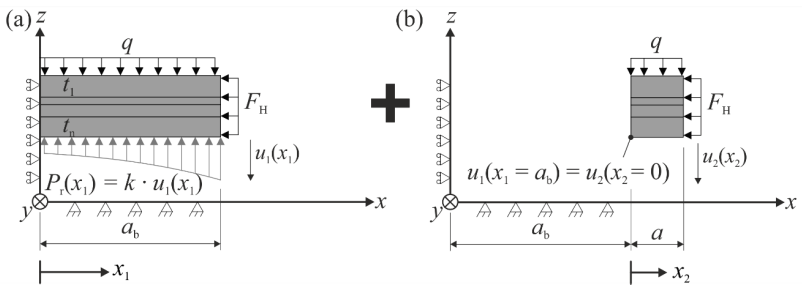

Figure 6.4: Stacked beam is discretized to (a) supported area, (b) free length

The boundary condition restricts the displacement in the x-axis at the position $x = 0$. In the supported area, the displacement of the whole beam is $u_1(x)$. The overhang-stacked beam can be considered an ordinary cantilever beam with the applied constant distributed horizontal force. The displacement of the overhang-stacked beam is $u_2(x)$.

The displacement in the point $u_1(x_1 = a_b) = u_2(x_2 = 0)$. Timoshenko and Gere (1985) define the bending of a beam-column as a fourth-order ordinary differential equation (ODE) provided:

$$E_{\mathrm{eq}} \cdot I_{\mathrm{eq}} \cdot \frac{d^4 u_1\,(x_1)}{dx_1^4} + F_H \cdot \frac{d^2 u_1(x_1)}{dx_1^2} = q_{\mathrm{r}}(x_1), \tag{6.14}$$

where based on Dankert and Dankert (2013), the force equilibrium in the beam-column with the supported bed is:

$$q_r(x_1) = q - k(z_1) \cdot u_1(x_1), \tag{6.15}$$

replacing the **Eq. (6.15)** on **(6.14)** for supported area yields:

$$E_{\mathrm{eq}} \cdot I_{\mathrm{eq}} \cdot \frac{d^4 u_1\,(x_1)}{dx_1^4} + F_{\mathrm{H}} \cdot \frac{d^2 u_1(x_1)}{dx_1^2} = q - k(z_1) \cdot u_1(x_1), \tag{6.16}$$

or reduced as:

$$u_1'''' + \frac{F_{\mathrm{H}}}{E_{\mathrm{eq}} \cdot I_{\mathrm{eq}}} \cdot u_1'' + \frac{k(x_1)}{E_{\mathrm{eq}} \cdot I_{\mathrm{eq}}} \cdot u_1(x) = \frac{q}{E_{\mathrm{eq}} \cdot I_{\mathrm{eq}}}, \tag{6.17}$$

by considering $F^* = \frac{F_{\mathrm{H}}}{E_{\mathrm{eq}} \cdot I_{\mathrm{eq}}}$, $k^* = \frac{k(x_1)}{E_{\mathrm{eq}} \cdot I_{\mathrm{eq}}}$, and $q^* = \frac{q}{E_{\mathrm{eq}} \cdot I_{\mathrm{eq}}}$, **Eq. (6.17)** can be simplified as:

$$u_1'''' + F^* \cdot u_1'' + k^* \cdot u_1(x_1) = q^*. \tag{6.18}$$

The second integration of **Eq. (6.18)** yields:

$$u_1''(x_1) = \frac{2}{L^2} e^{x_1/L} \left(-C_1 \sin\left(\frac{x_1}{L}\right) + C_2 \cos\left(\frac{x_1}{L}\right)\right) + \frac{2}{L^2} e^{-x_1/L} \left(C_3 \sin\left(\frac{x_1}{L}\right) - C_4 \cos\left(\frac{x_1}{L}\right)\right), \tag{6.19}$$

the forth integration, which is the displacement function for the supported area is:

$$u_1(x_1) = \frac{q}{k} + e^{x_1/L} \left(C_1 \cos\left(\frac{x_1}{L}\right) + C_2 \sin\left(\frac{x_1}{L}\right)\right) + e^{-x_1/L} \left(C_3 \cos\left(\frac{x_1}{L}\right) + C_4 \sin\left(\frac{x_1}{L}\right)\right), \tag{6.20}$$

where

$$L = \sqrt{\frac{4E_{\mathrm{eq}} \cdot I_{\mathrm{eq}}}{2 \cdot \sqrt{k \cdot E_{\mathrm{eq}} \cdot I_{\mathrm{eq}}} - F_{\mathrm{H}}}}. \tag{6.21}$$

In the case of a free length ($P_{\mathrm{r}}(x) = 0$) the forth-derivative equation is:

$$u_2''''(x_2) + F^* \cdot u_2''(x_2) = q^*. \tag{6.22}$$

The second integration yields:

$$u_2''(x_2) = \frac{q}{F_{\mathrm{H}}} + \cos(\sqrt{F^*} \cdot x_2) \cdot C_5 + \cos(\sqrt{F^*} \cdot x_2) \cdot C_6, \tag{6.23}$$

and the displacement function of the free length is:

$$u_2(x_2) = \frac{q \cdot x_2^2}{2F_{\mathrm{H}}} + \frac{cos(\sqrt{F^*} \cdot x_2)}{F^*} C_5 + \frac{sin(\sqrt{F^*} \cdot x_2)}{F^*} C_6 + C_7 \cdot x_2 + C_8. \quad (6.24)$$

Eight equations for the boundary conditions can calculate the constant parameters C_1 to C_8. The boundary conditions based on (Dankert and Dankert, 2013) are:

$$u_1(x_1 = 0) = \frac{q}{k} \quad (6.25)$$

$$u_1'(x_1 = 0) = 0 \quad (6.26)$$

$$u_1(x_1 = a_b) = u_2(x_2 = 0) \quad (6.27)$$

$$u_1'(x_1 = a_b) = u_2'(x_2 = 0) \quad (6.28)$$

$$u_1''(x_1 = a_b) = u_2''(x_2 = 0) \quad (6.29)$$

$$u_1'''(x_1 = a_b) = u_2'''(x_2 = 0) \quad (6.30)$$

$$u_2''(x_2 = a) = 0 \quad (6.31)$$

$$u_2'''(x_2 = a) = 0. \quad (6.32)$$

where $x_1 = 0$ because of the compression of the stacked beam, therefore the displacement at this point is equal to q/k (**Eq. (6.25)**). At $x_1 = 0$, the bending angle (u_1') is equal to zero, as mentioned in **Eq. (6.26)**. At the intersection line of supported and free length, the displacement, bending angle, bending curvature, and bending moment due to beam continuity are equal. At $x_2 = a$, where the end of the stacked beam is, the bending moment and shear force equal zero. The constant parameters C_1 to C_8 are calculated by applying the boundary conditions (**Appendix B**).

The von Mises general stress is:

$$\sigma_{\mathrm{v.M}} = \sqrt{{\sigma_{\mathrm{xx}}}^2 + {\sigma_{\mathrm{yy}}}^2 + {\sigma_{\mathrm{zz}}}^2 - \sigma_{\mathrm{xx}} \cdot \sigma_{\mathrm{yy}} - \sigma_{\mathrm{xx}} \cdot \sigma_{\mathrm{zz}} - \sigma_{\mathrm{yy}} \cdot \sigma_{\mathrm{zz}} + 3{\tau_{\mathrm{yz}}}^2 + 3{\tau_{\mathrm{xz}}}^2 + 3{\tau_{\mathrm{xy}}}^2}, \quad (6.33)$$

where in the supported area of the stacked beam, it is equal to:

$$\begin{cases} \tau_{\mathrm{xy}} \approx 0 \\ \tau_{\mathrm{yz}} \approx 0 \end{cases} \Longrightarrow \sigma_{\mathrm{v.M}} = \sqrt{{\sigma_{\mathrm{xx}}}^2 + {\sigma_{\mathrm{zz}}}^2 - \sigma_{\mathrm{xx}} \cdot \sigma_{\mathrm{yy}} - \sigma_{\mathrm{xx}} \cdot \sigma_{\mathrm{zz}} - \sigma_{\mathrm{yy}} \cdot \sigma_{\mathrm{zz}} + 3{\tau_{\mathrm{zx}}}^2}, \quad (6.34)$$

The corresponding von Mises stress by substitution of Eqs. (6.11), (6.12) in (6.13) and (6.34) for the i^{th} lamella is given with a Poisson's ratio of 0.3:

$$\sigma_{\mathrm{v.M}_i}^2 = 0.79 \cdot \left({\sigma_{\mathrm{xi}}}^2 + \left(\frac{q}{w}\right)^2\right) - \sigma_{x_i} \cdot \frac{q}{w} + 3\tau_{zxi}^2. \quad (6.35)$$

The von Mises stress of the sheet should be less than the tensile yield strength ($\sigma_{\mathrm{v.M.}} < R_{\mathrm{p0.2}}$) to be sure that the tool sheets will not be plastically deformed during the deep drawing process.

A Finite Element Method (FEM) with the software ABAQUS implicit (version 2020) is used to evaluate and improve the analytical model. The proposed simplified forming die aims to represent the deep drawing process. Since the proposed simplified analytical model cannot properly express the deep drawing process, this further analysis aims to improve the developed model compared to the actual deep drawing die.

The semi-analytical model is implemented in MATLAB software. To evaluate the semi-analytical model as a first step, a deep drawing with a DC06 blank is performed in ABAQUS to find the maximum contact pressures in the horizontal and vertical directions. The max. contact pressures are 31.11 MPa and 45.22 MPa in the horizontal and vertical directions, respectively (**Fig. 6.5**). Therefore, for the rest of the simulations, the horizontal pressure of $\frac{F_H}{T_s \cdot w} = 30$ MPa, and the vertical pressure of $\frac{q}{w} = 45$ MPa are used. However, it should be noticed that the maximum contact pressures do not happen simultaneously, and by considering the maximum stresses, the semi-analytical results are in the upper bound.

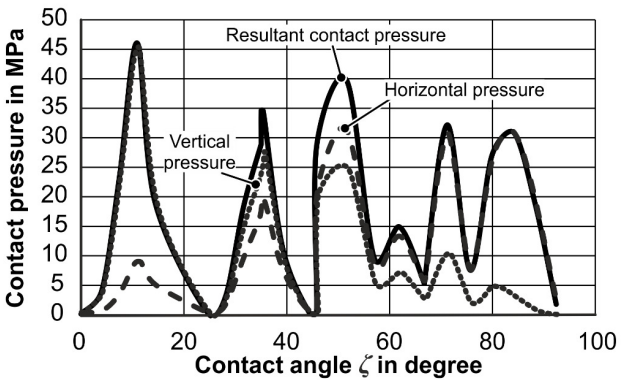

Figure 6.5: Contact pressures for deep drawing of DC06

Based on a convergence study, a mesh size of 0.1 mm is selected for 2D simulations. However, the computational time with the 0.1 mm mesh size was very intensive in 3D simulations, so the 1 mm mesh size is used. For generalization, the following normalized parameters are defined. The normalized von Mises stress ($\sigma_{\text{v.M.}}^{\text{N}}$) is defined as:

$$\sigma_{\text{v.M.}}^{\text{N}} = \frac{\sigma_{\text{v.M.}} - \sigma_{\text{v.M.}}^{\min}}{\sigma_{\text{v.M.}}^{\max} - \sigma_{\text{v.M.}}^{\min}}. \tag{6.36}$$

The normalized length in the x-direction (x^{N}) is equal to (see Fig. 6.2a):

$$x^{\text{N}} = \frac{x}{a_{\text{b}} + a}. \tag{6.37}$$

The normalized length in the thickness direction (z^{N}), also see Fig. 6.2a, is:

$$z^{\mathrm{N}} = \frac{z - H}{T}. \tag{6.38}$$

Since determining the von Mises stress in the whole stacked-beam analytically for each process parameter requires a lot of computing power and is time-consuming, the numerical analysis is utilized to determine the section where the maximum stress exists in the stacked-beam. To do this, the stress state along the *x*-direction (**Fig. 6.6a**) is determined numerically in three layers (top, middle, and bottom).

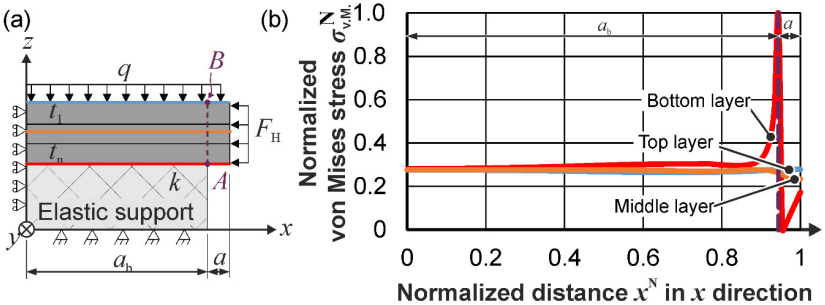

Figure 6.6: (a) Selected layers in stacked-beam, (b) normalized von Mises stress ($\sigma^{\mathrm{N}}_{\mathrm{v.M.}}$) distribution in the top, middle, and bottom layers along normalized *x* direction (x^{N})

The normalized von Mises stress ($\sigma^{\mathrm{N}}_{\mathrm{v.M.}}$) results in the top, middle, and bottom layers as illustrated in **Fig. 6.6b**. It shows that the maximum normalized von Mises stress happens in the bottom layer in point *A*, since there is no support in the bottom layer. This result is in agreement with (Hölker, 2014).

In all calculations, it is important to determine the stress in the thickness direction to ensure that the design criterion is met. Therefore, the von Mises stress is determined along the thickness from point *A* to *B,* as shown in Fig. 6.6a, by knowing that the maximum stress occurs at point *A* at the bottom of the tool sheets.

As a case study for a specific setup, the result of the von Mises stress distribution along the thickness direction for the analytical model (trend line) is compared with the FEM simulation (**Fig. 6.7**). The analytical model shows higher von Mises stress at the bottom of each layer compared to the top of each layer. The analytical model underestimates the equivalent stress at point *A* and near the bottom of the beam. However, it overestimates the equivalent stresses in other areas. There is a nearly accurate estimate of the equivalent stress at point *B*. At point *B*, the stresses acting in the beam are similar to cantilever beams with a sufficient supported layer, which can also be predicted by the analytical model.

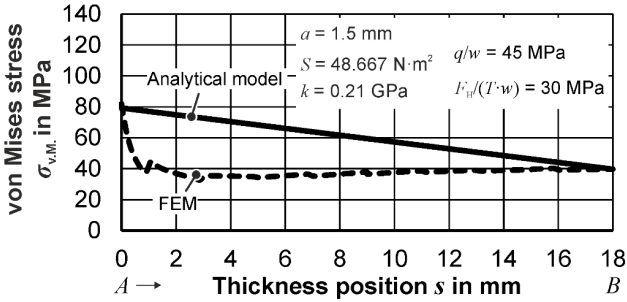

Figure 6.7: Comparison between the analytical model and FEM model

One possible reason for the higher stresses in the analytical model is the consideration of the same initial distributed vertical forces on all layers. The other possible reason for this difference is the lack of contact modeling between layers, i.e., friction forces in the analytical model. Several FEM simulations with different materials, bending stiffness (S), and overhang length (a) with steel support are performed to improve the analytical model to study the stress distribution in the thickness direction from point A to B. The FEM results shown in **Fig. 6.8** illustrate the results of the normalized stresses in the thickness direction.

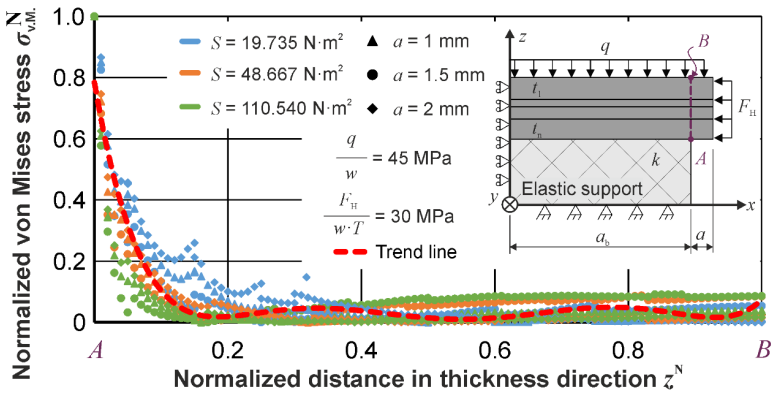

Figure 6.8: FEM results for normalized von Mises stress ($\sigma^{N}_{v.M.}$) along A-B points for different materials and free lengths

The trend of the stress distribution is almost equal for all setups, which shows a saturation of the stress after some layers toward the top of the stacked-beam. The trend line can be interpolated using regression models and applied to the analytical model to enhance the accuracy. The normalized von Mises stress would be a function of the normalized position in the thickness direction as:

$$\sigma_{\text{v.M.}}^{\text{N. Inter.}}(z) = b_0 + b_1 \cdot (z^{\text{N}}) + b_2 \cdot (z^{\text{N}})^2 + \cdots + b_{\text{j}} \cdot (z^{\text{N}})^{\text{j}}. \tag{6.39}$$

A convergence study is done to identify the degree of the polynomial of the trend line (**Fig. 6.9**). The results show a polynomial of 6 degrees ($j = 6$) provides an adequate *R*-squared (R^2) value. The *R*-squared value is the percentage of the change in the dependent variable, which is predictable based on the independent variables. The higher R^2, the more accurate the regression.

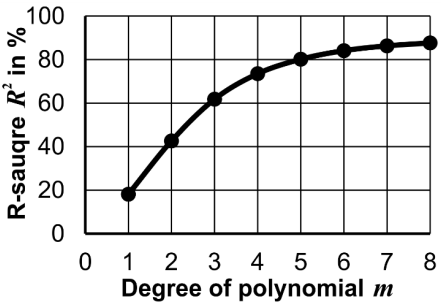

Figure 6.9: Convergence study of polynomial degree *m*

To determine the value of the coefficients b_0 till b_{j}, a full factorial design of experiments with a total of 486 simulation data is performed. In the simulations, the equivalent Young's modulus (E_{eq}) varied from pure aluminum to steel (E_{eq} = 60 to 210 GPa), and the overhang's length (a) changed from 1 to 3 mm. The regression is performed with Design software version 12 from the company Stat-Ease. The results of the regression are shown in **Table 6.1**.

Table 6.1: Fit statics results for the regression model

Parameter	Value	Parameter	Value
Standard deviation	0.032	Standard deviation	0.032
R-squared	0.94	*R*-squared	0.94
Adequate precision	93.0	Adjusted *R*-squared	0.94

Substituting the values of b_0 to b_{j} based on the output of regression in **Eq. (6.39)** yields:

$$\begin{aligned}\sigma_{\text{v.M.}}^{\text{N. Inter.}}(z) &= 0.79 - 13.12(z^{\text{N}}) + 81.4(z^{\text{N}})^2 \\ &-243.7(z^{\text{N}})^3 + 379.7(z^{\text{N}})^4 - 288.7(z^{\text{N}})^5 + 86.6(z^{\text{N}})^6.\end{aligned} \tag{6.40}$$

The analytical model cannot predict the maximum value of the von Mises stress in point *A*. Based on the performed numerical analysis, the analytical model generally underestimates the maximum stress at point *A* by around 45 %, so a correction factor of $\Lambda = 1.45$ is taken to improve the prediction of the maximum von Mises stress at point *A*. The value of the correction factor (Λ) is the mean value of the correction factors for all

simulations compared with the analytical model. Based on it the corrected maximum von Mises stress ($(\sigma_{\text{v.M.}}^{\max})_{\text{cor.}}$) from the analytical model is equal to:

$$(\sigma_{\text{v.M.}}^{\max})_{\text{cor.}} = \Lambda \cdot (\sigma_{\text{v.M.}}^{\max})_{\text{Analytical}}. \tag{6.41}$$

The von Mises stress based on the semi-analytical model can be calculated as:

$$\sigma_{\text{v.M.}}^{\text{semi}} = \sigma_{\text{v.M.}}^{\text{N. Inter.}} \cdot \left((\sigma_{\text{v.M.}}^{\max})_{\text{cor.}} - \sigma_{\text{v.M.}}^{\min}\right) + \sigma_{\text{v.M.}}^{\min}. \tag{6.42}$$

There is a satisfactory agreement between the outputs of the developed semi-analytical model and the numerical verification for various boundary conditions and geometries for stacked beams (**Fig. 6.10**).

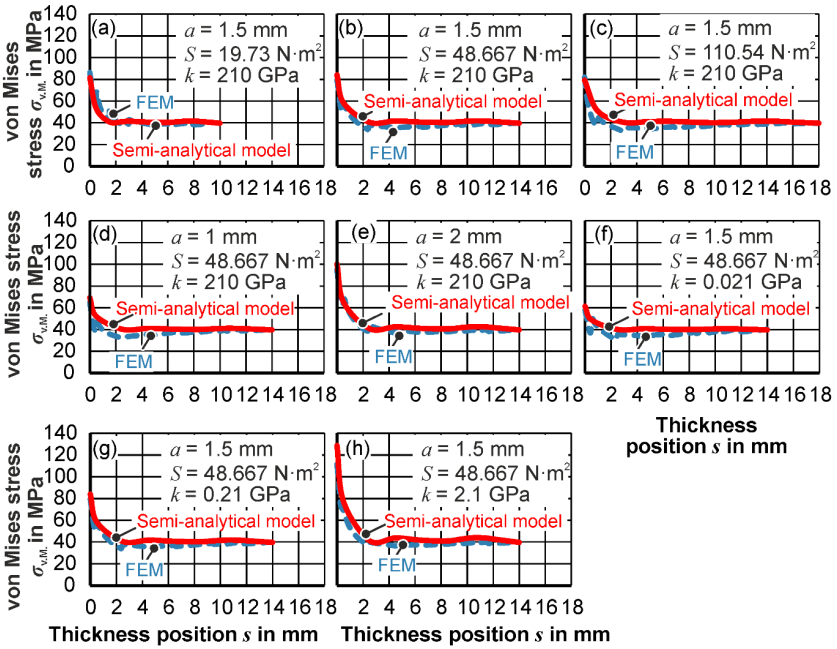

Figure 6.10: Comparison of the semi-analytical model with the FEM model for different boundary conditions and geometries for stacked beams (a - h)

The comparison of the semi-analytical model with FEM for the different stacked-beam stiffness (S = 19.37, 48.667, and 110.54 N·m^2) shows an overestimated maximum of 29 % (**Fig. 6.10a**, **b**, and **c**). For different free lengths (a =1.0; 1.5; 2.0), the predicted von Mises stress has a maximum overestimating of 12 % (**Fig. 6.10b**, **c**, and **e**). The different stiffnesses of the supported beam (k = 210, 21, 0.21, and 0.021 GPa) have a maximum overestimating of 13 % (**Fig. 6.10b**, **f**, **g**, and **h**). The possible reasons for

such deviations are assumptions in the analytical model, stress concentrations in the corner areas (leading to higher stresses), and the effect of the mesh size in simulations.

The effect of different equivalent Young's modulus (E_{eq}) of the stacked-beam determined by the semi-analytical model is shown in **Fig. 6.11**. The von Mises stress $\sigma_{v.M.}$ reduces by increasing E_{eq}. After this sharp decrease (2 mm from point *A*) a large von Mises stress saturation area towards point *B* exists. It means that the top sheets are not faced with high stresses, and only the bottom sheets (near point *A*) require high strength. This enables the application of low-strength sheets, i.e., increased selection window of different materials and more cost-effective tooling.

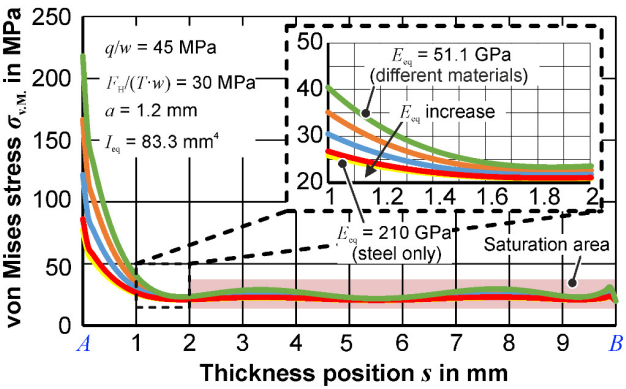

Figure 6.11: Effect of equivalent Young's modulus (E_{eq}) on von Mises stress ($\sigma_{v.M.}$) along laminae thickness distribution. The sheet order (based on thickness) is: 2, 0.5, 1, 1, 1, 0.5, 1, 0.5, 2, and 0.5 mm from points *A* to *B*

In the case that from a mechanical loading point of view, the sheet thickness combination doesn't play a crucial role, the optimum choice of combination should be considered from a rather economic point of view, which will be addressed in Chapter 7.5.

6.2 Deep drawing experiments

The simple symmetrical deep drawing dies are manufactured based on the results of the previous sections with die radii of 6 and 8 mm. Both Ferro55 and 316L-Si powders were used for reducing the stair step effect with bonding and filling parameters as presented in Chapter 5.2 for both powders (only $P = 1200$ W during filling step). The spiral strategy is used for the two final deposition layers. The step over of 0.2 mm with spiral strategy (same strategy as for the final layer) is used for the laser polishing. Besides, without any post-processing dies, three post-processing (milling, ball burnishing, and

laser polishing) are applied to the manufactured deep drawing dies. Milling is performed with a face milling tool with a diameter of 60 mm, a tool rotation speed of 4500 rpm, and a feed rate of 2000 mm/min with an overlap of 0.07 mm. The deep drawing tests were performed for each die at least three times, according to Chapter 4.1.7. Deep drawing dies (with the same radii) are also milled out of material 1.7225/42CrMo4 and gas nitriding based on the conventional method as a reference. The dies and deep-drawn cup radii and surface roughnesses are measured at four points (0°, 90°, 180°, and 270°) with the optical profilometer (Keyence), and the median value is calculated. The dies are cut and prepared for hardness measurements as presented in Chapter 4.2.1.

The Ferro55-die radius for the nominal radius of 6 mm has a very small deviation (+0.08 ± 0.09 mm) for the case without any post-processing (**Fig. 6.12**). For applying the milling, an extra layer with a thickness of ca. 0.35 mm is deposited to achieve the nominal radius later by milling. The die radius with milling has a small deviation (+0.08 ± 0.11 mm). For ball burnishing as a second post-processing method, a ball with a diameter of 12.7 mm and fluid pressure of 30 MPa (for Ferro55 powder) with a tool overlapping of 0.1 mm was used. The smoothing tracks by ball burnishing were parallel to the bonding tracks. The ball burnishing shows the maximum deviation from the nominal radius (-0.88 ± 0.26 mm). The reason for such a smaller die radius is the plastic deformation during the smoothing step. It shows the necessity of the extra deposition layers to achieve the exact nominal radius. A laser with a power of 1200 W in spiral form (parallel to the filling tracks) was used for laser polishing. The radius of the laser-polished die shows a lower deviation than the ball-burnished (-0.28 ± 0.17 mm). The reason for such a deviation is remelting the surface and filling the valley during laser polishing. An extra layer is also a necessity for post-processing by this method.

The effect of the manufactured die radii is also reflected in the deep-drawn cups. The cup deep drawn with the ball-burnished die has the maximum deviation (ca. 11.6 %) from the nominal cup radius (R = 6 mm). The cups deep-drawn by the laser-polished die have a deviation of 5 %, and the cups drawn with the milled die have only a 1.67 % deviation.

The surface roughness of the LMD-die without any post-processing is 480 % higher than the tool surface roughness by the conventional method. The conventional die surface roughness is R_z = 8.52 ± 0.3 µm for the die radius of 6 mm. As with the radius accuracy, the best surface roughness is given for finishing by milling, ball burnishing, and laser polishing. There are scratches on the surface of the ball-burnished dies due to the accessibility limitation of the ball-burnishing tool, especially in narrow inner diameters. The same problem could be caused by milling (it was not the case here) when the diameters are small. The main advantage of laser polishing is the working distance due to the laser focal point. It enables the treatment of the surface located in narrow areas. Yet, the main disadvantage is the reduction of the tool's hardness. However, the

surface roughness of the ball-burnished and laser-polished dies depends on the process parameters.

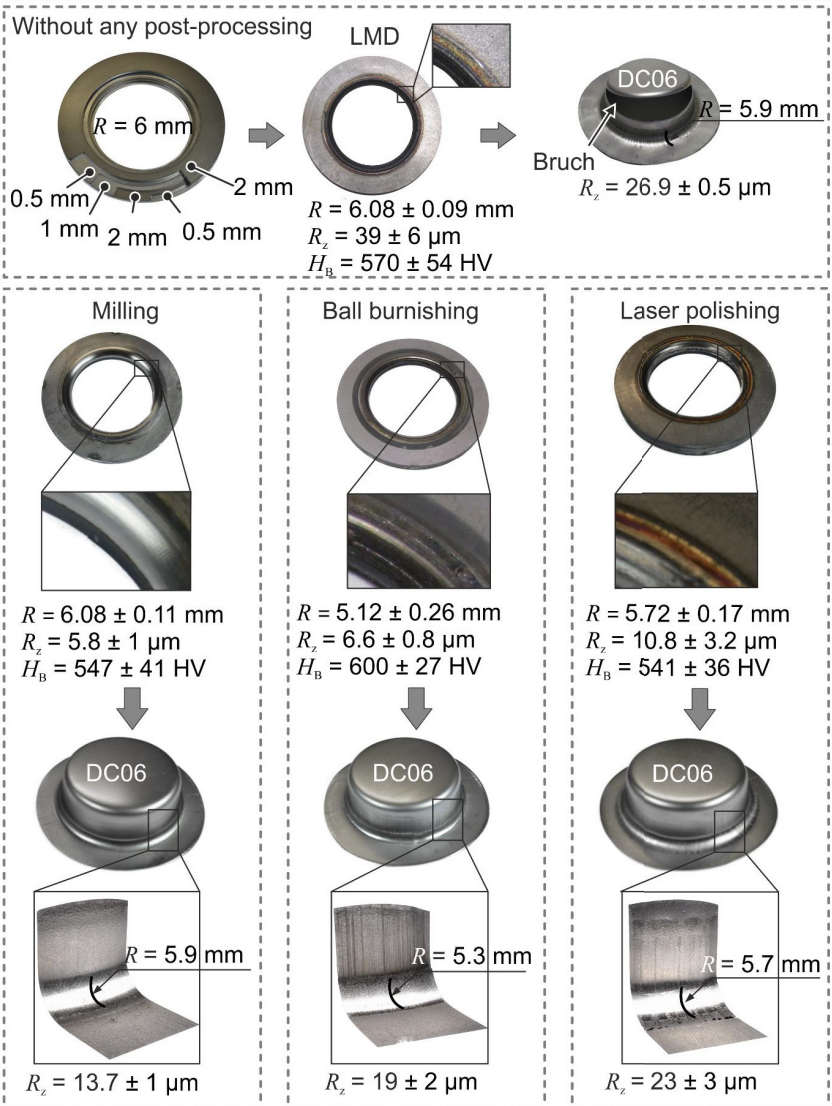

Figure 6.12: Manufactured dies and deep-drawn cups by the hybrid method

In ball burnishing, the process parameters such as applied pressure on the surface, overlapping value, ball diameter, and strategy play an important role. In laser polishing, the overlapping value, laser beam diameter, laser power, feed rate, and strategy are influencing parameters. The hardness measurement results show that the post-processing with ball burnishing can increase the initial hardness of the deposited die (around 5.2 %) without any hardening process and make it comparable with the conventional die with hardening (only 25 % lower than the conventional). The hardness of the die decreases by around 5 % for both milled and laser-polished dies. The reason for this reduction in laser-polished die is the reheating.

Deep drawing tests are performed with a deep drawing ratio of 1.93 ($\beta = D_B / D_P$). A drawing depth of 21 mm for the dies without any post-processing leads to the cup fracture for both blanks (compare Fig. 6.12 for DC06). The maximum deep drawing depth of 13.5 mm for DC06 and 12.5 mm for 6 and 8 mm die radii were achievable with a deep drawing ratio of 1.93.

6.3 Laser polishing and ball burnishing

Since the surface roughness of ball-burnished and laser-polished areas is highly dependent on the applied process parameters, an additional study is performed to compare these two methods.

The proper process parameter is determined during laser polishing on flat surfaces based on the deposited areas, as shown in Fig. 5.12. The laser polishing power P_P and feed rate f_P are varied between 400 - 1000 W and 400 - 1000 mm/min with a 1.2 mm hatch distance for bidirectional raster. For both powders, the same process parameters are studied (**Table 6.2**).

Table 6.2: Process parameters for laser polishing on the flat surface

No.	Laser power P_P (W)	Feed rate f_P (mm/min)	Ratio λ (J/mm)	No.	Laser power P_P (W)	Feed rate f_P (mm/min)	Ratio λ (J/mm)
1	1000	1000	60	7	600	700	54
2	800	1000	48	8	400	700	36
3	600	1000	36	9	1000	400	150
4	400	1000	24	10	800	400	120
5	1000	700	84	11	600	400	90
6	800	700	66	12	400	400	60

The ratio of λ is the applied energy per unit length, which is the ratio of the laser polishing power over the laser polishing feed rate ($\lambda = P_P / f_P$). The different combinations can deliver the same λ. It needs to be considered that there are two same λ values ($\lambda = 60$ J/mm) with 1000 W and 1000 mm/min and 400 W and 400 mm/min

(experiments 1 and 12). The surface roughness change R'_a (average roughness) is calculated as:

$$R'_a = \frac{(R_a^L - R_a^0)}{R_a^0}, \tag{6.43}$$

where R_a^0 is the average surface roughness of the die directly after deposition and R_a^L is the surface roughness after the application of laser polishing. The laser polishing is applied on different deposited surfaces (with different track-specific power densities), as presented in Fig. 5.12.

The results show that the not necessary higher track-specific power (θ) leads to surface roughness improvement (**Fig. 6.13**). For 316L-Si power, the maximum reduction is around 80% with applied 120 J/mm energy. However, at around λ = 85 J/mm, the surface roughness reduction is maximum by considering all the track-specific power density (θ) values.

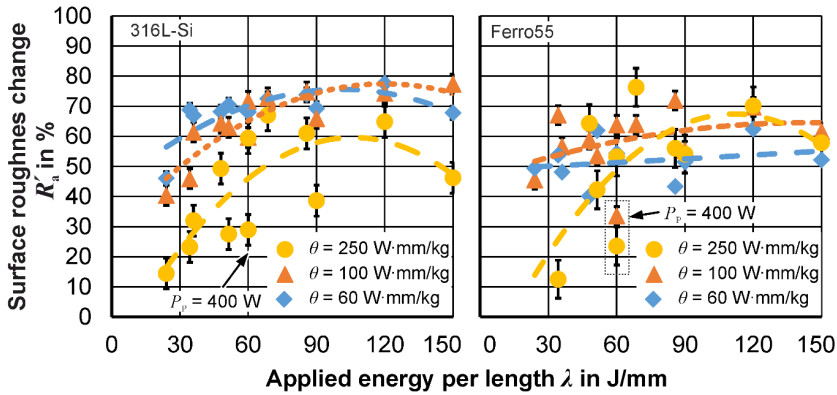

Figure 6.13: Effect of applied energy per length by laser polishing on different deposited surfaces (different energies)

For Ferro55 powder at λ = 120 J/mm, all θ values show the maximum surface roughness improvement. High energy per length values create a big melting pool, while cooling creates a rougher surface as a surface over-melt (SOM) mechanism. At the same time, the low values of λ are not able to melt the rough surface properly and can only improve the surface by a limited amount.

The effect of laser polishing on the surface roughness of the curved surfaces is investigated with the die segments with a radius of 10 mm. Two different laser spot diameters (laser nozzles with diameters of 1.6 and 3 mm) are used to study the laser

polishing effect in both radius and deposition directions. Based on the results of Fig. 6.13 for Ferro55 powder, a laser power of $P_P = 800$ W and feed rate $f_P = 400$ mm/min ($\lambda = 120$ J/mm) and 316L-Si powder $P_P = 1000$ W, and feed rate $f_P = 700$ mm/min ($\lambda = 85$ J/mm) is selected. The laser spot diameter of 1.6 mm, the hatching distances (h_d) were 0.1, 0.2, 0.4, 0.6, 0.8, and 1 mm. For a laser spot diameter (d_L) of 3 mm, the hatching distances were 0.2, 0.4, 0.8, 1.2, 1.6, and 2 mm for both powders. The surface roughness in the radius direction is measured as mentioned in Chapter 4.2.1 with the Keyence profilometer with 20 lines, a distance of 20 pixels, and a cut-off length of 0.8 mm. The hardness after laser polishing was also measured. The initial surface roughness of the deposited area for 316L-Si is $R_a^0 = 5.46 \pm 0.89$ µm and for Ferro55 is $R_a^0 = 5.73 \pm 0.96$ µm. The surface roughness change is calculated based on Eq. (6.43), and the hardness change is also calculated based on:

$$H'_B = \frac{(H_B^{h_d} - H_B^0)}{H_B^0}, \tag{6.44}$$

where H_B^0 is the initial hardness of the deposited area $H_B^0 = 212.4 \pm 10.74$ HV10 for 316L-Si powder and $H_B^0 = 534.4 \pm 16.74$ HV10 for Ferro55 powder. $H_B^{h_d}$ is the hardness of the deposited area after each hatching distance. The surface roughness change for the 316L-Si deposited area in the radius direction shows that the mean surface roughness (R_a) improves by a maximum of 75 % compared to the initial state (as deposited) by the laser spot diameter of 1.6 mm (**Fig. 6.14**). By increasing the hatching distance from 0.4 to 1.0 mm, the surface roughness improvement decreases to 66 % by using the laser spot diameter of 1.6 mm. Different hatching distances have an insignificant effect on the surface roughness improvement for the laser spot diameter of 3 mm. In the case of Ferro55 powder, the surface roughness can be improved by 71 % on average. The laser polishing time can be reduced by choosing larger hatch spacing for the same surface roughness improvement.

The hardness of the 316L-Si deposited area increases by a maximum of 10 % with the laser spot diameter of 1.6 mm at low hatching distances (Fig. 6.14). At higher hatching distances, laser polishing has an insignificant effect. With the laser spot diameter of 1.6 mm, the effect is the same for Ferro55 powder, with the only difference being that the hardness increases by up to 15 %.

The effect of laser polishing with the laser spot diameter of 3 mm is small for the 316L-Si deposited area. However, it improves the hardness up to 17 % for Ferro55 deposited area at hatching distances less than 0.8 mm. The larger hatching distance along the radius direction for 316L-Si powder causes the deposited surface to become softer. This softening for stainless steel is due to the low local energy input (low-temperature gradient) and the low cooling rate, which is not the case at small hatching distances.

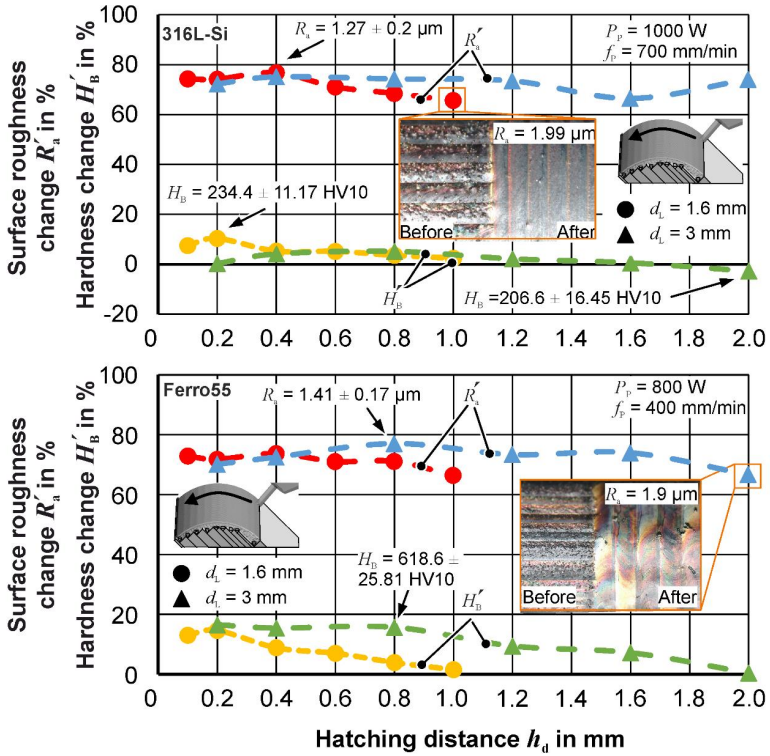

Figure 6.14: Effect of laser spot diameter and hatching distance on arithmetic mean deviation (R_a) and hardness of the deposited curved surfaces by laser polishing in the radius direction

The laser polishing along the weld direction is performed with the same process parameters. The surface roughness of the 316L-Si deposited area, regardless of the laser spot diameter and hatching distance, can be improved by around 59 % (**Fig. 6.15**). The hatching distance does not affect the deposited areas by Ferro55 with the laser spot diameter of 1.6 mm. The laser spot diameter of 3 mm for the deposited material from Ferro55 at 0.2 mm hatching distance showed a surface roughness improvement of only 37 %. In contrast, increasing the hatching distance increases this value to the saturated value of around 69 %. A high number of picks due to the high number of passes at the hatching distance of 0.2 mm explains the rougher surface roughness along the radius compared to the hatching distance of 2 mm for the laser spot diameter of 3 mm (Fig. 6.15).

Both laser spot diameters increase the hardness of the deposited area out of 316L-Si only by a maximum of 9 % at lower hatching distances, where the higher distances also lead to a softening (Fig. 6.15). The hardness of the deposited Ferro55 can also be increased only by 15 % by the laser spot diameter of 3 mm.

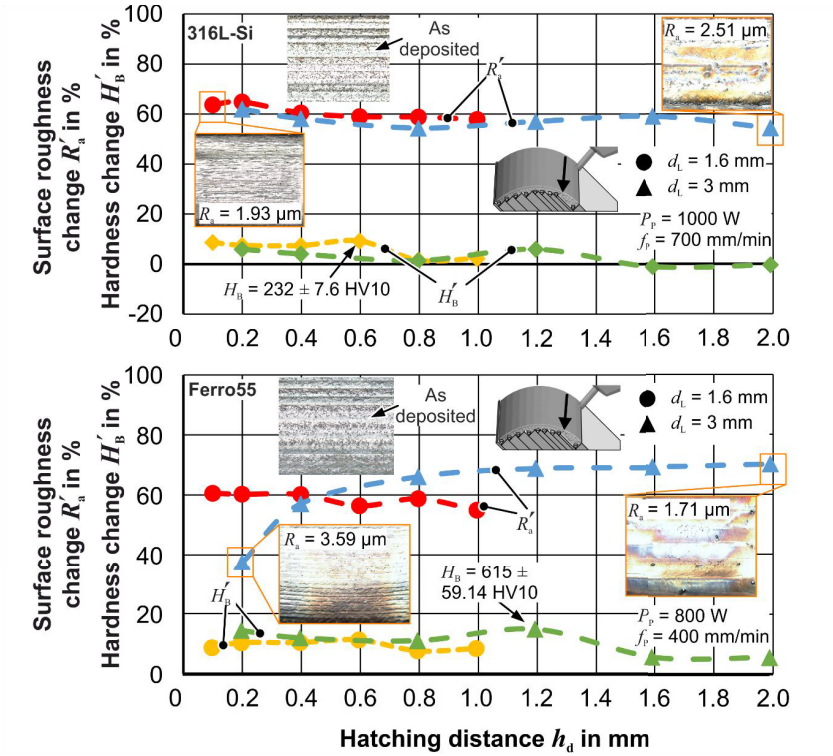

Figure 6.15: Effect of laser spot diameter and hatching distance on arithmetic mean deviation (R_a) and hardness of the deposited curved surfaces by laser polishing in the weld direction

The result of the laser polishing within the mentioned parameters shows that laser polishing has a positive and significant effect on the improvement of the surface roughness, and it can enhance surface roughness by a maximum of 78 % by selecting the proper process parameters. However, the hardness is increased by 17 %, whereas greater hatching distances can lead to softening.

The effect of different hatching distances of ball burnishing on the surface roughness and hardness of deposited curved areas are also analyzed. The experiments are

performed with a minimum hatching distance of 0.2 mm and a maximum of 6 mm with a hatching increase of 0.2 mm. The ball burnishing tool with a diameter of 12.7 mm is used. For the deposited area out of Ferro55, a hydraulic pressure of 300 bar and for the 316L-Si, 250 bar are used. Both toolpath strategies, along the radius direction and along the bonding track direction, are studied.

The arithmetic mean deviation improvement (R_a) is reduced by increasing the hatching distances in the tool path along the radius direction. A maximum surface roughness improvement of 78 % ($R_a = 1.2 \pm 0.18$ µm) for 316L-Si deposited area and only a maximum of 45 % ($R_a = 3.14 \pm 0.39$ µm) be achieved at a hatching distance of 0.2 mm (**Fig. 6.16**).

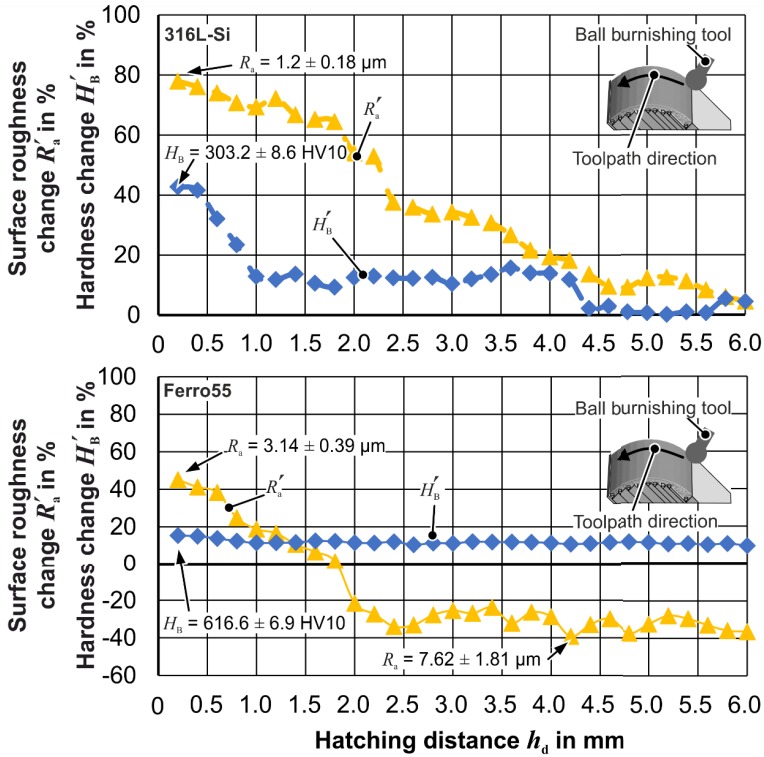

Figure 6.16: Effect of hatching distance on mean surface roughness (R_a) and hardness of the deposited curved surfaces by ball burnishing in the radius direction

The surface roughness change in the deposited area by 316L-Si is always positive (for along the radius direction strategy). It means the mean surface roughness improvement decreases, and there is no effect at 6 mm hatching distance. The lower hatching distance leads to more plastic deformation. For Ferro55, the maximum surface roughness improvement can achieved at the lowest hatching distances.

The outcome of the surface roughness and hardness change along the weld direction (bonding direction) by ball burnishing is presented in **Fig. 6.17**. In the weld direction strategy for 316L-Si deposited areas, the mean surface roughness can be improved by 58 % ($R_a = 2.2 \pm 0.52$ µm) where at a hatching distance of 3.4 mm the hatching distance effect is insignificant and greater hatching distances leads to rougher surface roughness.

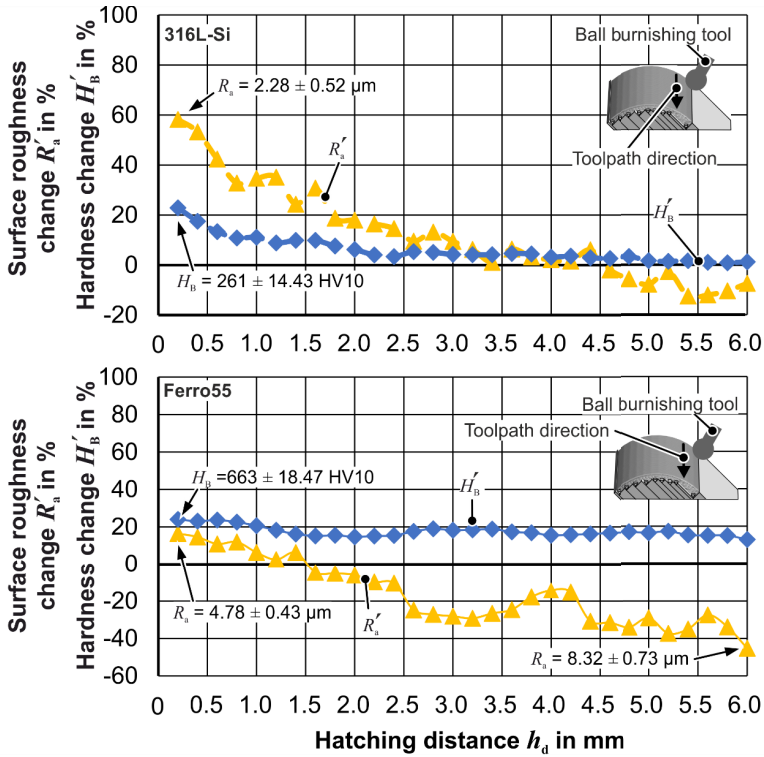

Figure 6.17: Effect of hatching distance on arithmetic mean deviation (R_a) and hardness of the deposited curved surfaces by ball burnishing in the weld direction

For Ferro55-deposited surfaces, the surface roughness quality is worse at higher hatching distances above 1.6 mm. The reason is because of the diameter of the ball-

burnished tool and high hatching distances. The ball burnishing tool cannot cover all surfaces (no contact), and it just stretches some areas and increases surface roughness. The hardness change (H'_B) of the 316L-Si deposited areas sharply decreases after 0.4 mm hatching distance from 43 % to 13 % at 1 mm hatching distance. Then there is saturation, and the hardness change reduces to almost zero from 4.4 mm hatching distance. For deposited areas with Ferro55, the hatching distance has an insignificant effect, and the hardness increases by almost 12 % ($H_B \approx 599$ HV10).

6.4 Wear study

For wear experiments, dies with a radius of 8 mm with the same condition as deep drawing only with an initial blank radius of 120 mm were performed. The sheets for lamination are ordered as top 2, 0.5, 1, 1, 2, 1, and 0,5 mm. Ferro55 and 316L-Si powders are used to reduce the stair-step areas, and in all experiments, the HC380LA high-strength steel blank (t_b = 1 mm) is used as the blank for deep drawing. As a reference for the conventional die, an 8 mm radius die made of 1.7225/42CrMo4 material is milled and hardened (gas nitrided). For all dies up to 1000 strokes, the radius and surface roughness are measured after every 200 strokes. After 1000 strokes, no further experiments are performed on the conventionally manufactured die and the hybrid-milled die. After 1000 strokes, microscopic (change in surface roughness) and macroscopic (change in radius) changes in every 1000 strokes are measured. For four hybrid dies (two powders and two post-processing methods), up to 10,000 strokes are executed. For comparison between the conventional die and dies manufactured with the hybrid method, the surface roughness change (R'_z) is calculated as:

$$R'_z = \frac{(R_z^S - R_z^0)}{R_z^0}, \tag{6.45}$$

where R_z^0 is the initial surface roughness of the die after deposition and post-processing and R_z^S is the surface roughness of the die for the corresponding stroke. Although the conventional die with a hardness of 642 ± 13 HV10 has a better surface roughness even after 1000 strokes, the hybrid dies show lower wear (surface roughness increase) than the conventional die. The surface roughness of the conventional die is worse, around 60 %, than the initial condition (**Fig. 6.18**). The surface roughness increase (wear) in all hybrid methods is lower than in the conventional die. Yet, the maximum surface roughness of the conventional die is R_z = 9.3 µm after 1000 deep drawings, which is lower than the surface roughness of the hybrid die R_z = 21.7 µm. The surface roughness after 200 strokes improves in the hybrid method for laser polishing and ball burnishing, which can be explained by removing or smoothing the weak spatters and surface picks by the first series of deep drawing experiments.

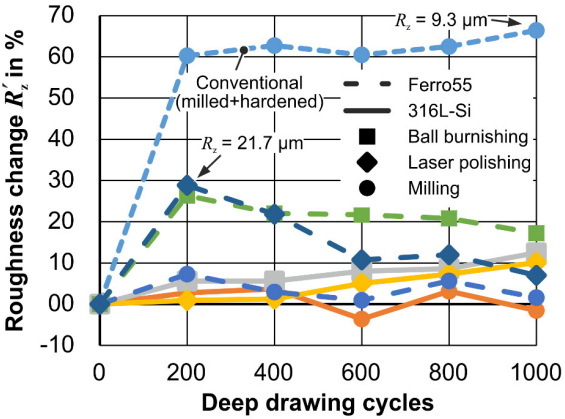

Figure 6.18: Comparison of surface roughness change of dies till 1000 strokes

The die radius reduction is calculated based on **Eq. (6.46)**.

$$R' = \frac{(R^0 - R^S)}{R^0}, \tag{6.46}$$

where R^0 is the initial radius of the die after manufacturing and R^S is the die radius for the corresponding stroke. The dies manufactured by the conventional method and the post-processed with milling show no radius change (**Fig. 6.19**), whereas the dies manufactured by deposition of 316L-Si powder and post-processed by ball-burnished and laser polished show a high radius reduction.

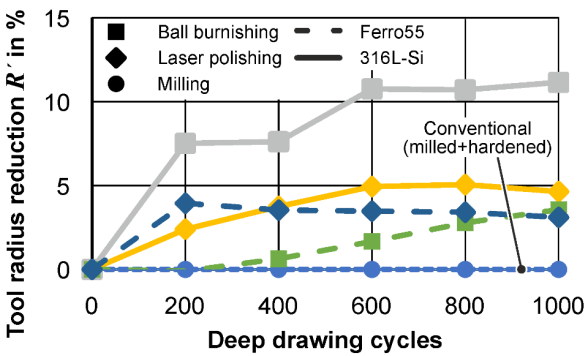

Figure 6.19: Tool radius reduction of conventional die compared with hybrid dies

The reason for that is the low hardness and stiffness of the 316L-Si material compared to Ferro55. The jagged surface roughness causes a high abrasion on the surface and

reduces the tool radius. The hybrid dies are manufactured with Ferro55 powder and post-processed by ball burnishing due to higher hardness showing lower radius reduction (Fig. 6.19). The maximum radius reduction in hybrid dies with the Ferro55 is 3 %, and for the 316L-Si, it is around 12 % for laser-polished ones. After 1000 strokes, the surface roughness of the dies manufactured by 316L-Si improves because of the high abrasion, which is not the case for Ferro55 dies (**Fig. 6.20**).

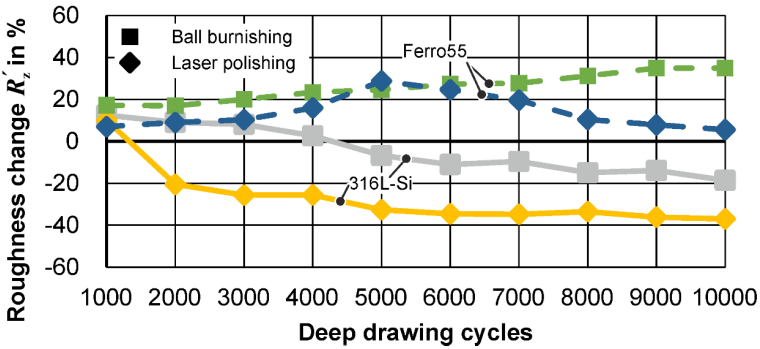

Figure 6.20: Comparison of surface roughness change for deep-drawn cups from 1000 to 10,000 strokes

The surface roughness of the ball-burnished die out of Ferro55 shows the maximum surface roughness increase among the other die due to the higher hardness. In the case of the laser-polished die, after 5000 cycles, the surface roughness of the die improves as a sign of starting the die wear (Fig. 6.20). The surface roughness of 316L-Si powders increases sharply, whereas, at 10,000 strokes, the surface roughness improves almost 40 % for laser-polished die, where the die radius decreases by around 12 % (**Fig. 6.21**).

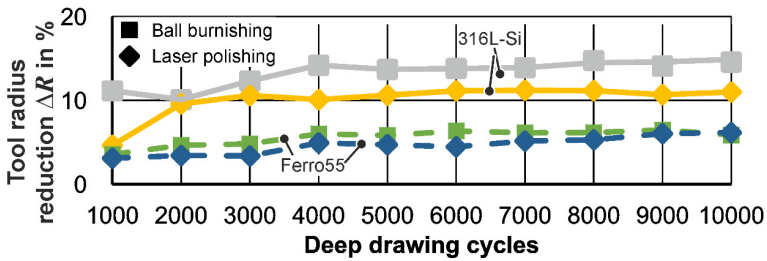

Figure 6.21: Tool radius reduction of hybrid dies from 1,000 to 10,000 cycles

The ball-burnished die out of 316L-Si shows the maximum radius reduction; however, the surface roughness improvement is lower than the laser-polished die. There is an insignificant difference in radius change between laser polishing and ball burnishing for

Ferro55-dies; after 10,000 cycles, it is around a maximum of 7 %. The hybrid Ferro55-dies are suitable for high cycles of deep drawing regardless of the post-processing method, which is not the case for hybrid 316-Si-dies.

6.5 Transfer to complex shapes (demonstrator)

Since the parts in the industry are more complex than simple axisymmetric parts, a complex shape with freeform surfaces with an external geometry of 450 × 326 × 15 mm^3 is selected to be manufactured by the hybrid method (**Fig. 6.22**).

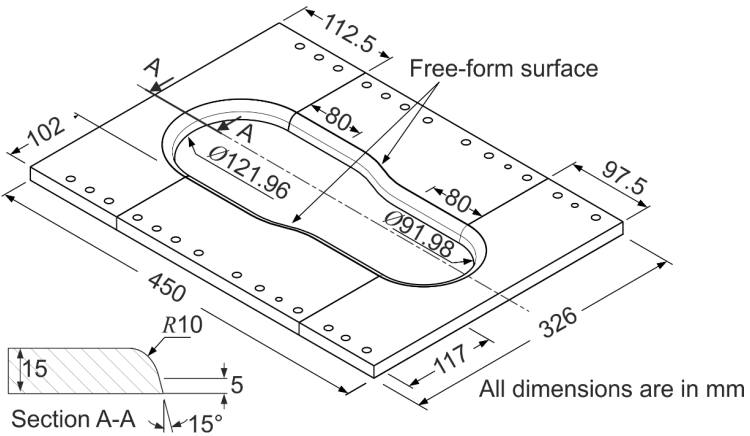

Figure 6.22: Schematic view and geometry of the demonstrator

For manufacturability, the die is segmented into four segments. The die has a corner radius of R = 10 mm and is chamfered at an angle of 15° to the vertical axis. The selected sheet combination for lamination is 2; 0,5; 1; 2; 1; 1; 2; 0,5; 2; 2; 1 mm from top to bottom. For reducing the stair-step areas, the two-step strategy (Fig. 5.14c) with the deposition process parameters is presented in **Table 6.3**.

Table 6.3: LMD Process parameters for demonstrator

Step	**Power *P*** (W)	**Feed rate *f*** (mm/min)	**Powder mass flow $\dot{m}$** (g/min)
Bonding	1400	1000	7
Filling	1000 (316L-Si) 1200 (Ferro55)	1000	4
Laser polishing	1000 (316L-Si) 800 (Ferro55)	700 (316L-Si) 400 (Ferro55)	-

The offset of b = 1 mm is used for cutting the sheet (not for the top and bottom sheets). Due to high energy input because of the large deposition area, the segments at the end are delaminated (**Fig. 6.23a**). Therefore, the ends of segments are welded by applying

pure laser (without any powder) at the same setup before deposition (**Fig. 6.23b**). A laser power of 1800 W is used to melt and join the sheets from the outer side of the segments. The outside surfaces of the dies are manually polished after joining to prevent misalignment of the inserts on the base plate during assembly. Both laser polishing and ball burnishing are used to improve the surface roughness after the deposition.

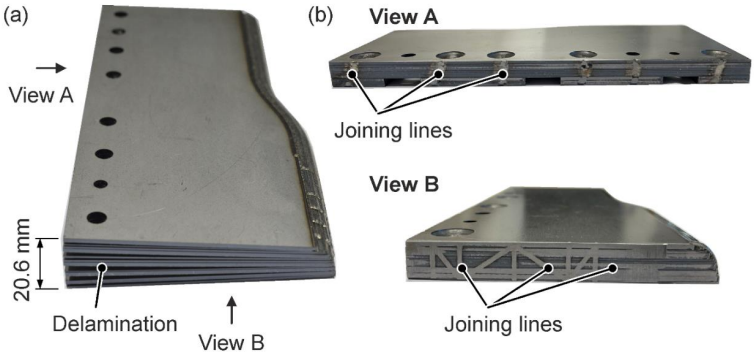

Figure 6.23: (a) Sheet delamination after deposition, (b) joining lines for inserts

The large stair-step area in the demonstrator leads to high energy input, i.e., high heating and cooling cycles, which affect the bonding tracks' hardness. Therefore, the hardness of the bonding track after the deposition layer is measured, as shown in **Fig. 6.24**.

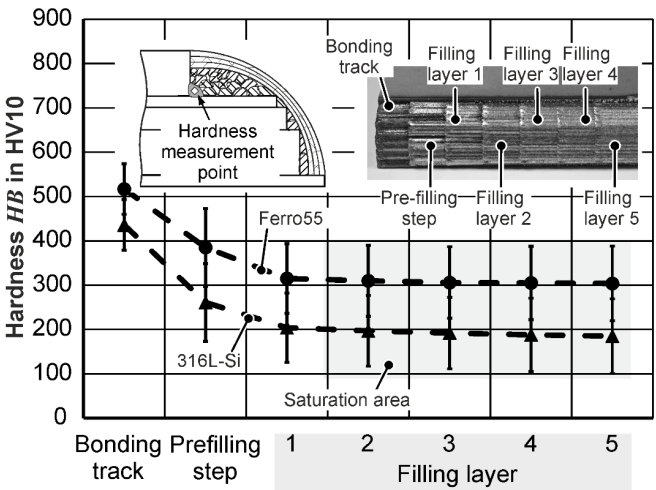

Figure 6.24: Bonding track's hardness change during the different depositions

The hardness decreases sharply directly after the deposition of the prefilling step, and this decrease continues by the deposition of the first filling layer. Next, there is no significant change in the hardness of the bonding track, and there is a hardness saturation for both powders. The hardness for Ferro55 powder is ca. 310 HV10, and the hardness for 316L-Si is around 200 HV10. The reason for saturation is increasing the distance of the energy source from the bonding track, which no longer influences the hardness.

The demonstrator's inserts require two different tool path strategies. The insert with semicircles requires a circular tool path, whereas the inserts with free-form surfaces require a linear tool path strategy. The measured surface roughness for both types of inserts shows that by the same laser metal deposition parameters, the maximum peak surface roughness parameter (R_z) of the circular strategy is around 19 %, which is higher than the linear tool path strategy (**Fig. 6. 25**). It is due to the deviation of the feed rate of the laser head by circular movements, which are smaller than nominal feed rate values. Laser polishing as a post-processing method can improve the surface roughness of the circular tool path strategy more than the linear one due to the higher energy input by slower laser head movement, especially for Ferro55 powder.

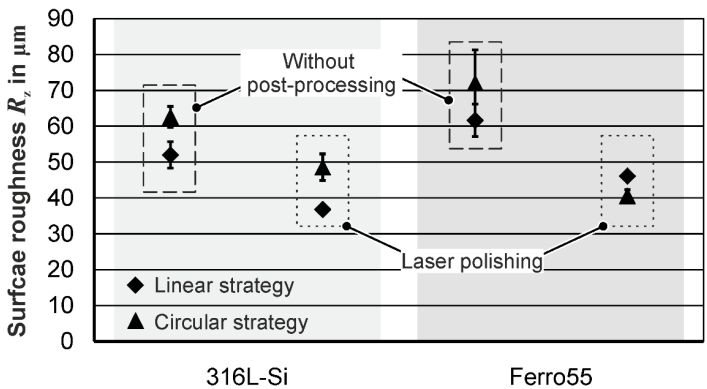

Figure 6.25: Effect of different strategies on surface roughness

The deep drawing experiments are carried out with DC06 and HC380LA blanks of 1 mm thickness, as described in subchapter 4.1.8. The oval-shaped blanks are laser cut with an external geometry of 441 × 281 mm^2. Ferro55 and 316L powders are used with laser-polished dies (**Fig. 6.26a**). The part's maximum achievable deep drawing depth was 40 mm for both blanks. The surface roughness of the deep-drawn parts along the radius direction is almost identical for both drawn parts (**Fig. 6.26b**). Taking into account the cutting of the tool sheets, the deposition time, and the laser polishing, the total manufacturing time for this set of inserts is approximately 4 hours and 25 minutes. Considering the hardness of the tool, the quality of the surface roughness, the variety of

material choices, and the geometry of the die, the die manufacturing time is much faster than that of the conventional method, which requires hardening.

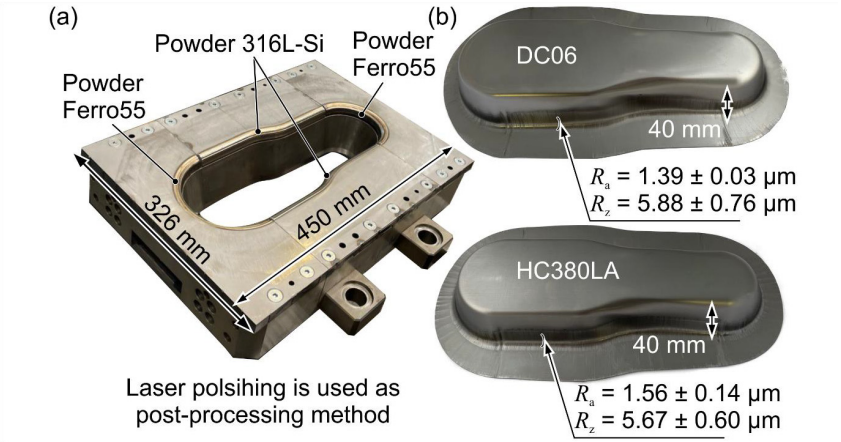

Figure 6.26: (a) Manufactured hybrid laminated demonstrator die, (b) deep-drawn parts from DC06 and HC380LA with a thickness of 1 mm

6.6 Summary

The developed semi-analytical model shows the possibility of using low-strength sheets near the tool surface and high-strength sheets at the bottom of the laminated die.

Deep drawing with the manufactured laminated dies for axisymmetric parts shows promising results. The various post-processing methods showed that the surface roughness and hardness of the dies depend on the process parameters. Laser polishing can improve the surface roughness by an average of 71 % and 59 % for the deposited curved areas of Ferro55 and 316L-Si, respectively. The hardness of the deposited area at small hatching distances (around 0.2 mm) can also be improved by a maximum of 17 % and 15 %, respectively, for Ferro55 and 316L-Si areas, but higher hatch distances (greater than 1.8 mm) have either no effect or even softening.

Ball burnishing with 0.2 mm hatch spacing along the radius strategy can improve surface roughness by 78 % (Ferro55) and 45 % (316L-Si). Increasing the hatching distance of ball burnishing along the radius direction above 1.4 mm for Ferro55 deposited areas increases the surface roughness up to 40 %. The hardness of the deposited areas in both strategies (along the radius and along the weld line) can be increased by max. 23 % for Ferro55, regardless of the hatching distance. However, for 316L-Si, the hardness increase highly depends on the hatch distance and the strategy applied. The maximum hardness can be increased up to 45 % (for the along radius strategy).

The wear test results show that the 316L-Si laminated dies are suitable for small series production (less than 1000 strokes) because the surface roughness increase and radius reduction (wear) due to low hardness are significant (about 40 %). In contrast, the Ferro55 laminated dies show only about 7 % wear after 10,000 cycles.

The hybrid process gives the possibility to produce large dies with freeform surfaces in a short time with adequate surface roughness and hardness, demonstrating the industrial transferability of the proposed concept.

7 Technological, economic, and energetic evaluation

The previous sections illustrated the application and potential of using the combination of laser metal deposition with sheet lamination to manufacture forming tools. In the following chapter, the economic and energetic aspects of the hybrid process (**Fig. 7.1a**) are compared with pure laser metal deposition followed by milling (**Fig. 7.1b**) and with the conventional method (**Fig. 7.1c**). Three different manufacturing routes are schematically compared in Fig. 7.1.

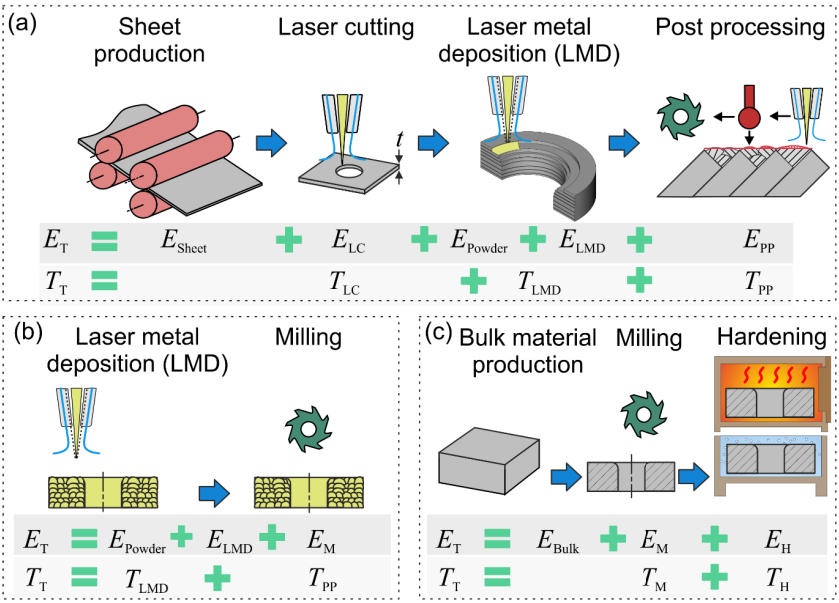

Figure 7.1: Process route for calculation of total energy consumption (E_T) and production time (T_T) for: (a) hybrid additive laminated tooling, (b) pure LMD with milling as post-processing, (c) conventional method

The following steps are considered to calculate the energy consumption of each one. For the hybrid additive laminated tooling (Fig 7.1), the total consumption energy is:

$$E_T^{Hybrid} = E_{Sheet} + E_{LC} + E_{Powder} + E_{LMD} + E_{PP}, \quad (7.1)$$

where E_{Sheet} is the energy required for the production of the sheet. The cutting energy (E_{LC}) is needed for laser cutting with a laser machine. The energy required for deposition is the sum of the energy needed for powder production (E_{Powder}) and the energy necessary for deposition with a laser beam (E_{LMD}). Different post-processing energies (E_{PP}), such as milling (E_M), ball burnishing (E_B), and laser polishing energy (E_{LP}), are used based

on the selected process in **Eq. (7.1)**. The total energy for the conventional method (**Fig. 7.1b**) is the sum of the energy required for manufacturing the bulk material (E_{Bulk}), consumed energy for milling, and the energy necessary for hardening. Finally, for the pure LMD method (**Fig. 7.1c**), the energy required for powder production plus deposition with the used energy for milling is considered.

The required time for producing sheet metal, bulk material, and powder is not considered for calculating the total production time (T_T) for each process (hybrid, conventional, and fully LMD followed by milling).

7.1 Hybrid additive lamination method

As the production energy and time for a systematic assessment are highly dependent on the workpiece geometry and dimensions, a reference workpiece is assumed to have a square shape with length l and a cylindrical hole with diameter d in the middle (**Fig. 7.2a**). The n number of sheets with a constant thickness of t are stacked to generate the target part. The thickness of the part is c, a fraction of the length l. The part's mass is (m_P), and the mass of the scrap is (m_s). Each sheet must be cut outside and inside (**Fig. 7.2b**) and stacked to build the final part geometry.

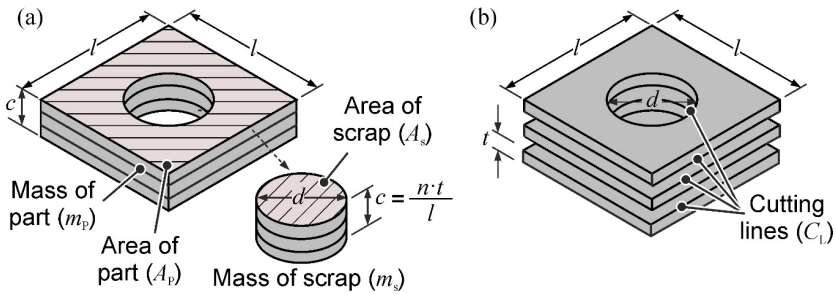

Figure 7.2: (a) Assumed geometry for evaluation, (b) cut lines of the final part

The ratio of X can be defined as the material yield, which is the ratio of the final part mass to the sum of the raw material as presented in **Eq. (7.2)**. Since the density of all layers is the same, the yield ratio can be considered as the part's area (A_P) over the area of the initial area ($A_P + A_s$). The parameter d can be derived as a function of material yield and length (l), as shown in Eq. (7.2).

$$X = \frac{m_P}{m_P + m_s} = \frac{A_P}{A_P + A_s} = 1 - \frac{\pi d^2}{4l^2} \Rightarrow d = l \cdot \sqrt{\frac{4(1-X)}{\pi}} \tag{7.2}$$

By considering the volume constancy and using the same density (ρ), the length ratio c can be calculated as:

$$c \cdot l^3 = \frac{m_P}{X \cdot \rho} \Rightarrow l = \sqrt[3]{\frac{c \cdot m_P}{X \cdot \rho}} \tag{7.3}$$

The total cutting length is the sum of the perimeter of the square and the hole:

$$C_L = (4l + \pi d)n \overset{n=\frac{l}{ct}}{\Longrightarrow} (4l + \pi d)\frac{l}{c \cdot t} = \frac{1}{4t}\left(\frac{c \cdot m_P}{X \cdot \rho}\right)^{\frac{2}{3}} \cdot \left(\sqrt{4\pi(1-X)} + 4\right) \tag{7.4}$$

It is assumed that all used sheets are steel with a density (ρ) of 7.9 kg/cm^3. The material yield (X) is also considered to be 60 % (i.e., 60 % of the total raw material mass used for the final part), and the length-thickness ratio is 25 %. The cutting length (C_L) based on the assumed values for three different sheet thicknesses is shown in **Fig. 7.3**.

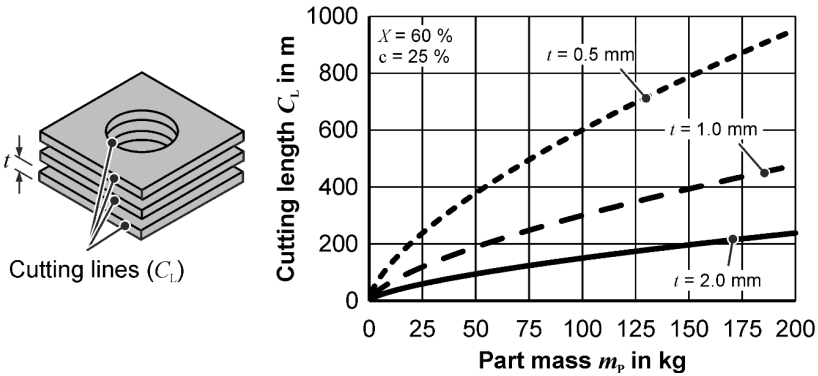

Figure 7.3: Calculated cutting length (C_L) for different sheet thicknesses as a function of part mass (m_P)

For the same part mass 4 and 2 times, the cutting tool needs to travel for 0.5 and 1 mm sheet thickness, respectively, compared to 2 mm sheet thickness. In hybrid additive laminated tooling, it is assumed that the sheets are cut by laser. The laser cutting parameters depend on the sheet material and thickness. A laser machine (TCL 1005) from the company Trumpf GmbH + Co. KG with a maximum laser power of 3000 W is used to calculate the energy consumption of laser cutting. **Table 7.1** shows the recommended laser power and feed rate for cutting different steel sheets.

Table 7.1: Process parameters for laser cutting the different sheet thickness

Thickness	**Laser power P_{LC}** (W)	**Feed rate f_{LC}** (m/min)
0.5 mm	1700	9
1.0 mm	1700	8
2.0 mm	1200	5

The machine manufacturer for laser cutting (Trumpf) calculated the machine's energy consumption (E_M) as a function of the used laser power, as shown in **Fig. 7.4**. The laser power for 0.5 and 1 mm sheet is around 57 % of the maximum laser power of the machine (P_{max} = 3000 W), which means the consumed energy for these sheets are equal to E_M = 42 kWh, and for 2 mm sheet thickness E_M = 38 kWh.

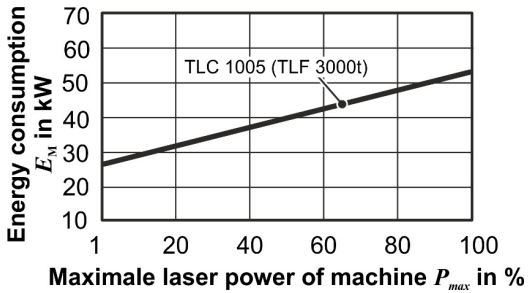

Figure 7.4: Energy consumption by TCL 1005 laser machine

Based on the consumed laser power for each sheet and using the cutting length with the corresponding feed rate, the total consumption energy for each sheet thickness can be calculated as:

$$E_{LC} = \frac{E_M \cdot C_L}{f_{LC}}. \tag{7.5}$$

The results of cutting energy for different sheet thicknesses show that the thinner sheet thickness (higher laser cutting distance (C_L) for the same part mass (m_P)) requires higher energy consumption (**Fig. 7.5a**).

For calculating the time for laser cutting length (T_{LC}), the time for positioning and replacing the sheets is not considered. The laser cutting time is calculated as follows:

$$T_{LC} = \frac{C_L}{f_{LC}}. \tag{7.6}$$

The plotted results (**Fig. 7.5b**) show that the lower sheet thickness requires longer laser cutting time. For the production of the sheets based on Sato and Nakata (2020), the energy needed for the production of 1 kg sheet is equal to 19.37 MJ. The energy required for the production of sheets (E_{Sheet}) is calculated as the sum of the mass of the part and the scrap, i.e.:

$$E_{Sheet} = 19.37 \left[\frac{MJ}{kg}\right] \cdot (m_P + m_s) = \frac{19.37 \left[\frac{MJ}{kg}\right]}{X} \cdot m_P, \tag{7.7}$$

Eq. (7.7) is not dependent on the sheet thickness.

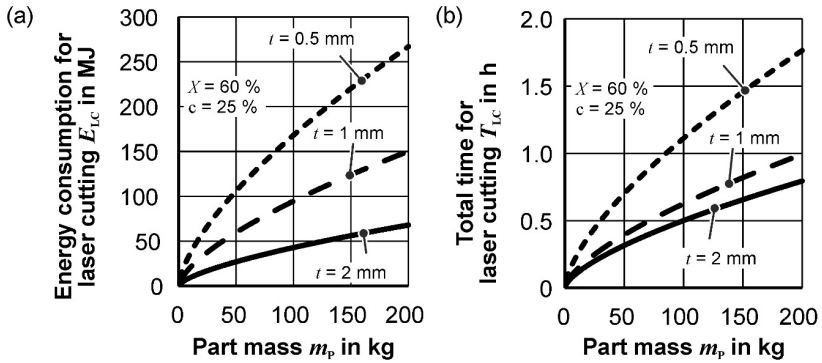

Figure 7.5: (a) Total energy consumption (E_{TC}) for cutting, (b) total cutting time (T_{LC})

Two main production methods for fabricating the powder for laser metal deposition are gas atomization and plasma atomization (Popov et al., 2021). There are different methods and values for calculating the energy required for powder production. However, in this study, the powder production energy is selected based on the calculation from Yule and Dunkley (1994). For gas atomization, 24.48 MJ is required to manufacture one kilogram powder. It is assumed that for the hybrid method, the mass of the sum of the stair step volumes ($m_{\mathrm{Step}} = \rho \cdot \sum_{i=1}^{n-1} V_i$), is 1 % of the scrap mass (m_S) i.e. the required powder by LMD is 1 % of m_S. Therefore, the energy required for fabrication of the powder for LMD is:

$$E_{\mathrm{Powder}}^{\mathrm{Hybrid}} = 24.48 \left[\frac{\mathrm{MJ}}{\mathrm{kg}}\right] \cdot (0.01 \cdot m_{\mathrm{s}}) = 0.2448 \left[\frac{\mathrm{MJ}}{\mathrm{kg}}\right] \left(\frac{1-X}{X}\right) \cdot m_{\mathrm{P}}. \qquad (7.8)$$

A detailed evaluation of the energy consumed during laser deposition with Lasertec 65 3D was carried out by Wippermann et al. (2020), and the calculated result shows an energy consumption of 76.11 MJ/kg during laser deposition (without any post-processing) with the given process parameters. Based on that, the consumed energy during the deposition of the stair steps is:

$$E_{\mathrm{LPA}}^{\mathrm{Hybrid}} = 76.11 \left[\frac{\mathrm{MJ}}{\mathrm{kg}}\right] \cdot (0.01 \cdot m_{\mathrm{s}}) = 0.7611 \left[\frac{\mathrm{MJ}}{\mathrm{kg}}\right] \cdot \left(\frac{1-X}{X}\right) \cdot m_{\mathrm{P}}. \qquad (7.9)$$

The deposition time depends on the feed rate (f) and tool travel path (L_T). The total tool travel path (L_T) defines the distance the tool needs to go through. It can be defined as the cutting length (C_L) and with the corresponding hatching distance (h_d). In this study, for further analysis, it is considered that the part is manufactured out of a constant sheet thickness of 1 mm. Therefore, the relation between the tool travel path (L_T) and the cutting length (C_L) is equal to:

$$L_{\mathrm{T}} = \begin{cases} \dfrac{C_{\mathrm{L}}}{h_d}, & h_d < 1\ \mathrm{mm} \\ C_{\mathrm{L}}, & h_d = 1\ \mathrm{mm} \\ C_{\mathrm{L}} \cdot h_d, & h_d > 1\ \mathrm{mm} \end{cases} \tag{7.10}$$

In the rest of this study, the tool travel path is equal to the cutting length, i.e., $L_{\mathrm{T}} = C_{\mathrm{L}}$. Therefore, the post-processing time for all three processes can be written as follows:

$$T_{\mathrm{PP}}^{\mathrm{Hybrid}} = \frac{C_{\mathrm{L}}}{f}. \tag{7.11}$$

For calculation of the total post-processing energy ($E_{\mathrm{PP}}^{\mathrm{Hybrid}}$) it is assumed that the tool (ball or laser) need to go through all cutting lengths (C_{L}) with the required energy consumption ($E_{\mathrm{rq.}}$).

$$E_{\mathrm{PP}}^{\mathrm{Hybrid}} = T_{\mathrm{PP}}^{\mathrm{Hybrid}} \cdot E_{\mathrm{rq.}}. \tag{7.12}$$

Since the energy consumption for each machine would be different here, the energy required for machines' movement is neglected. Therefore, the energy for laser polishing is equal to the laser power $E_{\mathrm{Sp.}}^{\mathrm{LP}} = P_{\mathrm{LP}}$. For the ball burnishing, the energy consumption of the hydraulic aggregator is used for the calculations. The hydraulic aggregator HGP6.5 400V from Ecoroll company has a consumption of $E_{\mathrm{rq}}^{\mathrm{BB}}$ = 3 kW.

Milling is conventionally applied within two different steps: rough milling and finishing. In rough milling, the depth of cut and feed rate is high. Therefore, the shape accuracy and surface roughness do not fulfill the final quality. In the finishing step, the depth of cut and feed rate of the tool is low, and the rotational speed of the tool is much higher than rough milling. Since the specific energy consumption for rough milling is significantly lower than finishing, two different values based on Zhao et al. (2018) are used to calculate the milling energy consumption. The specific energy consumption per kg (SEC) for finishing milling is $SEC_{\mathrm{Finishing}}$ = 5.791 MJ/kg; for rough milling, it is SEC_{Rough} = 0.848 MJ/kg. The feed rates are also different, which affects the production time. In the hybrid additive laminated tooling method, it is considered that 20 % of the deposited powder mass needs to be milled in the case of milling as the post-processing method (**Fig. 7.6**).

By that, the specific energy for post-processing energy ($E_{\mathrm{PP}}^{\mathrm{Hybrid}}$) by milling is:

$$E_{\mathrm{PP}}^{\mathrm{Hybrid}} = 0.01 \cdot 0.02 \cdot SEC_{\mathrm{Finishing}} \cdot m_{\mathrm{S}} = 0.001158 \left[\frac{\mathrm{MJ}}{\mathrm{kg}}\right] \cdot \left(\frac{1-X}{X}\right) \cdot m_{\mathrm{P}}. \tag{7.13}$$

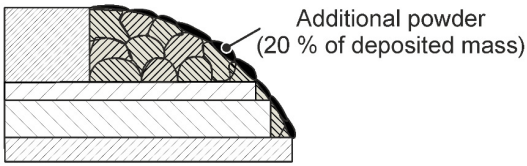

Figure 7.6: Schematic of additional powder in hybrid additive laminated for milling

Calculating the milling time requires different calculation methods. In which the following parameters, radial depth of cut (a_e) and axial depth of cut (a_p), both in mm beside the feed rate (f) need to be defined. These three parameters are produced by material removal rate (Q) with a unit of mm^3/h, mathematically shown in **Eq. (7.14)**.

$$Q[\mathrm{mm^3/h}] = f \cdot a_\mathrm{p} \cdot a_\mathrm{e}\,. \tag{7.14}$$

The material removal rate can be transformed as **Eq. (7.15)** by considering the density (ρ).

$$Q_{\mathrm{Finishing}}^{\mathrm{Hybrid}}[\mathrm{kg/h}] = \rho \cdot f \cdot a_\mathrm{p} \cdot a_\mathrm{e}\,, \tag{7.15}$$

where the unit of material removal rate ($Q_{\mathrm{Finishing}}^{\mathrm{Hybrid}}$) will be in kg/h.

The time of milling for the hybrid additive laminated tool considering the 1 % of mass removal of scrap mass can be calculated as:

$$T_{\mathrm{Milling}}^{\mathrm{Hybrid}} = \frac{Q_{\mathrm{Finishing}}^{\mathrm{Hybrid}}}{0.01 \cdot m_\mathrm{s}} = \frac{\rho \cdot f \cdot a_\mathrm{p}^{\mathrm{Finishing}} \cdot a_\mathrm{e}^{\mathrm{Finishing}}}{0.01 \cdot (\frac{1-X}{X}) \cdot m_\mathrm{P}}. \tag{7.16}$$

7.2 LMD plus milling

In the deposition of the whole part with laser metal deposition (LMD), powder waste during the process is not negligible. In addition, the subtractive post-processing method is considered, and 20 % of the total part mass is added to calculate the required powder. The same values are used for hybrid metal deposition to calculate the energy for the production of powder and the required energy for deposition. Considering the necessary powder, the total energy for powder production is:

$$E_{\mathrm{Powder}}^{\mathrm{LMD+Milling}} = 24.48\left[\frac{\mathrm{MJ}}{\mathrm{kg}}\right] \cdot (0.2 \cdot m_\mathrm{P}) = 4.896\left[\frac{\mathrm{MJ}}{\mathrm{kg}}\right] \cdot m_\mathrm{P}, \tag{7.17}$$

Since during the positioning for the laser head, the laser is off, therefore only the net mass of the part is considered for the calculation of the deposition energy during LMD with Lasertec 65 3D, which yields as:

$$E_{\mathrm{LPA}}^{\mathrm{LMD+Milling}} = 76.11 \left[\frac{\mathrm{MJ}}{\mathrm{kg}}\right] \cdot m_{\mathrm{P}}. \tag{7.18}$$

For post-processing, only 1 % of the part mass (m_{P}) is considered to be fine-milled:

$$E_{\mathrm{PP}}^{\mathrm{LMD+Milling}} = 0.01 \cdot SEC_{\mathrm{Finishing}} \cdot m_{\mathrm{P.}} = 0.0579 \left[\frac{\mathrm{MJ}}{\mathrm{kg}}\right] \cdot m_{\mathrm{P}}. \tag{7.19}$$

Like the hybrid additive laminated method, the feed rate during the deposition is 1000 mm/min.

For calculation of the manufacturing time of LMD plus milling, the same procedure can be used as for the hybrid additive laminated method, and it yields:

$$T_{\mathrm{Milling}}^{\mathrm{Hybrid}} = \frac{Q_{\mathrm{Finishing}}^{\mathrm{Hybrid}}}{0.01 \cdot m_{\mathrm{P}}} = \frac{\rho \cdot f \cdot a_{\mathrm{p}}^{\mathrm{Finishing}} \cdot a_{\mathrm{e}}^{\mathrm{Finishing}}}{0.01 \cdot m_{\mathrm{P}}}. \tag{7.20}$$

7.3 Conventional method (milling plus hardening)

In the conventional method, the final geometry is manufactured by subtractive processes such as milling or turning. In this study, the milling process is used for the calculation. Guminski et al. (2019) showed that the demanded energy for the fabrication of bulk material is E_{Bulk} = 17.73 MJ/kg, which means the total required energy is for bulk material considering the part mass:

$$E_{\mathrm{Bulk}} = 17.73 \left[\frac{\mathrm{MJ}}{\mathrm{kg}}\right] \cdot (m_{\mathrm{P}} + m_{\mathrm{s}}) = \frac{17.73}{X} \left[\frac{\mathrm{MJ}}{\mathrm{kg}}\right] \cdot m_{\mathrm{P}}. \tag{7.21}$$

For the conventional method, it is assumed that 99 % of the scrap mass is rough milled and only 1 % of the scrap mass is finishing mill. Therefore, by considering the specific energy consumption of finishing milling 0.848 MJ/kg and for rough milling 5.791 MJ/kg, the total machining energy in conventional equals:

$$E_{\mathrm{M}}^{\mathrm{Conv.}} = \left(0.99 \cdot SEC_{\mathrm{Rough}} + 0.01 \cdot SEC_{\mathrm{Finishing}}\right) \cdot m_{\mathrm{P}} = 0.8974 \left[\frac{\mathrm{MJ}}{\mathrm{kg}}\right] \cdot m_{\mathrm{P}}. \tag{7.22}$$

The energy consumption for the hardening process is significantly dependent on the part's geometry, the type of hardening, and the goal temperature (**Fig. 7.7**). In this study, hardening in the N 120/85 HA furnace with a power consumption of 13.6 kW from Nabertherm GmbH, which is available at IUL, is selected for energy and time calculations. It is assumed that the thickness of 80 mm by the maximum temperature of the furnace, 850 °C, needs to be heated. According to Fig. 7.7, the heating time is one hour. Considering the assumed square shape (Fig. 7.2) and the length-to-thickness ratio of 25 %, the length of the square would be 320 mm, and considering the density of steel, the total weight of the sample is about 64.7 kg.

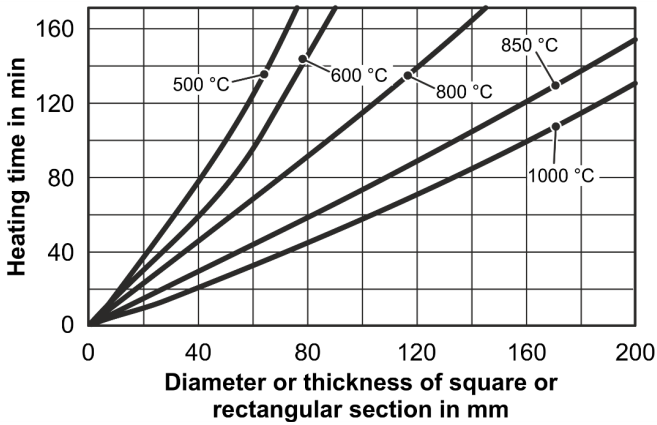

Figure 7.7: Heating time in air respectively under shielding gas (Spur and Zoch, 2015)

By considering that the furnace needs to use 50 % of the maximum energy for the heating up phase for one hour, the specific energy of the furnace can be calculated as:

$$SEC_{\text{Furnace}} = \frac{(13.6 + 6.8)\text{kWh}}{64.7\ \text{kg}} \cdot 3.6 \frac{\text{MJ}}{\text{kWh}} = 1.14 \frac{\text{MJ}}{\text{kg}}. \tag{7.23}$$

The hardening energy is:

$$E_{\text{H}} = SEC_{\text{Furnace}} \cdot m_{\text{P.}} = 1.14 \left[\frac{\text{MJ}}{\text{kg}}\right] \cdot m_{\text{P}}\,. \tag{7.24}$$

The hardening time is equal to:

$$T_{\text{H}} = \frac{2\ \text{h}}{64.7\ \text{kg}} \cdot m_{\text{P.}} = 0.031 \left[\frac{\text{h}}{\text{kg}}\right] \cdot m_{\text{P}}\,. \tag{7.25}$$

As mentioned earlier, since there is no general and unique equation for hardening, the suggested values are based on assumptions.

7.4 Comparison between the different processes

The values for different process parameters are selected as a case study to compare all possible processes, as shown in **Table 7.2**. The parameters are chosen based on experimental work.

The energy consumption for all processes is calculated (**Fig. 7.8**) by considering the process parameters presented in Table 7.2. The results show that the maximum energy consumption is by fully LMD parts plus milling followed by hybrid additive laminated tooling and finally conventional. However, there is less difference between the hybrid and the conventional methods.

Table 7.2: Process parameters for post-processing

Process	Laser polishing	Ball burnishing	Milling	
			Rough	Finishing
Feed rate f in mm/min	1000	900	600	200
Laser power P_L in W	1000	-	-	-
Radial depth of cut a_e in mm	-	-	25	25
Axial depth of cut a_p in mm	-	-	2	0.25
Track distance h_d in mm	1	1	-	-

Since the hybrid method's post-processing fraction from total energy consumption is very small, the difference between them is infinitesimal. In addition, the energy consumption by post-processing in the hybrid method depends on the process parameters.

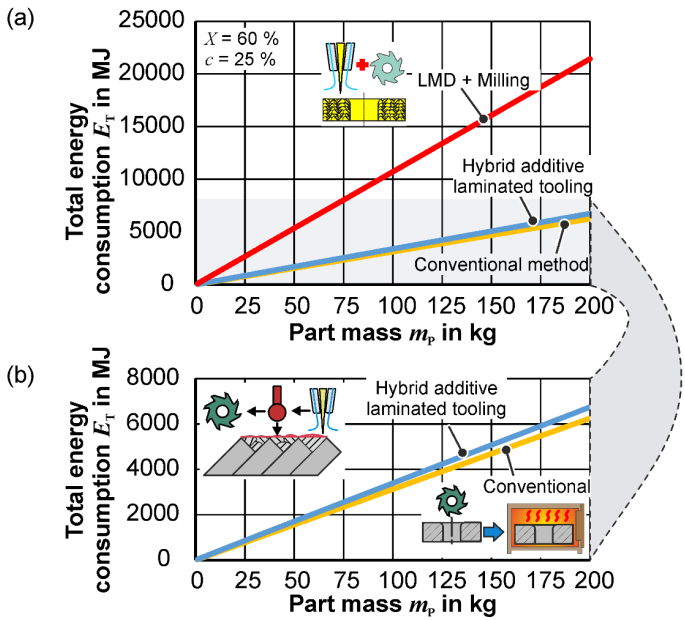

Figure 7.8: Total energy consumption E_T for three process routes (a) with LMD plus milling, (b) without fully LMD plus milling (without red curve)

It should also be noted that in the conventional method, the hardening energy is a function of the type of the hardening method and the furnace configuration. Therefore, the total energy consumption of the conventional method could be higher than the hybrid method.

The calculated manufacturing time for all three processes is shown in **Fig. 7.9a**. Like energy consumption results, the fully deposited parts demand much more production time than the two methods. The main reason is the high volume needed to deposit to generate the part. The hybrid and the conventional methods are faster since the main body of the part is already pre-manufactured (as sheet or bulk material). Even without considering the common transportation time of parts to hardening, the conventional method requires a higher production time than the hybrid additive laminated tooling method (**Fig. 7.9b**).

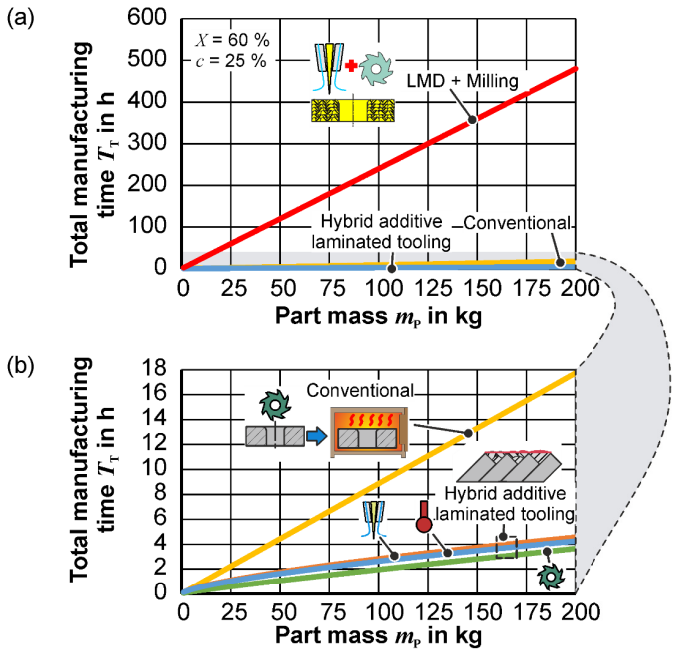

Figure 7.9: Total manufacturing time T_T (a) with LMD plus milling, (b) without fully LMD plus milling (without red curve)

Milling is faster than the other two post-processing methods (Fig. 7.9b). Based on the calculations, ball burnishing and laser polishing have slight differences. However, the production time is highly dependent on the process parameters such as feed rate, track distance, and tool diameter, i.e., by selecting different process parameters, the production time order would vary.

Laser polishing has unique advantages among the three different post-processing methods in hybrid additive laminated tooling. The laser polishing saves the cost of new tooling as well as programming time. In addition, because laser polishing is a non-contact process, tool wear is very low. The final superiority of this method is the

treatment of the surface within the focal distance. It allows the laser to treat the limited access areas.

The initial investment cost for the three processes is shown in **Fig. 7.10**. The hybrid process requires either a milling or ball burnishing tool in addition to the deposition and laser cutting machine. The initial investment cost calculations assume that the hybrid Lasertec 65 3D is used for the hybrid process. In this machine, milling and LMD are integrated. A laser cutting machine is required for the hybrid process, with laser polishing as post-processing besides the deposition. The Lasertec 65 DED machine from company DMG MORI can be selected. For ball burnishing, an additional ball burnishing aggregator and tool is required. The furnace costs for conventional methods can vary based on the chamber's inner geometry and heating type. Based on company Nabertherm's inquiry, it could vary from 100 k€ to 400 k€.

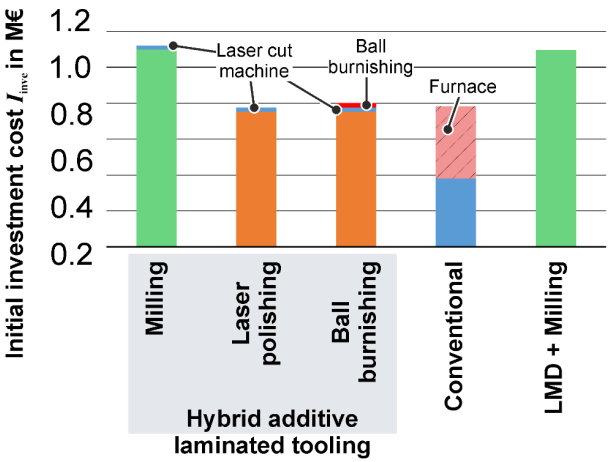

Figure 7.10: Initial investment cost for all three process routes

7.5 Determination of optimal sheet combination

Sheet lamination can manufacture parts with a combination of distinctive layer thicknesses. For instance, in the case of manufacturing the parts with different thicknesses, here 0.5, 1, and 2 mm sheets, the number of possible sheet combinations with these three sheet thicknesses multiply exponentially by an increasing radius (**Fig. 7.11**). The precise selection of combination is a multi-objective function relying on the demanded tool strength, manufacturing energy consumption, tooling cost, and induction of functional elements, e.g., cooling/heating channels or sensors. In this study, energy consumption and manufacturing time form the economic point of view and are two main criteria for optimizing the number of possibilities.

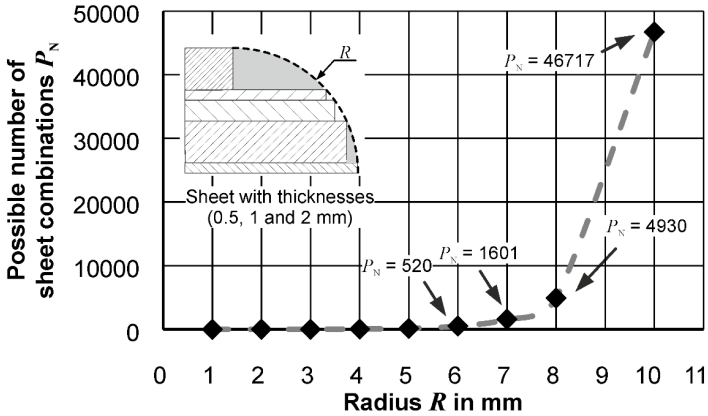

Figure 7.11: Possible number of the sheet combinations (P_N) for different radii

For optimizing the sheet combinations, the following criteria are considered:

- The normalized laser cutting time ($T_{\mathrm{LC}}^{\mathrm{N}}$).
- The normalized energy consumption for the laser cutting ($E_{\mathrm{LC}}^{\mathrm{N}}$).
- The normalized energy of production of metal powder and demanded energy for laser metal deposition ($E_{\mathrm{Powder}}^{\mathrm{N}} + E_{\mathrm{LMD}}^{\mathrm{N}}$).

The cutting time and energy consumption are preferred to be kept as low as feasible. These criteria are applied for three radii of 6, 5, and 4 mm for each individual sheet combination. The stair step areas for each combination are calculated based on Eq. (5.10), and each combination's corresponding required powder and energy for deposition are calculated. The outcomes are plotted in **Fig. 7.12**. For all three radii (6, 5, and 4 mm), the break-even point is around 0.33 to 0.35. By considering the break-even point's value, the sheet combinations are reduced. The total number for the radius of 4 mm decreases from 55 to 4, for the radius of 5 mm from 169 to 13, and finally, for the 6 mm radius from 520 to 24 combinations. The numbers of the layers are in all three radii, the same as the nominal radius, i.e., for the 6 mm radius, all 24 combinations have six layers. For 5 mm radius, all 13 combinations have five layers, and finally, for a 4 mm radius, all combinations have four layers. The break-even point value (0.33 to 0.35) is also confirmed for the radius of 10 mm. Considering the break-even point, the number of combinations is reduced to 1250 from 46717. All 1250 combinations also have ten or nine layers.

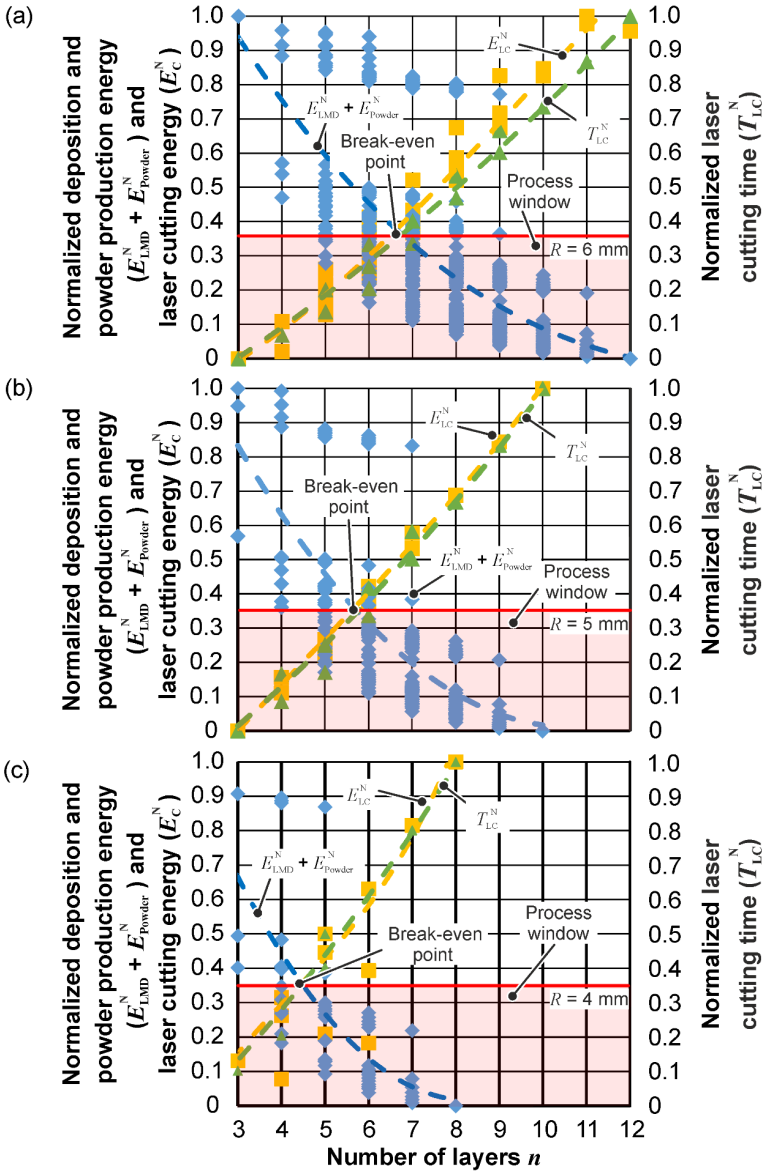

Figure 7.12: Determination of break-even point for tool radius of (a) 6 mm (b) 5 mm (c) 4 mm

7.6 Summary

The hybrid additive layer tool's energy consumption and manufacturing time are systematically evaluated and compared with the fully deposited part using LMD plus milling (as a post-processing method) and the conventional method. It is shown that the hybrid method is at least 29 % faster than the conventional method and more than 100 % faster than the LMD plus milling strategy for the same final part mass. Compared to the conventional manufacturing approach, which typically consists of milling followed by hardening, it is shown that the energy consumption is almost the same for simple geometries (a square with a hole in the center). However, complex shapes can be produced quickly using the hybrid additive laminating process, as laminating provides high flexibility in producing complex geometries.

Among other post-processing methods, laser polishing provides a suitable tool surface roughness without additional tooling and with reduced programming costs. With milling and ball burnishing, tool wear is also a challenge, in addition to additional tooling costs. Laser polishing is non-contact, and treating the tool surface at the focal point provides more room to work in tight areas and increases flexibility not available with other finishing methods.

Since the number of possible sheet combinations in sheet lamination is high, an optimized method based on economic evaluation is developed to reduce the number of possible combinations. It is concluded that 0.33 to 0.35 is the break-even point for normalized manufacturing time and deposition energy. This criterion drastically reduces the number of sheet combinations, e.g., for a 10 mm radius out of 0.5, 1.0, and 2.0 mm thickness, the number of combinations can be reduced up to 97 %, which helps to select the more energy-efficient sheet combination.

8 Conclusion and outlook

The fundamentals of a new manufacturing process, so-called hybrid additive laminated tooling for deep drawing dies, are investigated. The procedure of designing and manufacturing such forming tools is presented. The following scientific questions are answered in this study.

What are the considerations in the tooling design process?

The tool design starts with the selection of the combination of the proper sheet. The selected sheets should not plastify during the process. Therefore, a semi-analytical model based on beam theory and FEM simulation is developed to determine the proper sheet combination. It is concluded that due to stress saturation in a large area of the stacked-beam, low-strength sheets can be used near the laminated die surface, and only high-strength materials are required for the tool's bottom side. It offers the possibility of using lower-cost sheet metal for tooling, thus reducing tooling costs.

What are the characteristic mechanical limitations of the hybrid process?

The developed two-step filling strategy for reducing the stair-step effect, bonding, and filling reduces shape inaccuracy. It is concluded that the higher laser power and low powder mass flow also deliver a stronger joining of sheets and better surface roughness. However, the thickness of the sheets by selecting the process parameters during the deposition needs to be considered, where very high laser power with low feed rate and mass flow leads to over-melting the thin sheets.

Preheating the tool sheets to 100 °C during the deposition of 316L-Si powder can reduce the residual tensile stress, but it increases the surface roughness parameters. Therefore, the preheating can be neglected, which reduces the tool cost.

The tribological study shows the necessity of post-processing the deposited surfaces to obtain surface properties comparable to those of conventionally manufactured tools.

The various post-processing methods show that the surface roughness and hardness of the finished components are highly dependent on the process parameters. Ball burnishing not only improves surface roughness but also increases hardness. The disadvantage of laser polishing, i.e. the reduction in hardness, can be compensated by changing the strategy so that the hardness can not only be reduced but even increased.

In addition to simple axisymmetric deep-drawing dies, hybrid additive laminated tooling allows the production of complex shapes, i.e., with 3D surfaces, in a short time.

The hybrid method can be used for rapid prototyping and is also suitable for mass production to a certain extent, as proven by wear experiments.

What is the CO_2-footprint of this process?

Compared with the conventional process route (milling followed by hardening) and a fully deposited part using LMD plus milling, the hybrid additive laminated tool is more economical and faster. The low energy consumption of this method by eliminating the energy-intensive hardening process offers the possibility of producing complex shapes with lower CO_2 emissions and greener manufacturing. By determining the energy consumption and manufacturing criteria for selecting the proper sheet combination, the hybrid process can be optimized to reduce the CO_2 footprint. Using laser polishing-hardening to smooth the surface by saving additional programming and computing time compared to other post-processing methods offers more resource savings. The ability to use lower-strength sheets in hybrid additive-laminated tooling is another optimization source for this process, since high-strength sheets consume more energy than lower-strength sheets.

Outlook

The hybrid additive laminated tooling method is highly flexible and can be combined with other processes to increase the design and manufacturing complexity. The following three possible methods are presented as extensions of this method.

8.1 Smart tooling

Sheet lamination offers the possibility of placing various sensors or functional elements, in addition to inserting complex heating cartridges and cooling channels. However, the main challenge with conventional methods for reducing stair-step areas is the need for hardening. Conventional hardening methods require entire parts to be placed in an oven and heated to a specific temperature. Since force sensors, and in some cases temperature sensors, have an allowable operating temperature that is much lower than the hardening temperature, it is not possible or limited to place the sensors using conventional methods. Since the hybrid method does not require a hardening step, it allows the sensors to be used in sheet metal laminated tools in a short time. It also allows making effective contact areas of the dies with different materials (powders) with different heat transfer coefficients, hardening, and wear behavior. An example of such a die is shown in **Fig. 8.1**. In this example, one side can be heated to a specific temperature by moldable heating cartridges, while complex cooling channels can cool the other side of the die. The temperature sensors can monitor the temperature in between, and forces can be measured during the process.

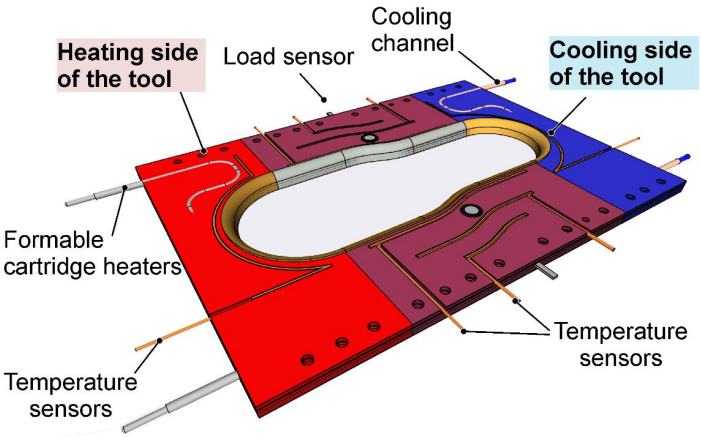

Figure 8.1: Smart tooling concept for deep drawing die (the cover sheets are removed for a better understanding of the channels and sensors' positions)

8.2 Cold forging dies

The concept of laminated tooling can also be applied to manufacturing cold forging dies. Cold forging dies are subjected to high stress from process forces, and hardening is an essential step in tool manufacturing. It results in a long production time. The dies produced by the hybrid method offer the possibility of quickly manufacturing the cold forging dies and the possibility of customizing the tool according to the requirements. An example of a hybrid cold forging die is shown in **Fig. 8.2**.

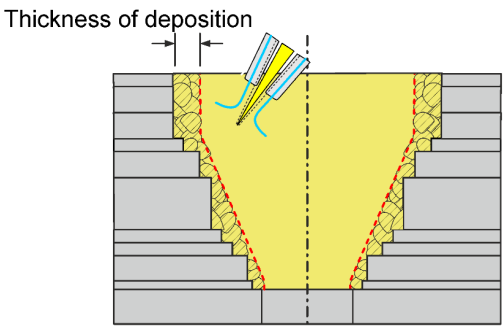

Figure 8.2: Cold forging die manufactured by hybrid laminated tooling method

The thickness can be varied easily per deposition layer and helps distribute the process stresses. Since the tool surface is manufactured from hard powder, e.g., Ferro55, there is no need for subsequent hardening.

8.3 Workpieces

In addition to tooling, sheet laminating allows for the production of finished parts with complex shapes. Extruded profiles can be produced in less time and without additional costly tooling. For example, a bulk extruded part with internal cooling/heating channels can be produced by sheet lamination. The use of sheet lamination can eliminate the need for deep-hole drilling of channels. LMD and laser polishing can improve the step effect and surface roughness (**Fig. 8.3**).

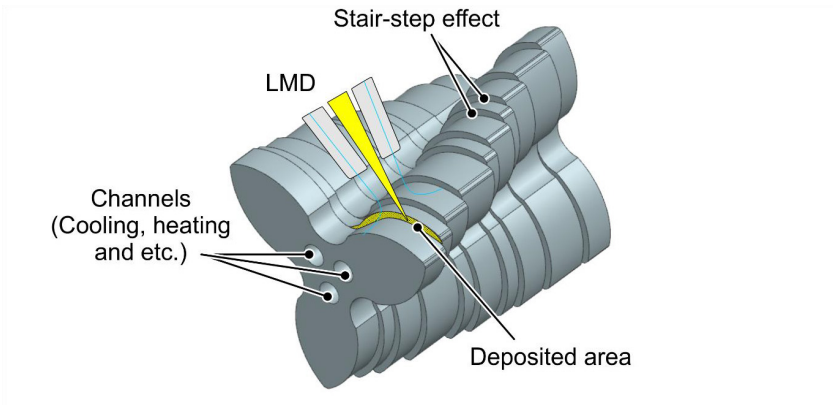

Figure 8.3: Cold forging die manufactured by hybrid laminated tooling method

8.4 Hot stamping punches

Hot stamping punches require the blanks to be cooled at a minimum of 27 K/min. Cooling is provided by the hot stamping die. Therefore, the main challenge in designing a hot stamping die is to create complex cooling channels near the surface. As mentioned in Chapter 2, one possibility is to manufacture the entire punch by laser metal deposition. The complete manufacture of complex parts with LMD offers high flexibility for complex geometries (here, cooling channels). Still, the energy consumption and production time are outside the concept of rapid tooling (Chapter 7). One possible method to reduce energy consumption and production time is to use sheet metal lamination to fill the flat areas in the die. In the proposed method, the wall of the cooling channels could first be produced by LMD, as shown in **Fig. 8.4a**.

Then, the sheets could be stacked with defined cuts (based on the width of the wall in each section) and welded to the wall of the cooling channels by LMD (**Fig. 8.4b** and **c**).

Since the sharp edge of the cooling channel prevents unwanted positioning of the top sheet, the last layer can be coated entirely by LMD to improve the surface roughness and add a hard layer on the last layer (**Fig. 8.4d**). In addition, the stair-step effect can be reduced by LMD. The appropriate post-processing (milling, ball burnishing, or laser polishing) could be applied to the tool contact surface to improve the surface roughness (**Fig. 8.4e** and **f**).

The other major advantage of using the hybrid method to produce complex shapes compared to other additive manufacturing processes, such as powder bed fusion, is the ability to produce parts on a large scale (Rosenthal et al., 2022).

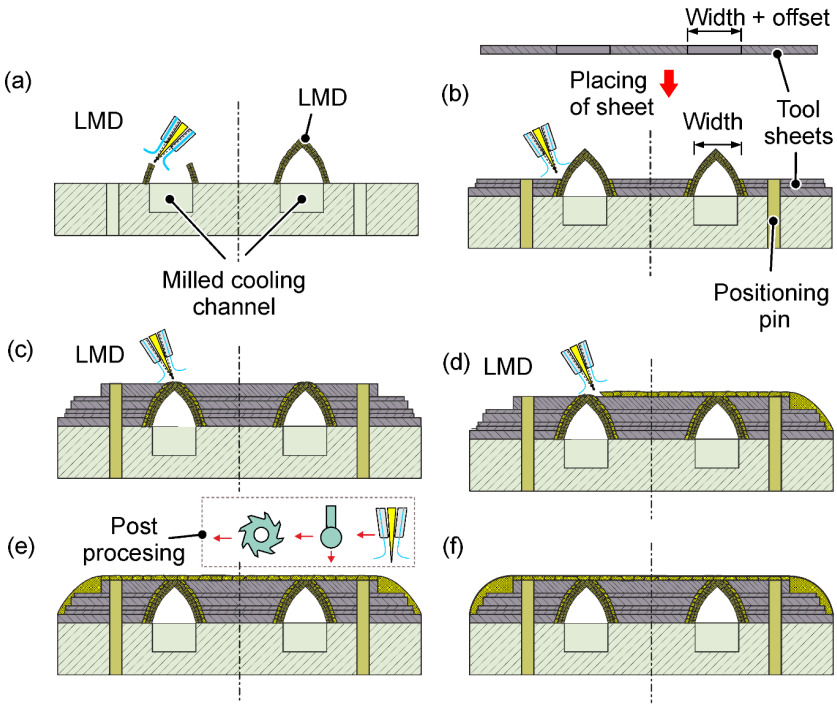

Figure 8.4: (a) Manufacturing the complex cooling channel by LMD, (b) placing the cut sheets and joining by LMD with the wall of the cooling channel, (c) replacing all sheets, (d) reducing the stair-step effect by LMD, (e) post-processing, (f) hybrid hot stamping punch

References

Adams, T.E., Härtel, S., Hälsig, A., Awiszus, B., Mayr, P., 2020. WeldForming: a new inline process combination to improve weld seam properties. Weld World, vol. 30, pp. 1969.

Ahn, D.G., 2021. Directed Energy Deposition (DED) Process: State of the Art. International Journal of Precision Engineering and Manufacturing-Green Technology, vol. 8, pp. 703-742.

Alimardani, M., Fallah, V., Khajepour, A., Toyserkani, E., 2010. The effect of localized dynamic surface preheating in laser cladding of Stellite 1. Surface and Coat-ings Technology, vol. 204(23), pp. 3911-3919.

Altenkirch, J., Steuwer, A., Withers, P.J., Williams, S.W., Poad, M., Wen, S.W., 2009. Residual stress engineering in friction stir welds by roller tensioning. Science and Technology of Welding and Joining, vol. 14(2), pp. 185-192.

Araghi, B.T., Manco, G.L., Bambach, M., Hirt, G., 2009. Investigation into a new hybrid forming process: Incremental sheet forming combined with stretch forming. CIRP Annals, vol. 58(1), pp. 225-228.

Aspinwall, D.K., Dewes, R.C., Burrows, J.M., Paul, M.A., Davies, B.J., 2001. Hybrid High Speed Machining (HSM): System Design and Experimental Results for Grinding/HSM and EDM/HSM. CIRP Annals, vol. 50(1), pp.145-148.

Atamert, S., Bhadeshia, H.K.D.H., 1989. Comparison of the microstructures and abrasive wear properties of stellite hardfacing alloys deposited by arc welding and laser cladding. MTA, vol. 20, pp. 1037-1054.

Baratta, F.I., 1981. When is a Beam a Plate?. Journal of American Ceramic Society, vol. 64(5), pp. 6.

Bareisis, J., 2004. Design and Stress State of Tensions in Multilayer Bars. Journal of Composite Materials, vol. 38(5), pp. 389-397

Bareisis, J., 2006. Stiffness and Strength of Multilayer Beams. Journal of Composite Materials, vol. 40(6), pp. 515-531.

Barragan De Los Rios, G.A., Ferreira, R., Mariani, F.E., Da Silva, E.J., Coelho, R.T., 2023. Study of the surface roughness of a remanufactured bimetallic AISI 1045 and 316L SS part obtained by hybrid manufacturing (DED/HSM International Journal of Advanced Manufacturing Technology, vol. 124, pp. 3185-3199.

Bax, B., Rajput, R., Kellet, R., Reisacher, M., 2018. Systematic evaluation of process parameter maps for laser cladding and directed energy deposition. Additive Manufacturing, vol. 21, pp. 487-494.

Bhaduri, D., Penchev, P., Batal, A., Dimov, S., Soo, S.L, Sten, S., Harrysson, U., Zhang, Z., Dong, H., 2017. Laser polishing of 3D printed mesoscale components. Applied Surface Science, vol. 405, pp. 29-46.

Boljanovic, V., 2004. Sheet metal forming processes and die design. Industrial Press. New York.

Bragg, W.H., Bragg, W.L., 1913. The reflection of X-rays by crystals. Proc. R. Soc. Lond. A, vol. 88(605), pp. 428-438.

Bryden, B.G., Pashby, I.R., 2001. Hot platen brazing to produce laminated steel tooling. Journal of Materials Processing Technology, vol. 110(2), pp. 206-210.

Bryden, B.G., Pashby, I.R., Wimpenny, D.I., Adams, C., 2000. Laminated steel tooling in the aerospace industry. Materials & Design, vol. 21(4), pp. 403-408.

Cao, J., Brinksmeier, E., Fu, M., Gao, R.X., Liang, B., Merklein, M., Schmidt, M., Yanagimoto, J., 2019. Manufacturing of advanced smart tooling for metal forming. CIRP Annals, vol. 68(2), pp. 605-628.

Chatterjee, S., Shariff, S.M., Datta Majumdar, J., Roy Choudhury, A., 2008. Development of nano-structured Al2O3-TiB2-TiN coatings by combined SHS and laser surface alloying. International Journal of Advanced Manufacturing Technology, vol. 38, pp. 938-943.

Clevenger, W.S., Cohen, J.S., Cohen, S.G., 1954. Laminated die form and method of producing same. US Patent, US2679172A, priority date: 16.03.1951.

Colegrove, P.A, Donoghue, J., Martina, F., Gu, J., Prangnell, P., Hönnige, J., 2017. Application of bulk deformation methods for microstructural and material property improvement and residual stress and distortion control in additively manufactured components. Scripta Materialia, vol. 135, pp. 111-118.

Cortina, M., Arrizubieta, J., Calleja, A., Ukar, E., Alberdi, A., 2018. Case Study to Illustrate the Potential of Conformal Cooling Channels for Hot Stamping Dies Manufactured Using Hybrid Process of Laser Metal Deposition (LMD) and Milling. Metals, vol. 8(2), pp. 102.

Costa, L., Felde, I., Réti, T., Kálazi, Z., Colaço, R., Vilar, R., Verő, B., 2003. A Simplified Semi-Empirical Method to Select the Processing Parameters for Laser Clad Coatings. MSF, vol. 414-415, pp. 385-394.

Coules, H.E, Colegrove, P., Cozzolino, L.D., Wen, S.W., Ganguly, S., Pirling, T., 2012. Effect of high pressure rolling on weld-induced residual stresses. Science and Technology of Welding and Joining, vol. 17(5), pp. 394-401.

Craig, O., Bois-Brochu, A., Plucknett, K., 2021. Geometry and surface characteristics of H13 hot-work tool steel manufactured using laser-directed energy deposition. Int J Adv Manuf Technol, vol. 116, pp. 699-718.

Cunningham, C.R., Flynn, J.M., Shokrani, A., Dhokia, V., Newman, S.T., 2018. Invited review article: Strategies and processes for high quality wire arc additive manufacturing. Additive Manufacturing, vol. 22, pp. 672-686.

Dadbakhsh, S., Hao, L., Kong, C.Y., 2010. Surface finish improvement of LMD samples using laser polishing. Virtual and Physical Prototyping, vol. 5(4), pp. 215-221.

Dandekar, C.R., Shin, Y.C., Barnes, J., 2010. Machinability improvement of titanium alloy (Ti-6Al-4V) via LAM and hybrid machining. International Journal of Ma-chine Tools and Manufacture, vol. 50(2), pp. 174-182.

Dankert, J., Dankert, H., 2013. Technische Mechanik. Springer Fachmedien Wiesbaden. Wiesbaden.

Dickens, P.M., 1997. Principles of design for laminated tooling. International Journal of Production Research, vol. 35(5), pp. 1349-1357.

DIN 50125, 2016. Prüfung metallischer Werkstoffe - Zugproben. Berlin. Beuth Verlag GmbH.

DIN 8584-1, 2003. Fertigungsverfahren Zugdruckumformen - Teil 1: Allgemeines; Einordnung, Unterteilung, Begriffe. Berlin. Beuth Verlag GmbH.

DIN EN 10149-2, 2013. Warmgewalzte Flacherzeugnisse aus Stählen mit hoher Streckgrenze zum Kaltumformen - Teil 2: Technische Lieferbedingungen für thermomechanisch gewalzte Stähle. Deutschland. Beuth Verlag GmbH.

DIN EN 10268, 2013. Kaltgewalzte Flacherzeugnisse aus Stählen mit hoher Streckgrenze zum Kaltumformen. Deutschland. Beuth Verlag GmbH.

DIN EN ISO 25178, 2016. Geometrische Produktspezifikation(GPS) - Oberflächenbeschaffenheit: Flächenhaft - Teil 1: Angabe von Oberflächenbeschaffenheit. Berlin. Beuth Verlag GmbH.

DIN EN ISO 4287, 2010. Geometrische Produktspezifikation (GPS) - Oberflächenbeschaffenheit: Tastschnittverfahren - Benennungen, Definitionen und Kenngrößen der Oberflächenbeschaffenheit. Berlin. Beuth Verlag GmbH.

DIN EN ISO 6892, 2020. Metallische Werkstoffe - Zugversuch - Teil 1: Prüfverfahren bei Raumtemperatur. Berlin. Beuth Verlag GmbH.

DIN EN ISO/ASTM 52900, 2022. Additive Fertigung - Grundlagen - Terminologie. Berlin. Beuth Verlag GmbH.

Ding, C., Cui, X., Jiao, J., Zhu, P., 2018. Effects of Substrate Preheating Temperatures on the Microstructure, Properties, and Residual Stress of 12CrNi2 Prepared by Laser Cladding Deposition Technique. Materials (Basel, Switzerland), vol. 11(12), pp. 2401.

Ding, D., Pan, Z., Cuiuri, D., Li, H., 2015. Wire-feed additive manufacturing of metal components: technologies, developments and future interests. International Journal of Advanced Manufacturing Technology, vol. 81, pp. 465-481.

Doege, E., Behrens, B.A., 2010. Handbuch Umformtechnik. Grundlagen, Technologien, Maschinen Springer Berlin Heidelberg. Berlin, Heidelberg.

Duflou, J.R, Callebaut, B., Verbert, J., Baerdemaeker, H. de, 2007. Laser Assisted Incremental Forming: Formability and Accuracy Improvement. CIRP Annals, vol. 56(1), pp. 273-276.

Dutta, B., Palaniswamy, S., Choi, J., Song, L., Mazumder, J., 2011. Additive Manufacturing by Direct Metal Deposition. Advanced Materials & Processes, vol. 169.

El-Galy, I.M., Saleh, B.I., Ahmed, M.H., 2019. Functionally graded materials classifications and development trends from industrial point of view. SN Appl. Sci., vol. 1. https://doi.org/10.1007/s42452-019-1413-4.

Erasenthiran, P., Ball, R., Jungreuthmayer, C., O'Neill, W., Steen, W.M, 1997. Laser step shaping for laminated object manufacturing parts, International Congress on Applications of Lasers & Electro-Optics, San Diego, California, USA, E84-E92. https://doi.org/10.2351/1.5059691.

Feenstra, D.R., Molotnikov, A., Birbilis, N., 2020. Effect of energy density on the interface evolution of stainless steel 316L deposited upon INC 625 via directed energy deposition. Journal of materials science, vol. 55, pp. 13314-13328.

Gäumann, M., Bezençon, C., Canalis, P., Kurz, W., 2001. Single-crystal laser deposition of superalloys: processing-microstructure maps. Acta Materialia, vol. 49(6), pp. 1051-1062.

Gebhardt, A., 2016. Additive Fertigungsverfahren. Carl Hanser Verlag GmbH & Co. KG. München.

Gharbi, M., Peyre, P., Gorny, C., Carin, M., Morville, S., Le Masson, P., Carron, D., Fabbro, R., 2013. Influence of various process conditions on surface finishes induced by the direct metal deposition laser technique on a Ti-6Al-4V alloy. Journal of Materials Processing Technology, vol. 213(5), pp. 791-800.

Gibson, I., Rosen, D.W., Stucker, B., 2010. Additive Manufacturing Technologies. Springer US. Boston, MA.

Graf, B., Gumenyuk, A., Rethmeier, M., 2012. Laser Metal Deposition as Repair Technology for Stainless Steel and Titanium Alloys. Physics Procedia, vol. 39, pp. 376-381.

Großmann, K., Wiemer, H., Hardtmann, A., Penter, L., Kriechenbauer, L. 2010. Static compensation for elastic tool and press deformations during deep drawing. Production Engineering, vol. 4, pp. 157-164.

Guminski, A., Hübner, T., Rouyrre, E., von Roon, S., Schimmel, M., Achtelik, C., Rhiemeier, J.M., Fahl, U., Bailey, I., 2019. Energiewende in der Industrie Potenziale, Kosten und Wechselwirkung mit dem Energiesektor. www.bmwk.de/

Hao, X., Dong, H., Li, S., Xu, X., Li, P., 2018. Lap joining of TC4 titanium alloy to 304 stainless steel with fillet weld by GTAW using copper-based filler wire. Journal of Materials Processing Technology, vol. 257, pp. 88-100.

Hart, F.V., 1942. Mold and mold making method. US Patent, US2274060A, priority date: 31.10.1938.

Hauk, V., 1997. Structural and Residual Stress Analysis by Nondestructive Methods. Elsevier. https://doi.org/10.1016/B978-0-444-82476-9.X5000-2.

Hiegemann, L., Agarwal, C., Weddeling, C., Tekkaya, A.E., 2016. Reducing the stair step effect of layer manufactured surfaces by ball burnishing, Nantes, France, vol. 1769(1), pp. 190002.

Himmer, T., Techel, A., Nowotny, S., Beyer, E., 2003. Recent developments in metal laminated tooling by multiple laser processing. Rapid Prototyping Journal, vol. 9(1), pp. 24-29.

Hölker, R., 2014. Additiv hergestellte Werkzeuge mit lokaler Innenkühlung zur Produktivitätssteigerung beim Aluminium-Strangpressen. Dr.-Ing. Dissertation. Technische Universität Dortmund. Dortmund.

Hölker, R., Tekkaya, A.E., 2018. Verfahren zur Reduzierung des Treppenstufeneffekts bei aus Blechlamellen geschichteten Werkzeugen/Bauteilen mittels additiver und umformtechnischer Nachbearbeitung. German patent DE102018004294 (A1), priority date: 17.05.2018.

Love, A.E.H., 1888. XVI. The small free vibrations and deformation of a thin elastic shell. Phil. Trans. R. Soc. Lond. A, vol. 179, pp. 491-546.

ISO 21920 (2021). Geometrical product specifications (GPS) - Surface texture: Profile - Part 1: Indication of surface texture, Beuth Verlag GmbH.

Jasim, K.M., Rawlings, R.D., West, D.R.F., 1993. Metal-ceramic functionally gradient material produced by laser processing. Journal of materials science, vol. 28, pp. 2820-2826.

Jiang, J., Lian, G., Xu, M., Li, C., Chen, B., Li, B., 2016. Influence of Preheating Temperature on Mechanical Properties of Laser Cladding Layer. Proceedings of the ASME 2016 International Manufacturing Science and Engineering Conference, Blacksburg, Virginia, USA. vol. 1. https://doi.org/10.1115/MSEC2016-8718.

Jiang, X., Scott, P., Whitehouse, D., Blunt, L., 2007. Paradigm shifts in surface metrology. Part I. Historical philosophy. Proc. R. Soc. A., vol. 463(2085), pp. 2049-2070.

Karbasian, H., Tekkaya, A.E., 2010. A review on hot stamping. Journal of Materials Processing Technology, vol. 210(15), pp. 2103-2118.

Karunakaran, K.P., Suryakumar, S., Pushpa, V., Akula, S., 2010. Low cost integration of additive and subtractive processes for hybrid layered manufacturing. Robotics and Computer-Integrated Manufacturing, vol. 26(5), pp. 490-499.

Kelbassa, J., Gasser, A., Bremer, J., Pütsch, O., Poprawe, R., Henrich Schleifenbaum, J., 2019. Equipment and process windows for laser metal deposition with coaxial wire feeding. Journal of Laser Applications, vol. 31(2), pp. 22320.

Kleiner, M., Krux, R., 2001. Entwicklung eines Verfahrens zur schnellen Herstellung von Tief- und Streckziehwerkzeugen aus Blechlamellen für die Prototypen- und Kleinserienfertigung (Rapid Tooling). Verl. und Vertriebsges. mbH. Düsseldorf.

Kolbe, J., 2012. Thermisch beschichtete, faserverstärkte Polymerwerkzeuge für die Umformung höherfester Blechwerkstoffe. Technische Universität Dortmund.

Komodromos, A., Kolpak, F., Tekkaya, A.E., 2022. Manufacturing of Integrated Cooling Channels by Directed Energy Deposition for Hot Stamping Tools with Ball Burnished Surfaces. Berg Huettenmaenn Monatsh, vol. 167, pp. 428-434.

Kong, C.Y., Carroll, P.A., Brown, P., Scudamore, R.J., 2007. www.twi-global.com

Kou, S., 2020. Welding metallurgy. John Wiley & Sons Inc. Hoboken NJ.

Krishnan, A., Fang, F., 2019. Review on mechanism and process of surface polishing using lasers. Front. Mech. Eng., vol. 14, pp. 299-319.

Kumaran, M., Senthilkumar, V., 2021. Experimental characterization of stainless steel 316L alloy fabricated with combined powder bed fusion and directed energy deposition. Weld World, vol. 65, pp. 1373-1388.

Küpper, D., Kuhlmann, K., Pieper, C., Burchardt, J., Schlageter, J., 2022. www.bcg.com.

Kwok, C.T., Cheng, F.T., Man, H.C., 2006. Cavitation erosion and corrosion behaviors of laser-aluminized mild steel. Surface and Coatings Technology, vol. 200(11), pp. 3544-3552.

Lange, K. (Ed.), 1990. Umformtechnik. Handbuch für Industrie und Wissenschaft Springer Verlag Berlin Heidelberg GmbH. Berlin, Heidelberg.

Lant, T., Robinson, D.L., Spafford, B., Storesund, J., 2001. Review of weld repair procedures for low alloy steels designed to minimise the risk of future cracking. International Journal of Pressure Vessels and Piping, vol. 78 (11-12), pp. 813-818.

Lauwers, B., Klocke, F., Klink, A., 2010. Advanced manufacturing through the im-plementation of hybrid and media assisted processes. Int. Chemnitz Manufacturing Colloquium, vol. 54, pp. 205-220.

Levinson, M., 1981. A new rectangular beam theory. Journal of Sound and Vibration, vol. 74(1), pp. 81-87.

Li, C., Liu, Z.Y., Fang, X.Y., Guo, Y.B., 2018. Residual Stress in Metal Additive Manufacturing. Procedia CIRP, vol. 71, pp. 348-353.

Liu, F.Q., Wei, L., Shi, S.Q, Wei, H.L., 2020. On the varieties of build features during multi-layer laser directed energy deposition. Additive Manufacturing, p. 101491.

Lorenz, K.A., Jones, J.B., Wimpenny, D.I., Jackson, M.R., 2015. A review of hybrid manufacturing, Solid Freeform Fabrication Symposium Conference Proceedings, pp. 96-108.

Lv, M., Gu, Z., Li, X., Xu, H., 2016. Optimal Design for Cooling System of Hot Stamping Dies. ISIJ International, vol. 56(12), pp. 2250-2258.

Macherauch, E., Kloos, K.H, 1989. Bewertung von Eigenspannungen bei quasistatischer und schwingender Werkstoffbeanspruchung - Teil III. Mat.-wiss. u. Werkstofftech., vol. 20(3), pp. 82-91.

Macherauch, E., Wohlfahrt, H., Wolfstieg, U., 1973. Zur zweckmäßigen Definition von Eigenspannungen. HTM Journal of Heat Treatment and Materials, vol. 28(3), pp. 201-211.

Mahamood, R.M.., Akinlabi, E.T., Akinlabi, S., 2015. Laser power and Scanning Speed Influence on the Mechanical Property of Laser Metal Deposited Titanium-Alloy. Lasers Manuf. Mater. Process, vol. 2, pp. 43-55.

Marciniak, Z., Duncan, J., Hu, S., 2002. Mechanics of Sheet Metal Forming. Elsevier.

Martina, F., Mehnen, J., Williams, S.W, Colegrove, P., Wang, F., 2012. Investigation of the benefits of plasma deposition for the additive layer manufacture of Ti-6Al-4V. Journal of Materials Processing Technology, vol. 212(6), pp. 1377-1386.

Meng, W., Zhang, W., Zhang, W., Yin, X., Cui, B., 2020. Fabrication of steel-Inconel functionally graded materials by laser melting deposition integrating with laser synchronous preheating. Optics & Laser Technology, vol. 131, p. 106451.

Merklein, M., Junker, D., Schaub, A., Neubauer, F., 2016. Hybrid Additive Manufacturing Technologies - An Analysis Regarding Potentials and Applications. Physics Procedia, vol. 83, pp. 549-559.

Milella, P.P., 2013. Fatigue and Corrosion in Metals. Springer Milan. Milano.

Mousavi, A., Sperk, T., Gietzelt, T., Kunze, T., Lasagni, A.F., Brosius, A., 2018. Effect of Contact Area on Friction Force in Sheet Metal Forming Operations. KEM, vol. 767, pp. 77-84.

Murphy, M.L, 1995. Rapid prototyping by laser surface cladding. Thesis (Ph.D.). University of Liverpool.

N. N., 2014. Material product data sheet austenitic stainless steel powder for laser cladding. Oerlikon metco.

Nakagawa, T., Kunieda, M., Liu, S.D., 1985. Laser Cut Sheet Laminated Forming Dies by Diffusion Bonding. In: Tobias, S.A. (Ed.), Proceedings of the Twenty-Fifth International Machine Tool Design and Research Conference. Macmillan Education UK, London, pp. 505-510.

Nakagawa, T., Suzuki, K., 1981. A Low Cost Blanking Tool with Bainite Steel Sheet Laminated. In: Alexander, J.M. (Ed.), Proceedings of the Twenty-First International Machine Tool Design and Research Conference. Macmillan Education UK, Lon-don, pp. 129-138.

Pepelnjak, T., Kuzman, K., 1998. Adaptable tooling sets for metal forming of geometrically similar products. Journal of Materials Processing Technology, vol. 80-81, pp. 413-420.

Pereira, M.P., Duncan, J.L., Yan, W., Rolfe, B.F., 2009. Contact pressure evolution at the die radius in sheet metal stamping. Journal of Materials Processing Technology, vol. 209(7), pp. 3532-3541.

Pereira, M.P, Yan, W.Y, Rolfe, B.F., 2007. Modeling of Contact Pressure in Sheet Metal Forming. MSF, vol. 561-565, pp. 1975-1978.

Pickin, C.G., Williams, S.W., Lunt, M., 2011. Characterisation of the cold metal transfer (CMT) process and its application for low dilution cladding. Journal of Materials Processing Technology, vol. 211(3), pp. 496-502.

Pinkerton, A.J., 2010. Laser direct metal deposition: theory and applications in manufacturing and maintenance, Advances in Laser Materials Processing. Elsevier, pp. 461-491.

Popov, V.V., Fleisher, A., 2020. Hybrid additive manufacturing of steels and alloys. Manufacturing Rev., vol. 7, pp. 6.

Popov, V.V., Grilli, M.L, Koptyug, A., Jaworska, L., Katz-Demyanetz, A., Klobčar, D., Balos, S., Postolnyi, B.O, Goel, S., 2021. Powder Bed Fusion Additive Manufacturing Using Critical Raw Materials: A Review. Materials (Basel, Switzerland), vol. 14(4), pp. 909-946.

Pragana, J., Sampaio, R., Bragança, I., Silva, C., Martins, P., 2021. Hybrid metal additive manufacturing: A state-of-the-art review. Advances in Industrial and Manufacturing Engineering, vol. 2, pp. 100032.

Rajurkar, K.P., Zhu, D., McGeough, J.A., Kozak, J., Silva, A. de, 1999. New Developments in Electro-Chemical Machining. CIRP Annals, vol. 48(2), pp. 567-579.

Ramos, J.A., Bourell, D.L., Beaman, J.J., 2002. Surface Over-Melt During Laser Polishing of Indirect-SLS Metal Parts. MRS Online Proceedings Library, vol. 758, pp. 19

Rangaswamy, P., Griffith, M.L., Prime, M.B, Holden, T.M., Rogge, R.B., Edwards, J.M., Sebring, R.J., 2005. Residual stresses in LENS® components using neutron diffraction and contour method. Materials Science and Engineering: A, vol. 399(1-2), pp. 72-83.

Ren, K., Chew, Y., Fuh, J., Zhang, Y.F, Bi, G.J, 2019. Thermo-mechanical analyses for optimized path planning in laser aided additive manufacturing processes. Materials & Design, vol. 162, pp. 80-93.

Rivette, M., Hacoët, J.Y., Mognol, P., 2007. A graph-based methodology for hybrid rapid design. Proceedings of the Institution of Mechanical Engineers, Part B: Journal of Engineering Manufacture, vol. 221(4), pp. 685-697.

Rosenthal, S., Hahn, M., Tekkaya, A.E., Platt, S., Kleszczynski, S., Witt, G., 2022. Speeding up Additive Manufacturing by Means of Forming for Sheet Components with Core Structures. International Journal of Precision Engineering and Manufacturing-Green Technology, vol. 9, pp. 1021-1034.

Röttger, A., Boes, J., Großwendt, F., Weber, S., 2023. Description of a new concept for the development of adapted hot-work tool steels for laser-powder bed fusion. Additive Manufacturing, vol. 61, pp. 103292.

Röttger, K., 2003. Walzen hartgedrehter Oberflächen, first ed. Shaker. Aachen.

Saboori, A., Aversa, A., Marchese, G., Biamino, S., Lombardi, M., Fino, P., 2019. Application of Directed Energy Deposition-Based Additive Manufacturing in Repair. Applied Sciences, vol. 9(16), pp. 3316.

Sato, F.E.K., Nakata, T., 2020. Energy Consumption Analysis for Vehicle Production through a Material Flow Approach. Energies, vol. 13(9), pp. 2396.

Schaub, A., Ahuja, B., Butzhammer, L., Osterziel, J., Schmidt, M., Merklein, M., 2016. Additive Manufacturing of Functional Elements on Sheet Metal. Physics Procedia, vol. 83, pp. 797-807.

Shamsaei, N., Yadollahi, A., Bian, L., Thompson, S.M., 2015. An overview of Direct Laser Deposition for additive manufacturing; Part II: Mechanical behavior, process parameter optimization and control. Additive Manufacturing, vol. 8, pp. 12-35.

Sharkeev, Y.P., Eroshenko, A.Y., Kovalevskaya, Z.G., Saprykin, A.A., Ibragimov, E.A., Glukhov, I.A., Chimich, M.A., Uvarkin, P.V., Babakova, E.V., 2016. Phase Composition and Microstructure of Ti-Nb Alloy Produced by Selective Laser Melting. IOP Conf. Ser.: Materials Science and Engineering, vol. 140, pp. 12020.

She, C.H., Hung, C.W., 2008. Development of multi-axis numerical control program for mill-turn machine. Proceedings of the Institution of Mechanical Engineers, Part B: Journal of Engineering Manufacture, vol. 222(6), pp. 741-745.

Spur, G., Zoch, H.W., 2015. Handbuch Wärmebehandeln und Beschichten. CARL HANSER Verlag GMBH. Munich.

Sreekanth, S., Ghassemali, E., Hurtig, K., Joshi, S., Andersson, J., 2020. Effect of Direct Energy Deposition Process Parameters on Single-Track Deposits of Alloy 718. Metals, vol. 10(1), pp. 96.

Syed, W.U.H., Pinkerton, A.J., Li, L., 2005. A comparative study of wire feeding and powder feeding in direct diode laser deposition for rapid prototyping. Applied Surface Science, vol. 247(1-4), pp. 268-276.

Syed, W.U.H., Pinkerton, A.J., Li, L., 2006. Combining wire and coaxial powder feeding in laser direct metal deposition for rapid prototyping. Applied Surface Science, vol. 252, pp. 4803-4808.

Tebaay, L.M., Hahn, M., Tekkaya, A.E., 2020. Distortion and Dilution Behavior for Laser Metal Deposition onto Thin Sheet Metals. Journal of Precision Engineering and Manufacturing-Green Technology, vol. 7, pp. 625-634.

Techel, A., 2005. Melato - Metal Laminated Tooling. Werkzeugfertigung durch Blechpaketierung; Ergebnisbericht zum Verbundvorhaben: Qualifikation innovativer Fertigungstechnologien zur flexiblen Fertigung von großformatigen und komplex geformten Werkzeugen mit seriennahen Eigenschaften; BMBF-Rahmenkonzept Forschung für die Produktion von morgen Fraunhofer IRB Verl. Stuttgart.

Temmler, A., Graichen, K., Donath, J., 2010. Laser Polishing in Medical Engineering. Laser material processing, vol. 7(2), pp. 53-57.

Timoshenko, S., Gere, J.M., 1985. Theory of elastic stability, second ed. Dover Publications. Mineola, N.Y.

Turnbull, D., 1981. Metastable structures in metallurgy. MTA, vol. 12, pp. 695-708.

VDI 3405, 2014. Additive Fertigungsverfahren - Grundlagen, Begriffe, Verfahrensbeschreibungen. Berlin. Beuth Verlag GmbH.

Verma, A., Yadav, H., Kumar, K., Singh, P.K., Sharma, M., Srivastava, V.S, Srivastava, A.K, 2022. State of Art on Microstructural and Mechanical Characterization of Wire and Arc Additive Manufacturing (WAAM). In: Rao, V.V., Kumaraswamy, A., Kalra, S., Saxena, A. (Eds.), Computational and Experimental Methods in Mechanical Engineering, vol. 239, pp. 93-104.

Walczyk, D.F., Dolar, N.Y., 1997. Bonding Methods for Laminated Tooling, International Solid Freeform Fabrication Symposium, pp. 211-222.

Walczyk, D.F., Hardt, D.E., 1998. Rapid Tooling for Sheet Metal Forming Using Profiled Edge Laminations—Design Principles and Demonstration. J Journal of Manufacturing Science and Engineering, vol. 120(4), pp. 746.

Walczyk, D.F., Hardt, D.F., 1994. A new rapid tooling method for sheet metal forming dies.

Wang, Z., Denlinger, E., Michaleris, P., Stoica, A.D, Ma, D., Beese, A.M, 2017. Residual stress mapping in Inconel 625 fabricated through additive manufacturing: Method for neutron diffraction measurements to validate thermomechanical model predictions. Materials & Design, vol. 113, pp. 169-177.

Weaver, W.R., 1991. Process for the manufacture of laminated tooling. US Patent, US5031483A, priority date: 06.10.1989.

Willenborg, E., 2011. Polishing with Laser Radiation, Poprawe R, ed Tailored Light 2. Springer Berlin Heidelberg, Berlin, 196-203.

Williams, S.W, Martina, F., Addison, A.C, Ding, J., Pardal, G., Colegrove, P., 2016. Wire + Arc Additive Manufacturing. Materials Science and Technology, vol. 32(7), pp. 641-647.

Wilson, J.M., Piya, C., Shin, Y.C., Zhao, F., Ramani, K., 2014. Remanufacturing of turbine blades by laser direct deposition with its energy and environmental impact analysis. Journal of Cleaner Production, vol. 80, pp. 170-178.

Wippermann, A., Gutowski, T.G., Denkena, B., Dittrich, M.-A., Wessarges, Y., 2020. Electrical energy and material efficiency analysis of machining, additive and hybrid manufacturing. Journal of Cleaner Production, vol. 251, pp. 119731.

Withers, P.J., Bhadeshia, H., 2001. Residual stress. Part 1 - Measurement techniques. Materials Science and Technology, vol. 17(4), pp. 355-365.

Witulski J., Trompeter M., Tekkaya A.E., Kleiner M., 2011. High wear resistant deep drawing tools made of coated polymers, CIRP Annals, vol. 60(1), pp. 311-314.

Wu, B., Pan, Z., Ding, D., Cuiuri, D., Li, H., Xu, J., Norrish, J., 2018. A review of the wire arc additive manufacturing of metals: properties, defects and quality improvement. Journal of Manufacturing Processes, vol. 35, pp. 127-139.

Xia, Z., Xu, J., Shi, J., Shi, T., Sun, C., Qiu, D., 2020. Microstructure evolution and mechanical properties of reduced activation steel manufactured through laser directed energy deposition. Additive Manufacturing, vol. 33, pp. 101114.

Xu, X., Ganguly, S., Ding, J., Guo, S., Williams, S., Martina, F., 2018. Microstructural evolution and mechanical properties of maraging steel produced by wire + arc additive manufacture process. Materials Characterization, vol. 143, pp. 152-162.

Ya, W., Pathiraj, B., Liu, S., 2016. 2D modelling of clad geometry and resulting thermal cycles during laser cladding. Journal of Materials Processing Technology, vol. 230, pp. 217-232.

Yang, Y.P., Dong, P., Tian, X., Zhang, Z., 1998. Prevention of Welding Hot Cracking of High Strength Aluminum Alloys by Mechanical Rolling. In: Vitek, J.M., David, S.A., Johnson, J.A., Smartt, H.B., Debroy, T. (Eds.), ASM Proceedings of the International Conference: Trends in Welding Research, Pine Mountain, GA, pp. 700-705.

Yin, Q., Soyarslan, C., Isik, K., Tekkaya, A.E., 2015. A grooved in-plane torsion test for the investigation of shear fracture in sheet materials. International Journal of Solids and Structures, vol. 66, pp. 121-132.

Yoo, S., Walczyk, D.F., 2005. Advanced Design and Development of Profiled Edge Laminae Tools. Journal of Manufacturing Processes, vol. 7, pp. 162-173.

Yoon, S.H., Na, S.J., 2005. Application of laser joining process for elimination of stair steps in steel laminate tooling. International Journal of Advanced Manufacturing Technology, vol. 25, pp. 154-159.

Yule, A.J., Dunkley, J.J., 1994. Atomization of melts for powder production and spray deposition. Clarendon Press. Oxford.

Zhao, G., Guo, Y.B., Zhu, P., Zhao, Y., 2018. Energy Consumption Characteristics and Influence on Surface Quality in Milling. Procedia CIRP, vol. 71, pp. 111-115.

Zhong, C., Gasser, A., Schopphoven, T., Poprawe, R., 2015. Experimental study of porosity reduction in high deposition-rate Laser Material Deposition. Optics & Laser Technology, vol. 75, pp. 87-92.

Zhu, Z., Dhokia, V.G., Nassehi, A., Newman, S.T., 2013. A review of hybrid manufacturing processes - state of the art and future perspectives. International Journal of Computer Integrated Manufacturing, vol. 26(7), pp. 596-615.

Attachment A

The list of tests carried out for single welded tracks with different sheet combinations.

Ferro55 powder

No.	Powder mass flow $\dot{m}$ (g/min)	Feed rate f (mm/min)	Laser power P (W)	Track-specific power density θ (W·mm/kg)	Sheet combination (mm-mm)	Fracture weld strength σ_W (MPa)
1	4	1400	1800	630	2.0-2.0	739.7
2	4	1400	1000	350	2.0-2.0	954.7
3	4	700	1800	315	1.0-2.0	555.8
4	4	700	1400	245	2.0-2.0	1070.1
5	4	1000	1800	450	0.5-1.0	161.9
6	4	1400	1400	490	1.0-1.0	534.7
7	4	700	1000	175	1.0-2.0	601.7
8	4	1000	1400	350	1.0-2.0	746.6
9	4	1000	1000	250	2.0-2.0	567.2
10	4	1000	1400	350	0.5-1.0	242.6
11	4	1400	1000	350	0.5-1.0	278.5
12	4	700	1800	315	0.5-2.0	172.4
13	4	1000	1400	350	0.5-0.5	203.0
14	4	700	1000	175	1.0-1.0	87.6
15	4	1000	1000	250	1.0-1.0	406.0
16	4	1400	1400	490	0.5-0.5	208.9
17	4	700	1000	175	0.5-0.5	191.5
18	4	700	1400	245	1.0-1.0	312.7
19	4	1000	1800	450	1.0-2.0	696.6
20	4	700	1000	175	0.5-2.0	340.1
21	4	700	1800	315	1.0-1.0	324.1

No.	Powder mass flow $\dot{m}$ (g/min)	Feed rate f (mm/min)	Laser power P (W)	Track-specific power density θ (W·mm/kg)	Sheet combination (mm-mm)	Fracture weld strength σ_W (MPa)
22	4	1400	1000	350	1.0-1.0	485.7
23	4	1000	1400	350	2.0-2.0	1115.6
24	7	1400	1800	360	0.5-1.0	191.5
25	7	1000	1800	257	2.0-2.0	1063.7
26	7	1400	1400	280	0.5-0.5	189.4
27	7	1000	1000	143	0.5-0.5	177.4
28	7	1400	1000	200	1.0-1.0	388.7
29	7	700	1800	180	0.5-1.0	134.9
30	7	700	1400	140	1.0-2.0	524.2
31	7	700	1000	100	2.0-2.0	552.0
32	7	1000	1400	200	2.0-2.0	1084.4
33	7	1400	1000	200	0.5-0.5	2113.6
34	7	1400	1400	280	0.5-2.0	366.1
35	7	700	1800	180	1.0-1.0	297.4
36	7	1000	1000	143	1.0-2.0	626.7
37	7	1000	1400	200	0.5-1.0	200.9
38	7	1000	1800	257	1.0-2.0	0.0
39	7	1400	1800	360	1.0-1.0	430.0
40	7	700	1000	100	0.5-0.5	0.0
41	7	700	1400	140	1.0-1.0	295.3
42	7	1000	1000	143	0.5-1.0	194.3
43	7	1400	1400	280	1.0-2.0	651.5
44	7	1000	1400	200	0.5-2.0	284.4
45	7	700	1400	140	0.5-0.5	271.8
46	10	1400	1800	252	2.0-2.0	857.7
47	10	1400	1400	196	2.0-2.0	657.3

No.	Powder mass flow $\dot{m}$ (g/min)	Feed rate f (mm/min)	Laser power P (W)	Track-specific power density θ (W·mm/kg)	Sheet combination (mm-mm)	Fracture weld strength σ_W (MPa)
48	10	1000	1800	180	2.0-2.0	847.4
49	10	700	1800	126	0.5-2.0	165.9
50	10	1400	1000	140	1.0-1.0	298.6
51	10	700	1000	70	2.0-2.0	396.6
52	10	1000	1400	140	1.0-2.0	416.2
53	10	700	1400	98	0.5-2.0	209.2
54	10	1000	1000	100	0.5-2.0	293.8
55	10	1000	1000	100	0.5-0.5	148.0
56	10	1400	1000	140	0.5-2.0	293.9
57	10	1400	1800	252	0.5-2.0	290.7
58	10	1400	1400	196	1.0-2.0	519.2
59	10	700	1400	98	0.5-1.0	156.9
60	10	1000	1400	140	0.5-2.0	249.5
61	10	1000	1000	100	0.5-1.0	194.3
62	10	1000	1800	180	0.5-2.0	234.0
63	10	700	1000	70	0.5-1.0	168.7
64	10	700	1000	70	0.5-0.5	168.6
65	10	1000	1400	140	0.5-0.5	168.2

316L-Si powder

No.	Powder mass flow $\dot{m}$ (g/min)	Feed rate f (mm/min)	Laser power P (W)	Track-specific power density θ (W·mm/kg)	Sheet combination (mm-mm)	Fracture weld strength σ_W (MPa)
1	4	1400	1400	490	1.0-1.0	176.6
2	4	1400	700	245	0.5-1.0	0.0
3	4	1000	1400	350	0.5-0.5	202.2

No.	Powder mass flow $\dot{m}$ (g/min)	Feed rate f (mm/min)	Laser power P (W)	Track-specific power density θ (W·mm/kg)	Sheet combination (mm-mm)	Fracture weld strength σ_W (MPa)
4	4	700	1000	175	2.0-2.0	1161.3
5	4	1400	1000	350	0.5-2.0	374.6
6	4	700	1400	245	1.0-2.0	662.2
7	4	700	700	122.5	0.5-0.5	193.3
8	4	1000	1000	250	0.5-0.5	187.4
9	4	1000	700	175	2.0-2.0	1068.3
10	4	1000	1000	250	0.5-1.0	253.7
11	4	700	1000	175	0.5-2.0	248.6
12	4	1000	700	175	1.0-1.0	0.0
13	4	1400	1000	350	0.5-1.0	268.1
14	4	1000	1400	350	0.5-2.0	335.5
15	4	700	1400	245	0.5-1.0	189.0
16	4	1400	1400	490	0.5-0.5	216.0
17	4	700	700	122.5	0.5-1.0	259.3
18	4	1000	1000	250	0.5-2.0	421.7
19	4	1400	1400	490	1.0-2.0	950.4
20	4	700	700	122.5	0.5-2.0	300.1
21	4	1400	1000	350	1.0-1.0	376.9
22	4	1400	700	245	0.5-0.5	0.0
23	4	700	1000	175	1.0-1.0	388.6
24	7	1400	1400	280	2.0-2.0	1137.0
25	7	700	1400	140	2.0-2.0	661.8
26	7	1400	1000	200	2.0-2.0	1040.8
27	7	1000	700	100	0.5-1.0	254.9
28	7	1000	1400	200	1.0-2.0	627.4
29	7	1400	700	140	0.5-2.0	330.2

No.	Powder mass flow $\dot{m}$ (g/min)	Feed rate f (mm/min)	Laser power P (W)	Track-specific power density θ (W·mm/kg)	Sheet combina-tion (mm-mm)	Fracture weld strength σ_W (MPa)
30	7	700	1000	100	0.5-0.5	152.9
31	7	700	700	70	2.0-2.0	753.2
32	7	1000	1000	142.8	2.0-2.0	700.2
33	7	1000	1400	200	0.5-0.5	169.4
34	7	1000	1000	142.8	0.5-0.5	182.4
35	7	1400	700	140	1.0-1.0	0.0
36	7	1400	1400	280	0.5-1.0	217.1
37	7	1000	700	100	1.0-2.0	626.8
38	7	1400	1000	200	0.5-2.0	321.4
39	7	700	1000	100	2.0-2.0	455.1
40	7	700	1400	140	1.0-2.0	524.2
41	7	700	700	70	0.5-2.0	261.3
42	7	1400	700	140	1.0-2.0	331.1
43	7	700	700	70	0.5-1.0	190.6
44	10	1400	1400	196	2.0-2.0	836.3
45	10	700	1400	98	2.0-2.0	383.3
46	10	1400	1000	140	2.0-2.0	769.8
47	10	1000	1400	140	1.0-2.0	507.1
48	10	1400	700	98	0.5-2.0	0.0
49	10	1000	1000	100	2.0-2.0	536.3
50	10	700	700	49	0.5-0.5	152.9
51	10	1000	700	70	1.0-1.0	0.0
52	10	700	1000	70	0.5-1.0	144.8
53	10	1400	700	98	1.0-2.0	409.4
54	10	1000	1400	140	1.0-1.0	245.6
55	10	1400	1000	140	1.0-2.0	758.5

No.	Powder mass flow $\dot{m}$ (g/min)	Feed rate f (mm/min)	Laser power P (W)	Track-specific power density θ (W·mm/kg)	Sheet combina-tion (mm-mm)	Fracture weld strength σ_W (MPa)
56	10	700	700	49	1.0-1.0	0.0
57	10	1400	1400	196	1.0-2.0	569.3
58	10	1000	700	70	0.5-2.0	140.0
59	10	1000	1000	100	0.5-1.0	209.4
60	10	700	1400	98	1.0-1.0	268.5
61	10	700	1000	70	0.5-0.5	193.7
62	10	1400	1000	140	0.5-0.5	0.0
63	10	1000	700	70	1.0-2.0	453.5
64	10	1000	1400	140	0.5-1.0	166.1
65	10	700	1000	70	1.0-1.0	174.6

Attachment B

Determination of coefficient for analytical model

```
clc;
close all;
clear;
format short;

a = sym('a','real'); %supported length
b = sym('b','real'); % free length
t = sym('t','real');

syms C1 C2 C3 C4 C5 C6 C7 C8
q1 = sym('q1','real');  % Linear vertical force in supported area
q2 = sym('q2','real');  % Linear vertical force in free length
FH = sym('FH','real');  % Horizontal force
l = sym('l','real');    % Total length of beam
kb = sym('kb','real') ; % Reaction  of support
ks = sym('ks','real') ; % Reaction  of support
L = sym('L','real');    % Coefficient L
x = sym('x','real');    % Position in x
E = sym('E','real');    % E-modul
Estarbeam = sym('Estarbeam','real'); % Equivalent E-module
I = sym('I','real');    % Inertial of moment
mu = sym('mu','real');  % Friction coefficient
tdisp = sym('tdisp','real');
ttotcush = sym('t','real');
Dbeam = sym('Dbeam','real');
Yi = sym('Yi','real');

% Coefficient based on BC
L = ((4*E*I)/((2*((ks*E*I)^0.5))-FH))^0.5;

vars = [C1 C2 C3 C4 C5 C6 C7 C8];

u1(x) = ((q1)/kb)+(((exp(x/L))*(C1*cos(x/L)+C2*sin(x/L)))+((exp(-
x/L))*(C3*cos(x/L)+C4*sin(x/L))));
Du1(x) = (((exp(x/L))/L)*(((C1+C2)*cos(x/L))+((C2-C1)*sin(x/L))))+(((exp(-
x/L))/L)*(((C4-C3)*cos(x/L))-((C3+C4)*sin(x/L))));
D2u1(x) = ((2*(exp(x/L))/(L^2))*((-C1*sin(x/L))+(C2*cos(x/L))))+((2*(exp(-
x/L))/(L^2))*((C3*sin(x/L))-(C4*cos(x/L))));
D3u1(x) = diff(D2u1,x,1);
u2(x) = (C5 + C6*exp((x*(-E*I*FH)^(1/2))/(E*I)) + C7*exp(-(x*(-
E*I*FH)^(1/2))/(E*I)) + (q2*x^2)/(2*FH) + (C8*E*I*x)/FH);
Du2(x) = diff(u2,x,1);
D2u2(x) = diff(u2,x,2);
```

```
D3u2(x) = diff(u2,x,3);

cond1 = u1(0) == (q1)/kb;
cond2 = D3u1(0) == 0;
cond3 = u1(a)*tdisp== u2(0);
cond4 = Du1(a)*tdisp== Du2(0);
cond5 = D2u1(a)*tdisp== D2u2(0);
cond6 = D3u1(a)*tdisp == D3u2(0);
cond7 = D2u2(b) == 0;
cond8 = D3u2(b) == 0;
eqns = [cond1, cond2, cond3, cond4, cond5, cond6, cond7, cond8];
coef = [C1 C2 C3 C4 C5 C6 C7 C8];

% result = (linsolve(A,B));
[A,B] = equationsToMatrix(eqns,coef);
result = simplify(linsolve(A,B));

% u1sub = subs(u1,coef,transFHose(result));

diary('result_coeff1.txt');
result(1)
diary off

diary('result_coeff2.txt');
result(2)
diary off

diary('result_coeff3.txt');
result(3)
diary off

diary('result_coeff4.txt');
result(4)
diary off

diary('result_coeff5.txt');
result(5)
diary off

diary('result_coeff6.txt');
result(6)
diary off

diary('result_coeff7.txt');
result(7)
diary off
```

```
diary('result_coeff8.txt');
result(8)
diary off
```

Aus der Dortmunder Umformtechnik sind im Shaker Verlag bisher erschienen:

A. Adelhof: Komponenten einer flexiblen Fertigung beim Profilrunden. ISBN 3-86111-601-4

G. Reil: Prozeßregelung numerisch gesteuerter Umformmaschinen mit Fuzzy Logic. ISBN 3-86111-862-9

F. Maevus: Rechnerintegrierte Blechteilefertigung am Beispiel des Gesenkbiegens. ISBN 3-8265-0104-7

R. Warstat: Optimierung der Produktqualität und Steigerung der Flexibilität beim CNC-Schwenkbiegen. ISBN 3-8265-1170-0

H. Sulaiman: Erweiterung der Einsetzbarkeit von Gesenkbiegepressen durch die Entwicklung von Sonderwerkzeugen. ISBN 3-8265-1443-2

Ch. Smatloch: Entwicklung eines numerisch einstellbaren Werkzeugsystems für das Tief- und Streckziehen. ISBN 3-8265-1465-3

T. Straßmann: Prozeßführung für das Walzrunden auf der Basis Neuronaler Netze. ISBN 3-8265-1966-3

L. Keßler: Simulation der Umformung organisch beschichteter Feinbleche und Verbundwerkstoffe mit der FEM. ISBN 3-8265-2256-7

E. Szücs: Einsatz der Prozeßsimulation bei der Entwicklung eines neuen Umformverfahrens - der Hochdruckblechumformung. ISBN 3-8265-3119-1

S. Chatti: Optimierung der Fertigungsgenauigkeit beim Profilbiegen. ISBN 3-8265-3534-0

F. Haase: Eigenspannungen an dünnwandigen Bauteilen und Schichtverbunden. ISBN 3-8265-4312-2

N. Austerhoff: Integrierte Produkt- und Prozeßgestaltung für die Herstellung von Blechbiegteilen. ISBN 3-8265-6613-0

D. Arendes: Direkte Fertigung gerundeter Aluminiumprofile beim Strangpressen. ISBN 3-8265-6442-1

R. Kolleck: Finite-Element-Simulation wirkmedienbasierter Blechumformverfahren als Teil einer virtuellen Fertigung. ISBN 3-8265-6566-5

T. Weidner: Untersuchungen zu Verfahren und Werkzeugsystemen der wirkmedienbasierten Blechumformung. ISBN 3-8265-6602-5

W. Homberg: Untersuchungen zur Hochdruckblechumformung und deren Verfahrenskomponenten. ISBN 3-8265-8684-0

M. Rohleder: Simulation rückfederungsbedingter Formabweichungen im Produktentstehungsprozess von Blechformteilen. ISBN 3-8265-9977-2

V. Hellinger: Untersuchungen zur Methodik der Berechnung und Herstellung von leichten Stützkernverbunden. ISBN 3-8322-0104-1

A. Klaus: Verbesserung der Fertigungsgenauigkeit und der Prozesssicherheit des Rundens beim Strangpressen. ISBN 3-8322-0208-0

B. Heller: Halbanalytische Prozess-Simulation des Freibiegens von Fein- und Grobblechen. ISBN 3-8322-0923-9

A. Wellendorf: Untersuchungen zum konventionellen und wirkmedienbasierten Umformen von komplexen Feinstblechbauteilen. ISBN 3-8322-2435-1

C. Klimmek: Statistisch unterstützte Methodenplanung für die Hochdruck-Blechumformung. ISBN 3-8322-2994-9

R. Krux: Herstellung eigenschaftsoptimierter Bauteile mit der Hochdruck-Blechumformung und Analyse der induzierten Eigenspannungen. ISBN 3-8322-3551-5

S. Jadhav: Basic Investigations of the Incremental Sheet Metal Forming Process on a CNC Milling Machine. ISBN 3-8322-3732-1

C. Beerwald: Grundlagen der Prozessauslegung und -gestaltung bei der elektromagnetischen Umformung. ISBN 3-8322-4421-2

A. Brosius: Verfahren zur Ermittlung dehnratenabhängiger Fließkurven mittels elektromagnetischer Rohrumformung und iterativer Finite-Element-Analysen. ISBN 3-8322-4835-8

R. Ewers: Prozessauslegung und Optimierung des CNC-gesteuerten Formdrückens. ISBN 3-8322-5177-4

T. Langhammer: Untersuchungen zu neuen Konzepten für PKW-Kraftstoff-behälter. ISBN 3-8322-5300-9

M. Schikorra: Modellierung und simulationsgestützte Analyse des Verbundstrangpressens. ISBN 3-8322-5506-0

M. Schomäcker: Verbundstrangpressen von Aluminiumprofilen mit endlosen metallischen Verstärkungselementen. ISBN 978-3-8322-6039-2

N. Ridane: FEM-gestützte Prozessregelung des Freibiegens. ISBN 978-3-8322-7253-1

R. Shankar: Surface Reconstruction and Tool Path Strategies for Incremental Sheet Metal Forming. ISBN 978-3-8322-7314-9

U. Dirksen: Testumgebung für Prozessregelungen zum Drei-Rollen-Profilbiegen mit virtuellem und realem Biegeprozess.
ISBN 978-3-8322-7673-7

D. Risch: Energietransfer und Analyse der Einflussparameter der formgebundenen elektromagnetischen Blechumformung.
ISBN 978-3-8322-8360-5

M. Marré: Grundlagen der Prozessgestaltung für das Fügen durch Weiten mit Innenhochdruck. ISBN 978-3-8322-8361-2

D. Becker: Strangpressen 3D-gekrümmter Leichtmetallprofile.
ISBN 978-3-8322-8488-6

V. Psyk: Prozesskette Krümmen - Elektromagnetisch Komprimieren - Innenhochdruckumformen für Rohre und profilförmige Bauteile.
ISBN 978-3-8322-9026-9

M. Trompeter: Hochdruckblechumformung großflächiger Blechformteile.
ISBN 978-3-8322-9080-1

H. Karbasian: Formgenauigkeit und mechanische Eigenschaften pressgehärteter Bauteile. ISBN 978-3-8322-9250-8

M. J. Gösling: Metamodell unterstützte Simulation und Kompensation von Rückfederungen in der Blechumformung. ISBN 978-3-8322-9355-0

H. Pham: Process Design for the Forming of Organically Coated Sheet Metal.
ISBN 978-3-8440-0309-3

B. Rauscher: Formschlüssig verbundene Metall-Kunststoff-Hybridbauteile durch Integration von Blechumformung und Spritzgießen.
ISBN 978-3-8440-0655-1

T. Cwiekala: Entwicklung einer Simulationsmethode zur zeiteffizienten Berechnung von Tiefziehprozessen.
ISBN 978-3-8440-0701-5

M. Hermes: Neue Verfahren zum rollenbasierten 3D-Biegen von Profilen.
ISBN 978-3-8440-0793-0

N. Ben Khalifa: Strangpressen schraubenförmiger Profile am Beispiel von Schraubenrotoren.
ISBN 978-3-8440-0969-9

J. Kolbe: Thermisch beschichtete, faserverstärkte Polymerwerkzeuge für die Umformung höherfester Blechwerkstoffe.
ISBN 978-3-8440-1353-5

L. Kwiatkowski: Engen dünnwandiger Rohre mittels dornlosen Drückens.
ISBN 978-3-8440-1381-8

T. Kloppenborg: Analyse- und Optimierungsmethoden für das Verbundstrangpressen.
ISBN 978-3-8440-1384-9

A. Schuster: Charakterisierung des Faserverlaufs in umgeformten Stählen und dessen Auswirkung auf mechanische Eigenschaften.
ISBN 978-3-8440-1581-2

A. Jäger: Strangpressen von Aluminiumprofilen mit prozessintegrierter umformtechnischer Weiterverarbeitung.
ISBN 978-3-8440-1654-3

M. M. Hussain: Polymer Injection Sheet Metal Forming – Experiments and Modeling.
ISBN 978-3-8440-2041-0

M. S. Aydın: Efficient Parameter Characterization for Hardening and Yield Locus Models for Sheet Metals.
ISBN 978-3-8440-2118-9

A. Canpolat: Experimentelle und numerische Bewertung der Fließortbestimmung mittels Kreuzzugversuch.
ISBN 978-3-8440-2126-4

V. Güley: Recycling of Aluminum Chips by Hot Extrusion.
ISBN 978-3-8440-2476-0

D. Pietzka: Erweiterung des Verbundstrangpressens zu höheren Verstärkungsanteilen und funktionalen Verbunden.
ISBN 978-3-8440-2538-5

M. Haase: Mechanical Properties Improvement in Chip Extrusion with Integrated Equal Channel Angular Pressing.
ISBN 978-3-8440-2571-2

Q. Yin: Verfestigungs- und Schädigungsverhalten von Blechwerkstoffen im ebenen Torsionsversuch.
ISBN 978-3-8440-2839-3

C. Becker: Inkrementelles Rohrumformen von hochfesten Werkstoffen.
ISBN 978-3-8440-2947-5

R. Hölker: Additiv hergestellte Werkzeuge mit lokaler Innenkühlung zur Produktivitätssteigerung beim Aluminium-Strangpressen.
ISBN 978-3-8440-3149-2

C. Weddeling: Electromagnetic Form-Fit Joining.
ISBN 978-3-8440-3405-9

A. Güner: In-situ stress analysis with X-ray diffraction for yield locus Determination.
ISBN 978-3-8440-3414-1

A. Güzel: Microstructure Evolution during Thermomechanical Multi-Step Processing of Extruded Aluminum Profiles.
ISBN 978-3-8440-3428-8

S. Hänisch: Verzugsanalyse kaltmassivumgeformter und wärmebehandelter Bauteile.
ISBN 978-3-8440-3761-6

A. Foydl: Strangpressen partiell verstärkter Aluminiumprofile.
ISBN 978-3-8440-3875-0

A. Weinrich Mora: Das Freibiegen mit inkrementeller Spannungsüberlagerung.
ISBN 978-3-8440-4221-4

S. Cai: Tailored and double-direction pressure distributions for vaporizing-foil Forming.
ISBN 978-3-8440-4255-9

G. Sebastiani: Erweiterung der Prozessgrenzen inkrementeller Blechumform-verfahren mittels flexibler Werkzeuge.
ISBN 978-3-8440-4359-4

C. Pleul: Das Labor als Lehr-Lern-Umgebung in der Umformtechnik. Entwicklungsstrategie und hochschuldidaktisches Modell.
ISBN 978-3-8440-4569-7

H. Hassan: Springback in deep drawing – Accurate prediction and reduction.
ISBN 978-3-8440-4924-4

L. Chen: An Investigation of Failure Mechanisms in Forming of Monolithic and Composite Sheets.
ISBN 978-3-8440-5168-1

L. Hiegemann: Glattwalzen beschichteter Oberflächen.
ISBN 978-3-84440-5419-4

G. Georgiadis: Hot stamping of thin-walled steel components.
ISBN 978-3-8440-5435-4

S. P. Afonichev: Numerische Simulation der Umformung von Sandwichblechen unter Berücksichtigung großer Krümmungen.
ISBN 978-3-8440-5471-2

D. May: Globally Competent Engineers. Internationalisierung der Ingenieurausbildung am Beispiel der Produktionstechnik.
ISBN 978-3-8440-5615-0

H. Chen: Granular medium-based tube press hardening.
ISBN 978-3-8440-5701-0

G. Grzancic: Verfahrensentwicklung und Grundlagenuntersuchungen zum Inkrementellen Profilumformen.
ISBN 978-3-8440-5889-5

S. Alkas Yonan: Inkrementelle Kaltumformung von Thermoplasten.
ISBN 978-3-8404-6026-3

P. Sieczkarek: Inkrementelle Blechmassivumformung.
ISBN 978-3-8440-6118-5

S. Ossenkemper: Verbundfließpressen in konventionellen Fließpresswerkzeugen.
ISBN 978-3-8440-6175-8

K. Isık: Modelling and characterization of damage and fracture in sheet-bulk metal forming.
ISBN 978-3-8440-6278-6

S. Gies: Thermische Spulenverluste bei der elektromagnetischen Blechumformung.
ISBN 978-3-8440-6468-1

C. H. Löbbe gen. Brüggemann: Temperaturunterstütztes Biegen und Wärmebehandeln in mehrstufigen Werkzeugen.
ISBN 978-3-8440-6485-8

J. Lueg-Althoff: Fügen von Rohren durch elektromagnetische Umformung – Magnetpulsschweißen.
ISBN 978-3-8440-6558-9

C. Dahnke: Verbundstrangpressen adaptiver Leichtbaukomponenten aus Aluminium und Formgedächtnislegierungen.
ISBN 978-3-8440-6630-2

O. K. Demir: New test and interpretation of electromagnetic forming limits of sheet metal.
ISBN 978-3-8440-6986-0

M. Schwane: Entwicklung und Eigenschaften von Längspressnähten beim Aluminiumstrangpressen.
ISBN 978-3-8440-6994-5

R. Meya: Schädigungskontrolliertes Blechbiegen mittels Druckspannungsüberlagerung.
ISBN 978-3-8440-7510-6

O. Hering: Schädigung in der Kaltmassivumformung: Entwicklung, Auswirkungen und Kontrolle.
ISBN 978-3-8440-7525-0

H. Traphöner: Erweiterung der Anwendungsgrenzen des ebenen Torsionsversuchs.
ISBN 978-3-8440-7737-7

O. Napierala: Tiefzieh-Verbundfließpressen: Analyse, Bauteileigenschaften und Potentiale.
ISBN 978-3-8440-7856-5

S. Wernicke: Inkrementelle Blechmassivumformung belastungsangepasster Funktionsbauteile.
ISBN 978-3-8440-7980-7

D. Staupendahl: 3D Profile Bending with Five Controlled Degrees of Freedom.
ISBN 978-3-8440-8006-3

S. Heibel: Schädigung und Versagensverhalten hochfester Mehrphasenstähle.
ISBN 978-3-8440-8269-2

F. Kolpak: Anisotropic Hardening in Cold Forging. Characterization, Simulation and Consequences.
ISBN 978-3-8440-8519-8

T. Mennecart: In-situ Hybridisierung von Faser-Metall Laminaten.
ISBN 978-3-8440-8566-2

S. Rosenthal: Umformung additiv gefertigter Bleche mit strukturiertem Kern.
ISBN 978-3-8440-8948-6

A. Schulze: Bleche aus stranggepressten Aluminiumspänen: Herstellung,Charakterisierung und Umformbarkeit.
ISBN 978-3-8440-8968-4

M. Hahn: Umformung mittels vaporisierender Aktuatoren: Experimente und Modellierung.
ISBN 978-3-8440-9106-9

M. Kamaliev: Isotherme Innenhochdruckumformung geschlossener Profile.
ISBN 978-3-8440-9168-7

F. Maaß: Gezielte Eigenspannungseinstellung in der inkrementellen Blechumformung.
ISBN 978-3-8440-9373-5

A. Schowtjak: Vorhersage der Porenentwicklung in der Umformtechnik.
ISBN 978-3-8440-9433-6